ABSTRACT

Title of Document: OPTIMIZATION OF DEDICATED BREAST
                            COMPUTED TOMOGRAPHY: BOWTIE
                            FILTER DESIGN AND OPTIMAL
                            SPECTRUM ANALYSIS

                            Kimberly Kontson, Doctor of Philosophy, 2014

Directed By: Dr. Robert Jennings
                            Department of Bioengineering

Recently, researchers have been investigating the use of a new imaging

modality called dedicated breast CT as a means of alleviating the problem of tissue

superposition that comes from acquiring a two-dimensional image of a three-

dimensional object in conventional mammography.

Several groups have investigated the optimal spectrum for this new imaging

modality using the dose efficiency as the FOM, but results are inconsistent. None of

these groups have employed the use of bowtie filtration in their optimal spectrum

studies. Given the right design, the inclusion of bowtie filtration will lead to

improved dose efficiency as well as consistency in the metric independent of position in a given phantom.

Bowtie filters can improve performance in several ways, including DR reduction, scatter reduction, patient dose reduction, and reduction of beam-hardening effects. In this dissertation, three different filter types with different choices for the tradeoffs between the performance improvements listed above are described. Examples of each type of bowtie filter are created for computational and Monte Carlo analyses, and two designs were fabricated for experimental analysis. Studies analyzing the material selection for each bowtie filter design and characterizing the scatter were also completed. Verification of the performance of the designs was done by calculating/measuring the HVL, intensity, and μ_{eff} behind the phantom as a function of fan-angle. The performance of the designs depended only weakly on incident spectrum and tissue composition. With various breast diameters, the calculated parameters varied the most, but the variation was substantially less than the no-bowtie filter case. For all designs, the DR requirement on the detector was reduced compared to the no-bowtie filter case. Simulation and experimental data showed that the use of our bowtie filters can reduce the peripheral dose to the breast by 61%, and provide uniform noise and CNR distributions.

The best performing bowtie filter design was implemented in simulation studies analyzing the optimal spectrum through calculation of the dose efficiency metric. The results from this study show the improvement and consistency that can be obtained with the inclusion of the proper bowtie filter, and provide the research

community with a methodology that will help lead to more consistent optimal

spectrum results.

OPTIMIZATION OF DEDICATED BREAST COMPUTED TOMOGRAPHY:
BOWTIE FILTER DESIGN AND OPTIMAL SPECTRUM ANALYSIS

By

Kimberly L. Kontson

Dissertation submitted to the Faculty of the Graduate School of the
University of Maryland, College Park, in partial fulfillment
of the requirements for the degree of
Doctor of Philosophy
2014

Advisory Committee:
Dr. Robert J. Jennings, Co-Chair
Professor Yu Chen, Co-Chair
Professor Yang Tao
Dr. Iacovos Kyprianou
Professor Julius Goldhar (Dean's Representative)

Dedication

To my family

for their never ending support, encouragement, and love

throughout my entire academic career.

Acknowledgements

I would like to acknowledge all of the people who have helped to bring this dissertation to fruition. Without their knowledge, teaching, and support, I could not have accomplished the many tasks necessary to achieve my academic and personal goals. In particular, I give thanks to. . .

. . . Dr. Robert Jennings, my advisor at the FDA. Nearly everything that I have learned about the field of diagnostic medical imaging has come through weekly conversations, abstract and paper revisions, and some hands-on experience in the lab with Dr. Jennings. He has not only given me the knowledge base needed to excel with this dissertation topic, but also instilled in me the good and decent practices of the professional world.

. . . Gene O'Bryan for his tireless efforts in assisting me with experimental set-ups. Each morning, Gene was the first person that I saw, allowing me to start each day with a pleasant conversation. His knowledge and creativity made the experimental work that I did possible, and I am so grateful to have been able to work with him before his retirement.

. . . Jackie Haynes for her office support and overall kind heart. Without her, this division would not be able to function as well as it does. I always enjoyed our conversations, and was glad to get to know Jackie.

them, this experience through graduate school would not have been the same. Whether the conversations were work-related or not, our row of carrels on the third floor provided the perfect environment for us to learn from each other, and to grow together as professionals and as friends. I hope that these friendships continue to grow even after we have moved on to the next chapter of our lives. A special thanks to my cubby buddy, Ivan, for always being there for me.

. . . my family, for whom this dissertation is dedicated. Without your guidance, support, encouragement, and love, I would not have been able to make it this far. Thank you to my parents, Kalle and Vicki, for their late night participation in dry-runs for conference presentations, their valuable revisions of countless documents, and their never-ending support and love. They are the epitome of goodness and professionalism, and I am proud to call them my parents. Thank you to my brother and sister, Stephen and Erica, for being supportive and also providing company during the much needed breaks from research. We are constantly challenging each other, encouraging each other, and laughing with each other, and I'm truly blessed to be a part of this wonderful family.

Table of Contents

List of Tables

List of Figures

List of Abbreviations

2D	two dimensional
3D	three dimensional
AUC	area under the curve
B_4C	boron carbide
BeO	beryllium oxide
CIRS	Computerized Imaging Reference System
CNR	contrast to noise ratio
DBCT	dedicated breast computed tomography
DE	dose efficiency
DR	dynamic range
FOM	figure of merit
FOV	field of view
HVL	half value layer
IPEM	Institute of Physics and Engineering in Medicine
LSF	line spread function
NPS	noise power spectrum
PENELOPE	PENetration and Energy LOss in Positrons and Electrons
PMMA	Poly-methyl methacrylate
PSF	point spread function
RMS	root mean square
ROI	region of interest
SDD	source to detector distance
SFD	source to filter distance
SNR	signal to noise ratio
SOCR	scatter to open field center ratio
SOD	source to object distance
SPR	scatter to primary ratio
UI	uniformity index
VOI	volume of interest

Chapter 1: Introduction

The American Cancer Society estimated that over 230,000 Americans would be diagnosed with invasive breast cancer in 2011. Approximately 40,000 women were expected to die from this disease last year, making breast cancer the second leading cause of cancer mortality among women. Since research has yet to hone in on a cure for breast cancer, the best way to reduce mortality is to improve methods for early detection and treatment.

The National Cancer Institute currently recognizes two methods for early detection of breast cancer: clinical examination by a physician and either digital or screen-film x-ray mammography. X-ray mammography is considered the gold standard screening method for women and has been a major contributor to the reduced mortality rate over the last few decades. [1, 2] It is very useful in the detection of microcalcifications, which are indicative of early formation of cancer, and has fairly high spatial resolution.[3] Furthermore, with the development of digital mammography, radiologists are able to adjust the contrast and size of a region of interest for better visualization of suspicious lesions. There is still a major limitation concerning superposition of structures in two dimensional images of the breast, especially for those women with greater breast density.[4]

A typical mammogram involves two x-ray projection views when the breast is fully compressed in the coronal and sagittal planes. Projecting a three-dimensional object onto a two-dimensional plane will make the detection of small lesions very difficult when

they are occult or overlapping in dense breast tissue.[3, 5, 6] Magnetic resonance imaging (MRI) of the breast is an alternate modality that has been investigated and shown to be able to identify the site of primary tumors in patients suspected of having occult primary cancer.[7] Although promising, MRI still cannot compete with mammography in terms of detection performance, imaging time and cost.[6, 7]

The major limitation resulting from superposition of tissue in mammography leads to a low positive predictive value. Data show that between 70% - 90% of biopsies that are performed based on suspicious mammograms turn out to be negative.[6] Dedicated breast computed tomography (CT) is an emerging technology that promises to alleviate the limitation of mammography caused by superposition.[5, 8, 9] The three-dimensional CT images overcome the masking of tissue detail that results from superposition in conventional mammography. These systems are designed such that the patient lies in the prone position on top of a table with a hole to place the breast (Figure 1.1). The breast hangs in the pendant position between a flat panel detector and x-ray source that are housed underneath the table. The entire imaging gantry rotates around the breast, generating projections from all angles that will be reconstructed into a three-dimensional volume.
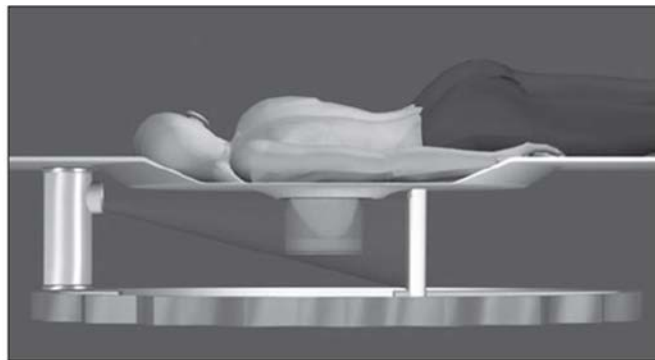
Figure 1.1: Schematic of clinical prototype dedicated breast CT scanner.[10] The x-ray source is shown on the left with the flat panel detector shown on the far right.

Studies have shown that dedicated breast CT has a higher contrast resolution than mammography, can better separate abnormalities from normal tissue, and has a high enough spatial resolution to visualize microcalcifications.[3, 10, 11] Another advantage of this system design is the fact that it requires little to no compression of the breast, a feature that appeals to many women.[10] Since dedicated breast CT requires a large number of projection images, there has been concern that the required dose to obtain reasonable image quality would be too high. However, Boone *et al.* demonstrated through simulations and cadaver experimentation that CT images of the breast could be acquired with equal or less dose compared to two-view mammography.[8]

Given that dedicated breast CT is a new imaging technology, optimization of the modality has not been fully investigated. There are several parameters that could be the focus of optimization studies. Since breast tissue is highly sensitive to radiation, there is a need for careful consideration of the dose delivered to the breast. High contrast and detectability are also desired traits of the system and demand attention when determining optimal parameters. With the cone-beam geometry used in dedicated breast CT systems, scatter contamination is a serious issue giving rise to degraded image quality. Optimization of scatter reduction techniques should be considered. Also, given the recent advancements in photon counting detectors and their application in the dedicated breast CT imaging scheme[12], optimization of the dynamic range seen by the detector may be of interest. The optimization of the balance between image quality, hardware limitations, and dose in dedicated breast CT is still a new field that has not yet converged on an accepted approach.

Over the last decade, research groups have focused on the issue of spectral optimization in dedicated breast CT[5, 9, 13-15] more than any other optimization issue. These optimizations focus on only one aspect of image quality and the dose delivered to the patient. Most of these studies used the dose efficiency (DE) metric, defined as the ratio of the square of the contrast-to-noise ratio (CNR) to the dose in the region-of-interest (ROI), as the figure of merit (FOM), with each group selecting different regions for analysis in the respective breast models/phantoms. Most studies used a uniform composition cylindrical breast phantom to perform the optimization analyses. Despite the similarities in the FOM and the methodology between different studies, the results are not consistent. Figure 1.2 summarizes the optimal tube voltage determined from the previously cited studies. As shown in the figure, the reported optimal tube voltage ranges from 40 kVp to 70 kVp with different uniform filters to achieve optimal image quality and dose. In addition to the inconsistent results, none of the studies looked at the DE metric as a function of position in the phantom. The x-ray fluence incident on the detector and the lesion contrast are two of the primary factors that can affect image quality in dedicated breast CT.[9] Given the change in path length through the cylindrical phantom from the center to periphery, one would expect the dose to the periphery of the breast phantom to be larger, and as a consequence of traveling through less tissue, the incident fluence upon the detector at the periphery of the phantom will be larger than at the center. These variable factors may generate different results as a function of radial location, even while using the same spectrum and FOM, which could help to explain the large variations in the determined optimal spectrum shown in Figure 1.2. Using a

technique to provide uniform image quality and dose would be advantageous and may

pave the way for improved, more consistent optimal spectrum results.
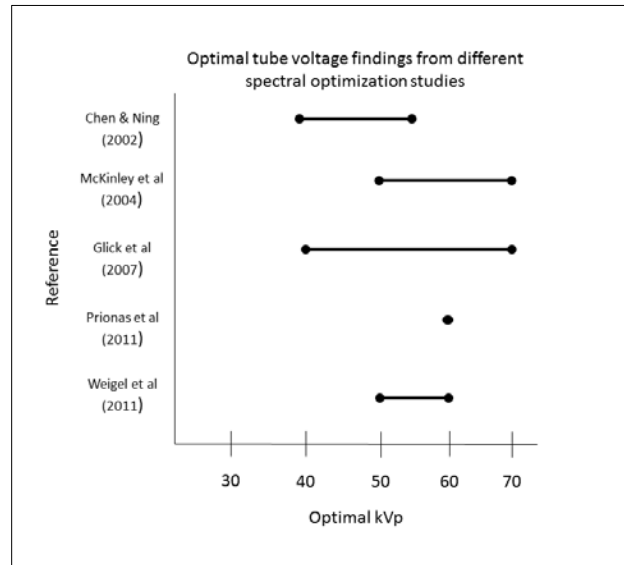
Figure 1.2: Comparison of optimal tube voltages determined by various groups

The bowtie filter is one additional component lacking in the previously discussed

studies that may be added to the imaging scheme in dedicated breast CT to produce the

desired uniform image quality and dose, as well as address some of the other

optimization parameters that were not covered in the previous studies. Figure 1.3 shows

the top view of a dedicated breast CT system with the inclusion of a bowtie filter between

the source and the object being imaged (breast). Bowtie filters have become common

place in the clinical environment for CT scanning of the abdomen, extremities, and other

parts of the body.[16] These filters can improve performance in several ways, including

dynamic range reduction, scatter reduction, and reduction of beam-hardening effects.[17-19]

One study on the influence of bowtie filtration on cone-beam CT image quality

determined that bowtie filters result in an overall improvement of CT number accuracy, skinline visualization, image uniformity, low-contrast detectability, and patient dose.[19] These results were obtained using the CatPhan 500 phantom meant to reflect the human torso with large variations in tissue compositions. In dedicated breast CT, it may be possible to provide more exact matching to the object since the object (i.e. breast) is composed of soft tissue with composition variations far smaller than in conventional CT where the object generally contains both soft tissue and bone. The pendant breast is also a fairly symmetric object, allowing for a reasonable geometric match between the object and the bowtie filter.
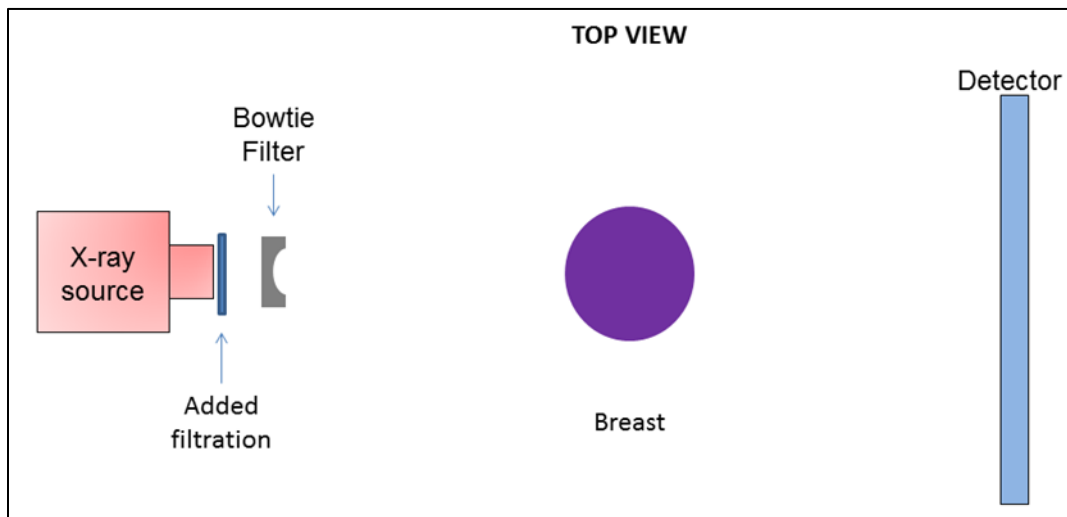
Figure 1.3: Top-side view of a dedicated breast CT system set-up with the inclusion of a bowtie filter between the x-ray source and the breast.

To facilitate the design of bowtie filters for dedicated breast CT, a standard breast can be assumed on which all of the bowtie filter designs are based. The standard breast would have certain characteristics such as diameter, composition, and distance from the source that will factor into the design of a bowtie filter. In a clinical scenario, it would be

nearly impossible to match all of these design input parameters. Therefore, evaluation of the efficacy of a bowtie filter with parameters that differ from that of the standard breast is of great importance.

In this dissertation, three different bowtie filter designs are presented that address several of the optimization parameters discussed above, and evaluated to test the robustness of the designs against variations in design input parameters. Chapters 2 - 4 are dedicated to introducing the design concepts and implementing the designs in computational, simulation, and experimental environments provided an initial set of design input parameters. In Chapter 2, the general computational theory describing each bowtie filter is discussed. For two of the bowtie filter designs (bowtie design #1 and bowtie design #2), relative thickness values that determine the appropriate thickness of a specific material needed to accurately simulate breast tissue were computed using an established algorithm described in chapter 2.[20, 21] A similar algorithm was also used to make liquid phantoms equivalent to breast tissue of varying glandularity. To validate these liquid phantoms, two liquid mixtures of water, isopropyl alcohol, and glycerin were made to be equivalent to 25% fibroglandular/75% adipose and 50% fibroglandular/50% adipose breast tissue. These liquid mixtures were analyzed using spectroscopy methods to determine the attenuation coefficient of the liquid mixtures and compare the results to breast phantom materials of known glandularity.

In Chapter 3, initial design input parameters were defined and used to create three simulated bowtie filters. The design input parameters included breast composition, breast diameter, source-to-filter distance (SFD), source-to-object distance (SOD), and tube voltage (the tube voltage was only used as a design input parameter for one type of

bowtie filter. The independence of energy is built in to the other two designs). The justification for selecting the initial design input parameters and the material selection for each bowtie filter was discussed. The designs were validated by computational methods to calculate various values of interest, such as half-value layer (HVL) behind the phantom, transmitted energy fluence, and effective attenuation coefficient, all as a function of fan-angle. The bowtie designs were then simulated in the penEasy_Imaging geometry environment to collect simulated images of a cylindrical phantom with and without each bowtie filter. The projection images were used in an FDK filtered backprojection reconstruction algorithm to create a reconstructed volume, and the reconstructed images were analyzed. All calculations and analyses were repeated with varying design input parameters to test the robustness of the designs. The computational and simulation results showed that each bowtie design achieved its design goal, and performed well against variations in design input parameters.

Chapter 4 describes the simulation methodology used to analyze the bowtie filter designs as a function of material. Several different materials were chosen that differ in their atomic number composition and density so that a comprehensive understanding of the behavior of a given bowtie filter design with various materials could be obtained. The importance and need to perform such an analysis for optimization of a given dedicated breast CT system is explained. This chapter provides a way to determine the optimal bowtie filter design by taking into account several of the optimization issues previously listed above, and comparing them between different bowtie filter designs and within a given bowtie filter design. The values of interest included bowtie filter design profile, dynamic range, noise uniformity, dose distribution, and scatter. Only the SPR

was investigated for each bowtie filter design as a function of material. A more in depth analysis of scatter magnitude and distribution was done in Chapter 5 on the three bowtie filters described in Chapters 3 and 4. The results from Chapter 4 also showcase the flexibility of some of the designs in tailoring a specific parameter (such as dynamic range) to a user-defined value.

In Chapter 5, experimental and simulation methods were used to determine the scatter magnitude and distribution changes that occur with implementation of the three bowtie filter designs analyzed in Chapters 3 and 6. The scatter-to-primary ratio (SPR) was calculated using the lead strip beam-block method to obtain values of SPR as a function of horizontal distance across the object FOV. The experimental and simulation data were compared. The scatter distribution was also investigated and compared between the no-bowtie and bowtie filter cases for each of the three bowtie filter designs. These same analyses were repeated in both experimental and simulation environments for different breast phantom diameters and tube voltages. The results indicated that the addition of the bowtie filters in dedicated breast CT geometry could be used to reduce the scatter magnitude, and also produce a more uniform scatter distribution. The benefits of achieving such reductions and uniformities in the scatter signal are also addressed.

In Chapter 6, two of the three bowtie filter designs used for the computational analysis in Chapter 3 were constructed from the same specified materials, and analyzed experimentally. Radiation field mapping of the field behind the phantom was performed to validate and evaluate the bowtie filter designs. The RadCal AccuGold radiation monitoring system was used to collect simultaneous measurements of HVL and intensity at several positions behind a phantom for a variety of phantom diameters, breast

compositions, and tube voltages. The bench-top cone-beam CT system used to acquire images is also described, as well as the phantoms and bowtie filters used during acquisition. Since the computational work was done assuming a scatter-free case, a scatter reduction technique using a tungsten plate with an array of small holes was applied to all projection images. A description of this technique is covered in Chapter 6. Projection images were reconstructed using the same FDK filtered backprojection reconstruction algorithm used for the simulated images from Chapter 3. The same analyses were performed on the experimental reconstructed images as were done on the simulated reconstruction images.

Based on conclusions from previous chapters, one of the bowtie designs was implemented in a spectral optimization analysis using similar FOM's as previously cited studies, namely the DE metric. In Chapter 7, a more complete review of the spectral optimization studies done in dedicated breast CT is given. Initially, computational analyses were done without the use of a bowtie filter in order to demonstrate the issue of tube loading limitations in constraining the optimal spectrum. The results from this computational work highlight the importance of manufacturing an x-ray tube with the ability to generate sufficient fluence at lower tube voltages. The influence of bowtie filtration on the uniformity of the DE metric as a function of position in the phantom and the magnitude of the DE metric was investigated for various tube voltages with an additional 0.1 mm copper filtration.

Chapter 8 discusses areas of future work and Chapter 9 provides the conclusion to the dissertation.

Chapter 2: Bowtie filters for dedicated breast CT: theory and design approach

2.1 Introduction

In cone-beam CT geometries, the goal of a bowtie filter is to account for the change in the path length through an object as a function of the fan-angle in the xy-plane. For simplification, most bowtie filters are not designed to account for the change in path length through an object in the cone-angle in the yz-plane. By accounting for the varying path length as a function of fan-angle, it seems as if the detector has imaged a uniform, constant thickness object which provides the benefits of reducing the beam hardening artifact, dose, and scatter, as well as improving image uniformity among other benefits.[17-19]

In on design approach, the bowtie filter would be composed of the same material as the object being imaged. In body CT scans, such as abdominal or thoracic CT scans, this is not possible due to the large variations in the tissue composition of the region being imaged. There are several different types of tissues in these regions, (i.e. bone, soft tissue, muscle, air), with bone exhibiting drastically different attenuation characteristics compared to other tissues of the body. These regions of the body are also asymmetric. Most simulation studies that model the human torso or human head assume the shape of the region to be an ellipsoid with different major and minor axes.[22] Phantom

manufacturing companies also make this same assumption. As the projection angle

changes, the shape of the object will change. This results in the bowtie filter to be valid

only at a few projection angles, and has prompted research into dynamic bowtie filters

that have the ability to change the bowtie filter profile as a function of view-angle.[23-26]

Compared to the problematic geometry of body and head CT scans for bowtie

filter implementation, the configuration of the dedicated breast CT systems provides an

ideal set-up for bowtie filters. Since the breast is the only body region being irradiated,

the tissue composition is much more uniform. The two major tissues comprising the

breast are fibroglandular and adipose,[27] and these tissues are more similar in x-ray

attenuation characteristics compared to the tissues encountered in a thoracic or head CT

scan (Figure 2.1). The shape of the breast in the pendant position is more symmetric, and

will not change drastically for different view-angles. These features of dedicated breast

CT make this imaging modality a prime candidate for bowtie filter implementation: the

comparatively uniform tissue composition and symmetric shape allow for the possibility

of more direct match to the object (i.e. breast) to be made.
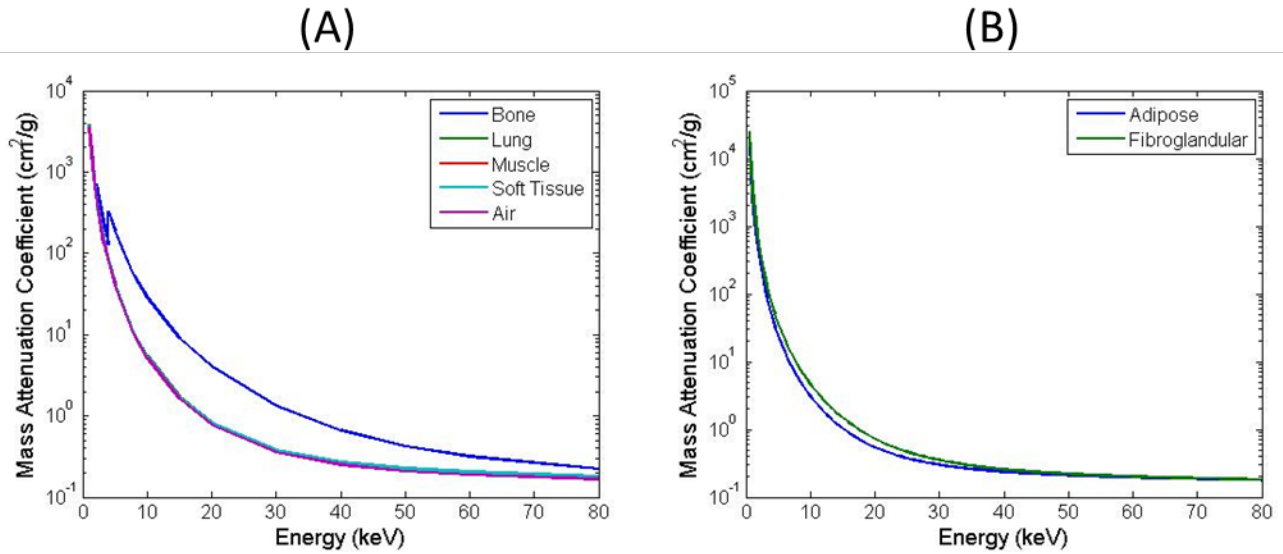
Figure 2.1: Mass attenuation coefficients from ICRU Report 44[28] for various tissues found in (A) body and head CT scans and (B) breast CT scans.

A few groups have designed bowtie filters for dedicated breast CT,[12, 29, 30] but these designs have not taken full advantage of the ability to produce a more accurate match of the object in a readily implementable way. One group conducted simulation studies using a 14-cm diameter cylindrical breast phantom with uniform breast composition. The bowtie filter used was a block composed of the same breast composition as the cylindrical phantom with a 14-cm diameter cylinder cut out of the center.[12] While this design would provide the exact match desired since it is made of breast tissue, this type of implementation would most likely be limited in its applicability to multiple breast diameters. Other groups have designed bowtie filters that transmit the same intensity as breast tissue for 50 keV photons,[29] generate a uniform dose distribution for a cylindrical phantom, and generate a uniform noise distribution.[30]

Two of the bowtie filter designs presented in this work use the ideas of spectral matching and basis material decomposition. It was established from earlier studies that

filter materials can be classified according to their qualitative and quantitative equivalence to a reference material.[31, 32] Two materials show quantitative equivalence when the same decrease in exposure is observed. However, in general, when quantitative equivalence is met between two different materials, the intensity distributions are not the same. Qualitative equivalence of two materials can be established if the two materials transmit the same relative spectral intensity such that the transmissions of the two materials are in the same ratio at all energies.[20] It is possible to determine the thickness of a single material that will achieve either of these characteristics. For the purposes of this work, however, the formulation to determine the thickness of a single material such that qualitative equivalence is achieved was used since this ensures a closer match between image contrast and patient dose. The design that achieves this qualitative equivalence to a given breast tissue composition using a single material will be referred to as bowtie design #1.

In order to achieve both quantitative and qualitative equivalence, two materials that each represent two independent functions are needed to simulate the spectral shape and intensity transmission of a reference material (i.e. breast).[33] Given two materials that both spectrally match the breast tissue, if one material transmits more than the breast tissue while the other transmits less, an appropriate combination of the two materials will produce the same spectral shape and same transmission as the breast tissue.[21] The design that achieves this qualitative and quantitative equivalence to breast tissue using two materials will be referred to as bowtie design #2.

By varying the thickness of either bowtie design #1 or bowtie design #2, an additional bowtie design that eliminates the need for beam-hardening corrections in the

calibration scan can be realized. The bowtie filter, referred to as bowtie design #3, attenuates the beam such that the same effective attenuation coefficient is observed for every fan-angle behind the phantom. This type of design may be clinically important for the improvement of tissue characterization in dedicated breast CT. Several studies have investigated the measurement of breast tissue linear attenuation coefficients, with most findings indicating a significant difference between fibroglandular tissue and cancerous tissues.[34-36] By eliminating beam hardening effects, accurate quantification of tissue components can be used to differentiate between normal and diseased lesions.[37] The details of such a design are further presented in this chapter, as well as the details behind the theory of bowtie designs #1 and #2.

2.2 Methods

2.2.1 Material simulation algorithm

Two of the three bowtie filter designs in this work were designed using an algorithm detailed by Jennings.[20, 21] This portion of the methods section will discuss the theoretical concepts used for the designs of bowtie #1 and bowtie #2. The first part of this section will discuss the methods used to generate the key design parameter for the single material bowtie filter design #1 that matches the transmitted spectral shape of breast tissue. The second part will discuss the methods used to generate the key design parameters for the two-material bowtie design #2 that transmits the same spectral shape and intensity as breast tissue. Both of these methods use a similar algorithm. The third part will discuss the spectroscopy methods used to validate the phantoms used in this work that were designed using similar algorithms as those described for the bowtie filters.

2.2.1.1 Determination of a_1 for bowtie design #1

The algorithm used to determine the thickness of a single material that will

produce the same spectral shape as a reference material (i.e. breast tissue) uses point-by-

point matching of the two spectra as the quality criterion. As stated by Jennings[20], there

have been several other groups that have conducted research in the same area using the

less strict definition of qualitative equivalence of matching the half-value layer (HVL)

between the two materials.[31, 38] The algorithm uses Eq. 2.1 as the mathematical basis for

the thickness determination.

$$\frac{T_1}{T_0} = e^{(\mu_0 t_0 - \mu_1 t_1)} = K \tag{2.1}$$

In this equation, T_0 and T_1 are the transmissions of the reference material and the

simulating material, respectively. Also, μ_0, t_0 and μ_1, t_1 are the energy dependent linear

attenuation coefficient and thickness of the reference material and simulating material,

respectively. Taking the natural logarithm and the energy derivative of each side of the

equation, and noting that the desired condition is that K is independent of energy, the

following relationship is established.

$$\mu_0' t_0 - \mu_1' t_1 = \left(\frac{1}{K}\right)\frac{dK}{dE} = 0$$

$$\frac{t_1}{t_0} = \frac{\mu_0'}{\mu_1'} \tag{2.2}$$

In fact, the match is not exact, K is not exactly independent of energy, and the ratio of thicknesses does depend on energy. The ratio is calculated for every energy on the grid specified by the user and the one giving the smallest RMS error is selected.

Putting things in to the perspective of the bowtie filter design, t_1 would represent the thickness of a single material chosen for the bowtie filter, and t_0 would represent the thickness of breast material. The variable a_1 was used to describe the thickness ratio of these two quantities. Using these concepts, the algorithm described by Jennings follows the flow chart shown in Figure 2.2.

Input
- Chemical Composition of bowtie material(S)
- Chemical composition of breast tissue
- Energy range of interest

Calculate thickness ratios for every energy in the range of interest

Determine average transmission ratio between reference and simulating material over all energies for each thickness ratio (K_{av})

Calculate RMS error between T_0 and scaled T_1 for a given thickness ratio

Smallest error

Relative thickness (a_1)

Figure 2.2: Flow chart detailing the steps in generating the relative thickness value used in the computational methods for designing the single material bowtie filter that transmits the same spectral shape as breast tissue.

The first step in the process of determining the relative thickness ratio for the single material design was to specify the chemical composition of the simulating material (bowtie filter material), the reference material (breast tissue), and the energy range of interest limited to the diagnostic range. The breast tissue chemical composition was determined according to the data from Hammerstein *et al.*[39] The linear attenuation coefficients and derivatives for the simulating material and reference material were then

created using the polynomial fit data from McMaster *et al.*[40] This older data set was used

because the representation of coefficients in the form of polynomials is convenient for

calculating derivatives. The goal of the algorithm was to determine the thickness ratio

that results in the smallest transmission error between the two materials. The thickness

ratio was first determined for all energies in the range of interest.   Then, the

transmissions of the simulating material and reference material (T_1 and T_0, respectively)

for a given thickness ratio were calculated at each energy (E) specified by the user and

averaged with weighting by T_0 (Eq. 2.3).[20]

$$K_{av} = \frac{\Sigma_E\left(\frac{T_1}{T_0}\right)T_0}{\Sigma_E T_0} = \left(\frac{T_1}{T_0}\right)_{av} \tag{2.3}$$

The RMS error between the transmission of the reference material and the scaled

transmission of the simulating material ($T_0 K_{av}$) was calculated for all energy points. The

thickness ratio value that corresponded to the K_{av} value that generated the smallest RMS

error was used as a_1 in subsequent calculations for the single material bowtie design #1.

2.2.1.2 Determination of a_1, a_2 for bowtie design #2

As stated in the previous section, it is possible to determine the thickness of a

single simulating material that is quantitatively <u>or</u> qualitatively equivalent to a reference

material. The equation needed to be satisfied to achieve qualitative equivalence was

defined by Eq. 2.2. The condition for matching the quantity of radiation requires the

transmissions to be equal such that[20]:

$$\frac{t_1}{t_0} = \frac{\mu_0}{\mu_1} \tag{2.4}$$

As stated by Alvarez and Macovski[33], only two independent functions are needed to describe the linear attenuation coefficient as a function of energy (within in the diagnostic range) of any material of biological interest. Alvarez and Macovski, in their work on energy-selective reconstruction in CT, apply the assumption that the two independent functions are those which describe the photoelectric effect and the Compton effect.[33] Similarly, a material's attenuation coefficient can also be described as a linear combination of two basis materials according to Eq. 2.5.[21, 41]

$$\mu_0(E)t_0 = \mu_1(E)t_1 + \mu_2(E)t_2 \tag{2.5}$$

The subscripts 1 and 2 refer to the basis materials. These materials should be different in their atomic number compositions, and also differ in the photoelectric and Compton attenuation effects. The algorithm by Jennings[21] determines the solution to Eq. 2.4 and Eq. 2.2 assuming two components for the simulating material. The solutions to those two equations are given as a_1 and a_2 (Eq. 2.6 and 2.7).

$$a_1 = \frac{t_1}{t_0} = \frac{\mu_0\mu'_2 - \mu_2\mu'_0}{\mu_1\mu'_2 - \mu_2\mu'_1} \tag{2.6}$$

$$a_2 = \frac{t_2}{t_0} = \frac{\mu_0\mu'_1 - \mu_1\mu'_0}{\mu_1\mu'_2 - \mu_2\mu'_1} \tag{2.7}$$

19

The process of determining these solutions is similar to that described in Figure 2.2. The chemical composition of the simulating materials, or the basis materials, as well as the reference material are input into the program in order to calculate the attenuation coefficients for each material. The energy range of interest is also specified. The values of a_1 and a_2 are calculated for each energy specified in the energy range. Using these values, the "effective" attenuation coefficient is calculated using a similar equation to Eq. 2.5 and compared to the attenuation coefficient of the reference material. The RMS error between these two attenuation coefficients is calculated for each energy (Figure 2.3). The values of a_1 and a_2 that yield the smallest RMS error are used in subsequent calculations for bowtie design #2.
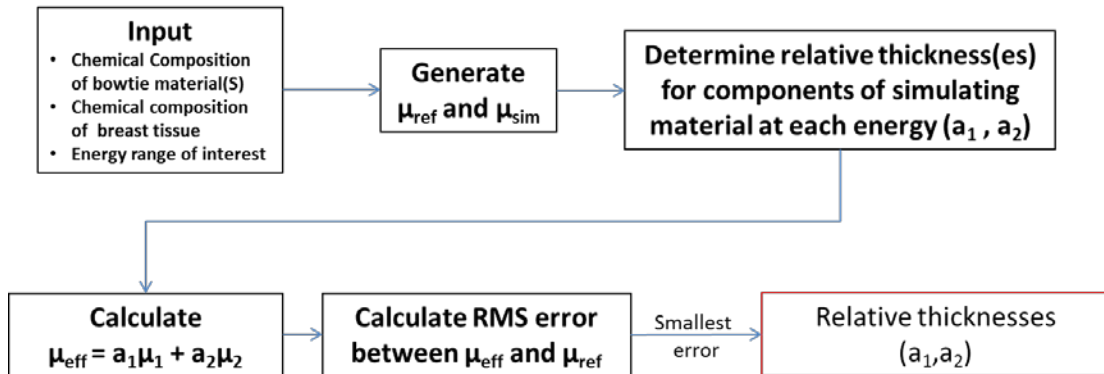
Figure 2.3: Flowchart detailing the steps in generating the thickness values (a_1,a_2) for bowtie design #2 that transmits the same spectral shape and intensity as breast tissue.

2.2.1.3 Validation of phantoms

In order to validate the liquid phantoms used in this work, two liquid mixtures of isopropyl alcohol, glycerin, and water were created that theoretically match the spectral shape and intensity of 50% fibroglandular/50% adipose breast tissue, and 25% fibroglandular/75% adipose breast tissue. A high purity germanium (Ge) detector

optimized for low energy spectroscopy was used to collect spectra for each liquid at 25

kVp and 35 kVp. The liquid nitrogen cooled Ge detector (CANBERRA Industries Inc.,

Meriden, CT) had a 0.025 mm Be entrance window and 2048 channels available to bin

the detected photons.

In order to calibrate the channels to the corresponding photon energy, a 90.87 μCi

Cobalt-57 radioactive source was used. Cobalt-57 decays by electron capture into

various excited states of the daughter nuclei. Several of these excited states emit γ-rays

with energies of 6.4 keV, 14.41 keV, 122.06 keV, and 136.47 keV.[42] The Cobalt-57

source was placed near the entrance window of the Ge detector, and the counts collected

in each channel were recorded for 500 seconds. An example of the spectrum that was

obtained from 500 seconds of data acquisition using the Cobalt-57 source is shown in

Figure 2.4.
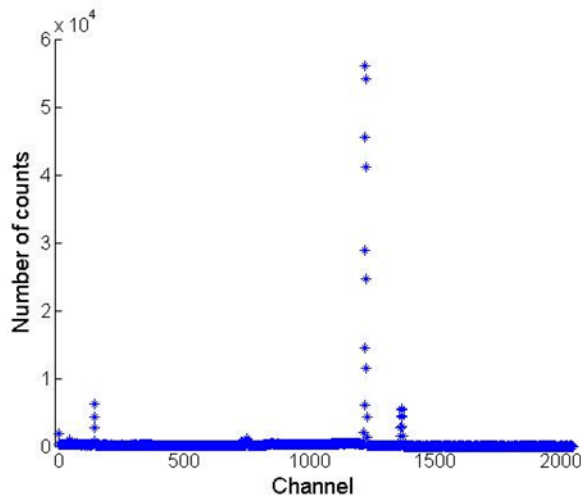
Figure 2.4: Calibration spectrum from Co-57 source used to determine the gain and offset
for calibration of channels to energy.

By identifying the peaks in the acquired spectrum and associating them with their known

energy, the gain and offset parameters were determined by using a linear fit of the data in

the form of Eq. 2.8.

$$Energy\,[keV] = Offset[keV] + Gain * Channel \tag{2.8}$$

Figure 2.5 shows an example of the calibration curve that is used to convert the channel

number into energy. The green points on the line represent each of the energy peaks

from the Cobalt-57 source.
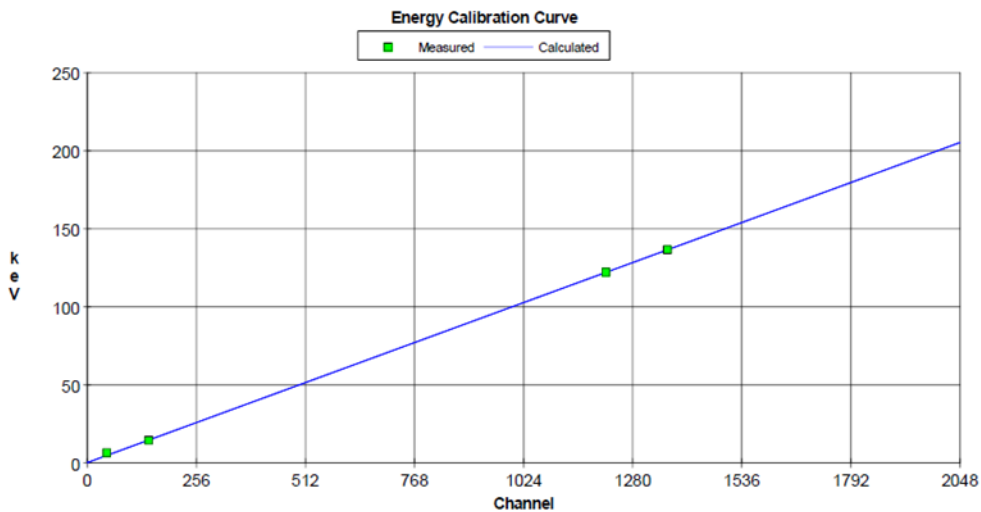
Figure 2.5: Calibration curve using the energy peaks from a Co-57 source. The known
energy of the γ-ray emission is given on the y-axis, and the corresponding channel of the
measured peak is shown on the x-axis. The calculated linear fit (blue line) allows for the
conversion between channel and energy.

After calibration, data were acquired for each liquid simulating the two different

breast compositions by putting the liquids in a small container made of PMMA and

placing that container in front of the Ge detector in line with the x-ray source. Spectra

22

were acquired for 500 seconds at 25 kVp and 35 kVp with and without the breast-simulating liquid in the container to obtain the transmitted spectrum and incident spectrum, respectively. Before any calculations could be done using the incident and transmitted spectra, spectral corrections were made to account for K-characteristic photons generated as a result of photoelectric absorption in the germanium detector material. If this photoelectric event occurs near the entrance surface of the detector, the K-characteristic photon may escape from the detector and cause the false registration of a lower energy photon in one of the channels. Figure 2.6 shows two 30 kVp spectra collected. The raw spectrum shows four smaller peaks near 6 keV and 10 keV that are the result of K-characteristic photon escape of the Ge Kβs and Kαs. To correct this, Monte Carlo simulations are computed to predict the probability of such events. With this information, a stripping procedure can be implemented to adjust the counts in each bin. The corrected spectrum shown in Figure 2.6 more accurately represents the counts recorded for a given energy.
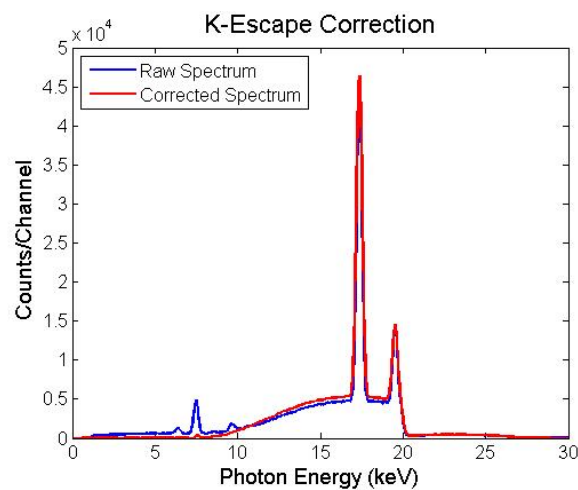
Figure 2.6: Raw spectrum and corrected spectrum for K-edge escape in the Ge detector.

With the knowledge of the distance x-rays traveled through the PMMA container, the linear attenuation coefficient was calculated by applying the Beer-Lambert equation. The same procedure was repeated for the CIRS epoxy material that simulates 25% fibroglandular/75% adipose breast tissue as a reference.[43] Another reference attenuation coefficient was calculated using the data from Hammerstein *et al.*[39] for each breast composition. All linear attenuation coefficients were plotted to compare the results.

2.2.2 Computational design of bowtie filters

For all three bowtie filter designs, the first step in the design process was to determine the parameters used to describe the breast being simulated. For the initial designs, the breast was assumed to be a cylinder. The parameters that needed to be specified included the diameter (d) of the breast phantom, the breast composition, the source-to-object distance (SOD), and the source-to-filter distance (SFD).

The path length as a function of fan-angle (p(θ)) from the source was determined by solving for the intersection between a circle described by Eq. 2.9 and a photon ray path described by Eq. 2.10. In these equations, x is the horizontal distance from the source, y is the vertical distance from the source, and θ spans from -5.4° to 5.4° in 0.04° increments.

$$y = \pm\sqrt{\left(\frac{d}{2}\right)^2 - x^2} + SOD \qquad (2.9)$$

$$y = \frac{x}{\tan\theta} \qquad (2.10)$$

Figure 2.7 shows a ray path at an arbitrary angle from the vertical dotted center line (0°) for a breast phantom 14 cm in diameter at 73.5 cm from the source. The red dots represent the intersections of Eq. 2.9 and Eq. 2.10. The distance between these two points for every angle is p(θ).
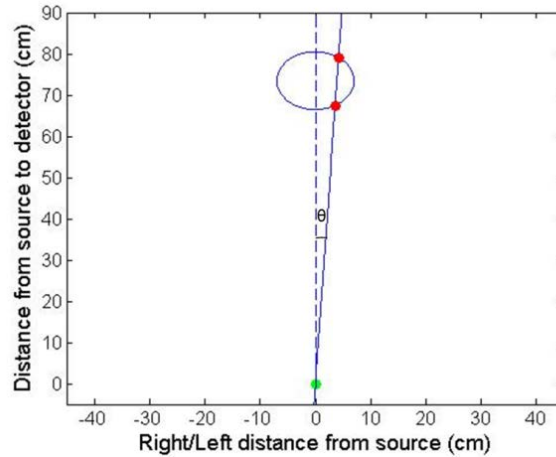
Figure 2.7: Path of photons from the x-ray source through the breast phantom at an angle, θ. The green dot represents the source and the red dots represent the intersection of the ray and the phantom.

For bowtie designs #1 and #2, the relative thickness values of $[a_1]$ or $[a_1,a_2]$, respectively, were used in the following equation to determine the bowtie filter thickness as a function of angle (t_{bti}).

$$t_{bti}(\theta) = \big(d - p(\theta)\big) * a_i \qquad (2.11)$$

Here, the subscript i denotes the simulating material: for the single material bowtie design #1, $i = 1$; for the two-material bowtie design #2, $i = 1, 2$.

2.2.2.1 Bowtie design #3

The third bowtie filter was designed by varying the thickness of the first and second bowtie designs such that the effective attenuation coefficient at the detector is the same across the object field-of-view (FOV). The initial spectrum, I_0, was a 50 kVp spectrum filtered with inherent filtration of 0.8 mm beryllium, 2.0 mm aluminum, and 0.1 mm copper. The incident intensity spectrum through the bowtie upon the breast and the transmitted spectrum through the bowtie and breast as a function of fan-angle were calculated by Eq.2.12 and 2.13, respectively.

$$I_{bt}(\theta) = I_0(\theta) * e^{-\mu_{bt}*t_{bt3}(\theta)} \tag{2.12}$$

$$I_{phan}(\theta) = I_{bt}(\theta) * e^{-\mu_{phan}*p(\theta)} \tag{2.13}$$

The effective attenuation coefficient observed through the center of the breast phantom was defined as

$$\mu_{eff,c} = \frac{ln\left(\frac{I_{bt}(0°)}{I_{phan}(0°)}\right)}{d}, \tag{2.14}$$

where $I_{bt}(0°)$ and $I_{phan}(0°)$ are defined as the intensity spectra through the center of the phantom. In order to observe the value of $\mu_{eff,c}$ at every position behind the phantom, the condition described by Eq.2.15 was applied and solved iteratively for the thickness of the bowtie filter as a function of fan-angle, $t_{bt3}(\theta)$ in Eq. 2.12.

$$\mu_{eff,c} = \frac{ln\left(\frac{I_{bt}(\theta)}{I_{phan}(\theta)}\right)}{p(\theta)}, \tag{2.15}$$

26

2.3 Results

The main purpose of this chapter was to elucidate the theory and design approach for the three different bowtie filters presented in this dissertation. Proceeding chapters will define the initial parameters used to design the different bowtie filters and the resulting profiles of each bowtie filter type. Therefore, the results of this chapter focus on the spectroscopic validation done on the liquid breast tissue samples that were made based on the material simulation analysis program. Only the data for the 25% fibroglandular/75% adipose breast tissue simulation are presented.

2.3.1 Material simulation algorithm output

When all the necessary data were entered into the algorithm (chemical compositions, energy range, etc.), relative amounts of the different simulating materials to be used for the simulation of the x-ray interaction properties of the user-specified reference material were computed. The output to the algorithm provides the user with a summary of the compositions of each simulating/reference material and the composition of the resulting mixture. Table 2.1 shows an example of the output using isopropyl alcohol, glycerol, and water to simulate 25% fibroglandular/75% adipose breast tissue. The right-most column represents the chemical composition of the resulting mixture that simulates breast tissue using the three constituent materials.

Table 2.1: Output from the material simulation algorithm. A summary of the chemical composition of the material being simulated (breast tissue) and the materials used to simulate the x-ray interaction properties of the breast tissue are shown. The atomic number (Z) and the weight fraction for each material are provided. The bottom row shows the density of the material.

25/75 Breast Tissue		Isopropyl Alcohol		Glycerol		Water		Liquid Mixture	
Z	Wt. Frac.	Z	Wt. Frac.	Z	Wt. Frac.	Z	Wt. Frac.	Z	Wt. Frac.
1	0.1095	1	0.1342	1	0.0876	1	0.1119	1	0.1126
6	0.5103	6	0.5996	6	0.3912	8	0.8881	6	0.4927
7	0.0208	8	0.2662	8	0.5212			8	0.3947
8	0.3575								
15	0.0020								
ρ = 0.955 g/ml		ρ = 0.786 g/ml		ρ = 1.260 g/ml		ρ = 0.998 g/ml		ρ = 0.952 g/ml	

The algorithm also outputs the relative volumes and masses of each simulating material needed to create the liquid mixture that simulates breast tissue. For the simulation of 25% fibroglandular/75% adipose breast tissue, the relative volumes for isopropyl alcohol, glycerol, and water were 0.6382, 0.3415, and 0.0203; the relative masses were 0.5268, 0.4519, 0.0213, respectively. These values were used to calculate the mass in grams of each material needed to create the liquid mixture.

Figure 2.8 shows the ratio of the calculated linear attenuation coefficient of the liquid mixture to the calculated linear attenuation coefficient of the 25% fibroglandular/75% adipose breast tissue. The same ratio was also plotted for the scatter coefficient defined as the summation of the Compton and coherent scattering coefficients. At lower energies, the linear attenuation coefficient and scatter coefficient of the liquid

mixture are slightly higher than the breast tissue material. The difference between the two quantities remains less than 0.5% at all energies.
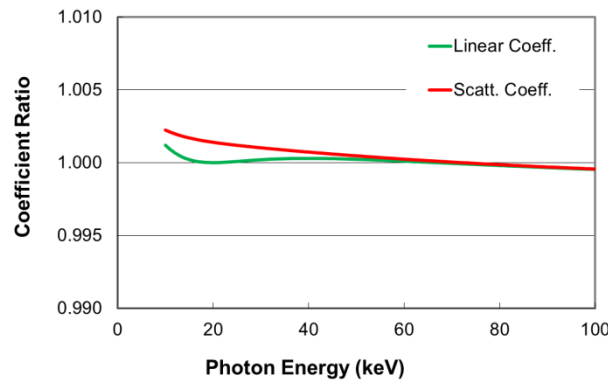
Figure 2.8: Ratio of the linear attenuation coefficient and scatter coefficient for the liquid mixture and the reference material, 25% fibroglandular/75% adipose breast tissue.

2.3.2 Calculation of linear attenuation coefficients

The linear attenuation coefficients of the breast tissue obtained from calculations and from measured spectra using the CIRS epoxy phantom and the liquid mixture for 35 kVp are shown in Figure 2.9. At lower energies, there is approximately an 11.5% increase in the spectrally measured linear attenuation coefficient for the liquid mixture compared to the calculated linear attenuation coefficient. However, the spectrally measured linear attenuation coefficient for the CIRS epoxy phantom also shows an increase at lower energies. Both spectrally measured linear attenuation coefficients from the CIRS epoxy phantom and the liquid mixture match very well over the given energy range, with less than a 1% change between the two values at all energies on average.

29
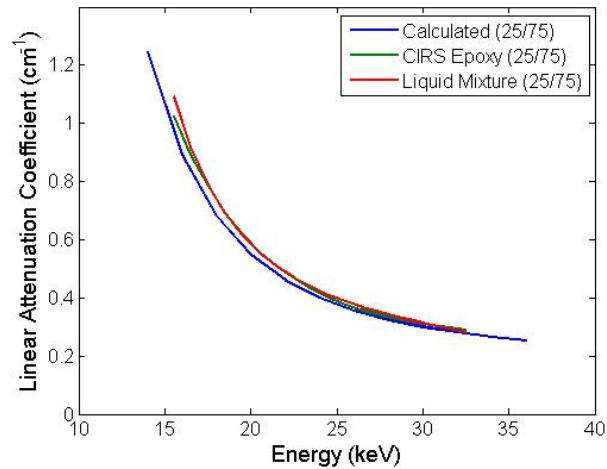
Figure 2.9: Calculated (blue) and spectrally measured and fit (green and red) linear attenuation coefficients for 25% fibroglandular/75% adipose breast tissue, CIRS epoxy phantom simulating 25% fibroglandular/75% adipose breast tissue, and a liquid mixture simulating 25% fibroglandular/75% adipose breast tissue. These data are from a 35 kVp spectrum.

The spectrally measured linear attenuation coefficients for the liquid mixture and the CIRS epoxy phantom were also calculated at 25 kVp. The results shown in Figure 2.10 indicate that the liquid mixture is able to simulate the 25% fibroglandular/75% adipose breast tissue independent of tube voltage. There is a slight deviation from the general trend of the linear attenuation coefficient at the lower energies of the 35 kVp data.
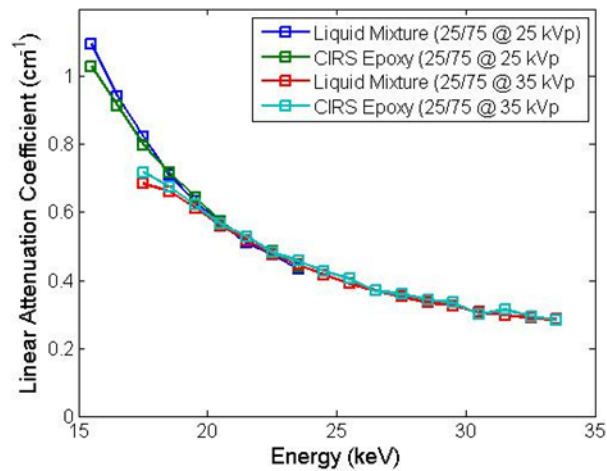
Figure 2.10: Spectrally measured linear attenuation coefficient at 25 kVp and 35 kVp for the CIRS epoxy phantom and liquid mixture simulating 25% fibroglandular/75% adipose breast tissue.

2.4 Discussion

The framework to design bowtie filters that more accurately represent the object being imaged in dedicated breast CT has been presented. Using the ideas of spectral matching and basis material decomposition, an algorithm was utilized to determine the relative thickness values needed to achieve either qualitative equivalence, or both qualitative and quantitative equivalence between a given breast tissue composition and simulating material(s). These relative thickness values were then used in the design of two bowtie filters. Another design that eliminates the need for software corrections in the calibration scan was presented. In the proceeding chapters, the theoretical basis of these designs were tested as input parameters were defined for each bowtie filter type, and used to design computational and physical prototypes to verify the desired design outcomes.

For bowtie design #1 and bowtie design #2, the material simulation algorithm developed by Jennings[20, 21] was used to compute the relative thickness values used to

compute the profiles of the bowtie filter designs (Eq. 2.11). To validate this algorithm,

spectroscopy studies were done to ensure the x-ray interaction properties could be

accurately simulated. Figure 2.9 shows good agreement between the linear attenuation

coefficient determined from acquired spectra for the liquid mixture and the CIRS epoxy

phantom, both simulating 25% fibroglandular/75% adipose breast tissue. However, at

lower energies, for the 35 kVp spectra, there is a small deviation from the expected

energy dependence. Past experience with this measurement technique has shown that

when higher energy spectra are used for the measurement, the additional scatter

generated by the sample shifts counts to lower energies, increasing the apparent

transmission of the sample at these energies, and leads to a lower calculated value for the

attenuation coefficient.

Chapter 3: Computational validation and evaluation of bowtie filter designs

3.1 Introduction

In breast CT, as in conventional CT, performance is enhanced by the use of compensating or bowtie filters. These filters can improve performance in several ways, including dynamic range reduction, scatter reduction, patient dose reduction, and reduction of beam-hardening effects.[17-19] In breast CT, it may be possible to provide more exact matching to the object since the object (i.e. breast) is composed of soft tissue with composition variations far smaller than in conventional CT where the object generally contains both soft tissue and bone. The pendant breast is also a fairly symmetric object, allowing for a reasonable geometric match between the object and the bowtie filter.

A few research groups have designed bowtie filters specific to dedicated breast CT.[29, 30, 44] One group studied the scatter reduction and dose reduction potential of a bowtie design that was designed to deliver ideal beam flattening for 50 keV photons in 50% fibroglandular breast tissue.[29, 44] The results indicated the scatter-to-primary ratio could be reduced, and dose could be reduced by 40% with the use of this bowtie filter. Another group recently proposed two designs for bowtie filters in dedicated breast CT that create either uniform dose distribution in the breast or uniform noise distribution from center to periphery of the resulting image.[30] Results also indicate that scatter and

dose are substantially reduced. In this work, we describe a design approach that can be used to obtain performance improvements in varying degrees, in a precise yet flexible manner. The approach requires reasonably close matching of the bow tie filter to both the shape and the composition of the object being imaged.

We describe three different filter types with three different choices for the tradeoffs between the performance improvements listed above. Two of the three types, when precisely matched to the shape and composition of the object being imaged (e.g., a breast) produce nearly uniform spectral shape exiting the breast. The first and simplest type (bowtie design #1) produces variable intensity that reduces the dynamic range requirements on the detector while transmitting the same spectral shape as breast tissue. This filter typically consists of a single material. A second type, referred to as bowtie design #2, produces constant x-ray intensity in addition to the same spectral shape transmitted through the breast. Its design requires two different materials. This type provides maximum patient dose reduction and scatter reduction. Both of these designs would result in reconstructed images of the object with "capping" artifacts (inverse of "cupping") due to the beam hardening in the flat field image of the bowtie filter. Software corrections can be applied to the flat field image to account for this beam hardening.[45, 46] A third bowtie type, a variation on the first type, can be designed such that the software correction is not needed. This bowtie design, referred to as bowtie design #3, requires one or more different materials and is designed to generate a constant effective attenuation coefficient across the field-of-view of the object. Further details about the design of each bowtie filter were previously described in Chapter 2.

In this chapter, we briefly review the theoretical basis for these designs, present computational approaches for a simple object, and give examples of the three designs based on that object. We also examine the sensitivity of the desired properties to mismatches between the object for which the filter was designed and the actual object being imaged. In a companion paper we will report on experimental tests of this approach to bowtie filter design.

3.2 Methods

3.2.1 Phantoms

The phantoms used in both the computational and simulation analyses were cylindrical, uniform composition phantoms. The diameter and composition of the phantoms were varied to evaluate the bowtie filter designs.

3.2.2 Bowtie filter design approach

Physical implementations of bowtie filters in breast CT generally assume a fan beam geometry with no variation in the z-direction, so that geometry is used in the mathematical development. Further details on the design approach for each bowtie filter can be found in Chapter 2 of this dissertation. The approach is briefly described here.

The first step in designing the bowtie filters was to determine the path length of the x-rays traveling through the phantom as a function of fan-angle, $p(\theta)$. This was done by finding the intersection between an equation of a circle describing the location and size of the breast phantom, and an equation describing the path of photons from the x-ray source (Eqs. 2.9 and 2.10).

3.2.2.1 Bowtie designs #1 and #2

Bowtie designs #1 and #2 are based on the ideas of single material spectral matching and basis material decomposition. Using algorithms described by Jennings[20, 21] that calculate 1), the quasi-optimal relative thickness value (a_1) of a specific material that matches the shape of the transmitted spectrum, and 2), the relative thicknesses of two materials (a_1,a_2) that produce a match to the spectral shape and intensity of the transmitted radiation, bowtie filters that closely match the desired properties over a broad range of diagnostic energies were designed. Please refer to Sections 2.2.1.1 and 2.2.1.2 for details. The equations for the relative thickness values are given by Eq. 3.1 for bowtie design #1, and Eqs. 3.2 and 3.3 for bowtie design #2..

$$Bowtie\ design\ \#1: a_1 = \frac{t_1}{t_0} = \frac{\mu'_0}{\mu'_1} \tag{3.1}$$

$$Bowtie\ design\ \#2: a_1 = \frac{t_1}{t_0} = \frac{\mu_0\mu'_2 - \mu_2\mu'_0}{\mu_1\mu'_2 - \mu_2\mu'_1} \tag{3.2}$$

$$a_2 = \frac{t_2}{t_0} = \frac{\mu_0\mu'_1 - \mu_1\mu'_0}{\mu_1\mu'_2 - \mu_2\mu'_1} \tag{3.3}$$

The variable *t* represents thickness, *μ* represents the attenuation coefficient and *μ'* represents the energy derivative of the attenuation coefficient. The subscript 0 denotes the reference material being simulated (i.e. breast) while the subscripts 1 and 2 denote the materials being used to simulate the breast. These relative thickness values were used to design the shape of the bowtie filter according to the following equations:

$$t_{bt1}(\theta) = (d - p(\theta)) * a_1 + t_{base1} * \left(\frac{1}{\cos\theta} - 1\right) \tag{3.4}$$

$$t_{bt2}(\theta) = (d - p(\theta)) * a_2 + t_{base2} * \left(\frac{1}{\cos\theta} - 1\right) \tag{3.5}$$

In these equations, t_{bt1} and t_{bt2} are the calculated thicknesses of material 1 and material 2

as a function of fan-angle, respectively. In the center of the bowtie filter, the thickness is

zero since the photons are already traveling through the entire diameter of the breast

phantom. However, to provide stability to the filters, a constant thickness of the same

material was added as a base. The last terms in Eqs. 3.4 and 3.5 take into account this

added thickness of t_{base1} and t_{base2} for the outer filter material and inner filter material,

respectively, for bowtie designs #1 and #2. For the single-material bowtie filter design

#1, only Eq. 3.4 was used.

3.2.2.2 Bowtie design #3

The third bowtie filter was designed by varying the thickness of the first and

second bowtie designs such that the effective attenuation coefficient at the detector is the

same across the object field-of-view (FOV). Details on this design can be found in

Section 2.2.2.1.

3.2.3 Material selection for bowtie designs

The initial bowtie designs were validated through computational modeling and

simulations, which allowed for greater flexibility in selecting material(s) for each bowtie

design. The choice of material controls the distribution of energy fluence across the

object FOV, and also affects the dose distribution. The dimensions of the bowtie filter

also need to be taken into consideration when translating these computational models into

physical models: a material with a high density will produce a very small thickness

variation that is difficult to machine, and a material with a low density will create a

bowtie design that is inconveniently large. With these constraints in mind, several

different materials were chosen for the initial bowtie designs including aluminum, poly-

methyl methacrylate (PMMA), beryllium oxide (BeO) and boron carbide (B_4C). The

chemical compositions and densities of each material are listed in Table 3.1.

Table 3.1: Chemical compositions and density of materials used in bowtie
filter designs

Material	Chemical Composition	Density (g/ml)
Aluminum	Al	2.7
PMMA	$C_5O_2H_8$	1.18
Beryllium oxide	BeO	2.5
Boron carbide	B_4C	2.52

All bowtie filters were designed with a width of 8 cm. Due to its high thermal

conductivity and electrical insulation abilities, BeO is commonly used in high

performance semi-conductor parts. B_4C is frequently used in tank armor and bullet proof

vests. However, these materials were chosen because their low atomic number

compositions and higher densities yield a reasonably sized bowtie design.

3.2.4 Design input parameters

One material selection is done, four design input parameters determine the

bowtie filter design according to our model: breast diameter, breast composition, SFD,

and SOD. The clinical work by Boone *et al.* showed that the average breast diameter

from a cohort of 200 women was 14 cm, so this was the breast diameter chosen for the

bowtie filter designs.[44] Research has shown the average fibroglandular percentage of the

female breast to be as low as 20%[47], while other studies have cited 50% as the average.[5, 13, 48] The breast composition of 40% fibroglandular/60% adipose that was used to design the bowtie filters described in this chapter falls in between these two values. When considering the SFD, there were two important factors: the physical limitations of the bench-top system and the scatter contribution from the bowtie filter. The minimum SFD that could be achieved with our system is approximately 10 cm. To reduce the amount of scattered radiation that reaches the phantom due to the bowtie filter, the SFD should be as small as possible. Also, since the same bowtie filter was used for different breast diameters, there needed to be enough space to translate the bowtie filters along the source-to-detector axis. Based on these considerations, a SFD of 16.25 cm was chosen in the computational modeling of the bowtie filters. The SOD was chosen to be 73.5 cm to mimic existing dedicated breast CT systems and geometries employed in other studies.[10, 14] A summary of the initial design input parameters is shown in Table 3.2.

Table 3.2: Initial design parameters for three bowtie filter designs

Design parameter	Value
Breast diameter	14 cm
Breast composition	40/60
SFD	16.25 cm
SOD	73.5 cm

3.2.5 Bowtie filter designs

Taking into account the bowtie filter material and the initial design input parameters, a bowtie filter of each type was computationally realized. Figure 3.1 shows the cross-section of each design using aluminum for bowtie design #1, BeO/B$_4$C for

bowtie design #2, and PMMA for bowtie design #3, respectively. In these plots, the cone-beam x-ray source would be located at the point (0,-16.25).
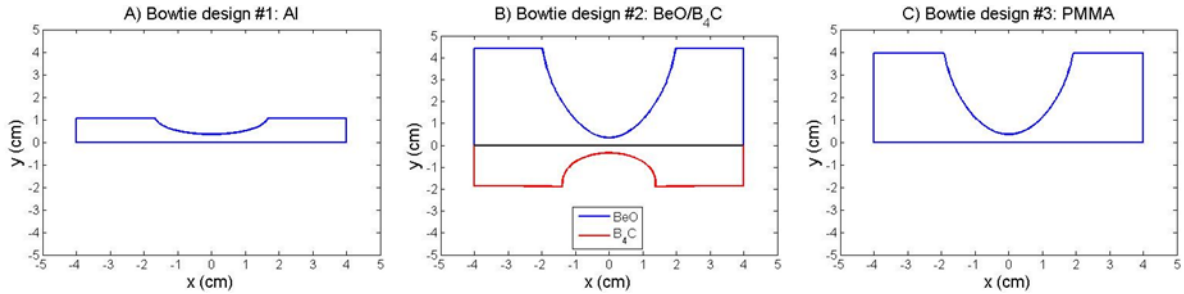
Figure 3.1: Cross-section views of the bowtie filter designs using (A) aluminum for bowtie design #1, (B) BeO/B$_4$C for bowtie design #2, and (C) PMMA for bowtie design #3.

3.2.6 Computational and simulation analyses

To validate and evaluate the bowtie filter designs, two separate methods were employed. A deterministic computational method was used to verify the x-ray behavior, and test it against variations in design input parameters. Calculated values of HVL, intensity, and effective attenuation coefficient as a function of fan-angle for various diameters and breast compositions were obtained with and without each bowtie filter. A stochastic Monte Carlo simulation method was used to further validate and evaluate the designs. Using simulated projection images, reconstructed volumes were obtained and used in the calculation of parameters such as noise uniformity, CNR homogeneity, line profiles, and dose distributions.

3.3 Results

3.3.1 Computational analyses

With the angular information about the thickness variation of the bowtie filter material(s), the designs can be deterministically validated and analyzed for robustness against variation in design input parameters. Using IPEM Report 78 spectra as input, the incident fluence upon the breast and the transmitted fluence through the breast can be obtained and used to generate values of HVL, energy fluence, and effective attenuation coefficient as a function of fan-angle, θ. The elemental attenuation data from XCOM[49] were used to calculate linear attenuation coefficients of the breast and bowtie filter materials according to the sum rule. Breast tissue composition was calculated using data from Hammerstein *et al.*[39] The energy fluence, E_{flu}, through the breast was calculated according to the following equation:

$$E_{flu}(\theta) = \int_0^{Emax} I_0 * e^{-\left(\mu_{bt}*t_{bt}(\theta)+\mu_{phan}*p(\theta)\right)} * \varepsilon(E) * \delta(E) \, dE \qquad (3.6)$$

The energy fluence was used as a reasonable approximation to the detector response. In this model, the detector efficiency $\varepsilon(E) = 1$, and the detector response $\delta(E) = E$ to mimic the behavior of energy integrating detectors. The effective attenuation coefficient as a function of fan-angle was calculated as

$$\mu_{eff}(\theta) = \frac{ln\left(\frac{I_{bt}(\theta)}{I_{phan}(\theta)}\right)}{p(\theta)}. \qquad (3.7)$$

The HVL, energy fluence, and effective attenuation coefficient were calculated

using the initial design input parameters (Table 3.2) to validate the bowtie filter designs.

Corresponding values were also calculated without the bowtie filter. To test the

robustness of the designs, various tube voltages, breast compositions and breast diameters

were investigated to determine the effect on the design outcome for each bowtie filter. It

was assumed that, for practical reasons, only a single bowtie filter would be used in a

clinical machine. Using the bowtie filters that were designed for a 14 cm, 40/60 breast at

50 kVp, breast diameters of 10 cm, 14 cm,and 18 cm, breast compositions of 25/75,

40/60, and 75/25, and different tube voltages between 40-60 kVp in 10 kVp increments

were used in the computation of HVL, energy fluence, and effective attenuation

coefficient. Since the same bowtie designs were used in the evaluation of the design

outcome with various parameters, the SFD was adjusted such that the edges of the bowtie

filter matched with the x-ray path that was tangent to the periphery of the breast phantom

when performing calculations for the 10 cm and 18 cm breast phantoms. All calculations

were performed assuming a scatter-free case.

3.3.1.2 Computational validation

Figure 3.2 shows the calculated HVL and normalized energy fluence as a function

of fan-angle with and without an aluminum bowtie of design #1 for a 14-cm diameter

phantom with 40% fibroglandular/60% adipose composition at 50 kVp. The 0° angle is

the x-ray beam that travels through the center of the phantom. With the inclusion of the

bowtie filter, the HVL is kept constant at all angles behind the phantom. As expected,

the energy fluence as a function of angle is not constant, but the variation from the central

ray is substantially decreased with the inclusion of the bowtie filter.
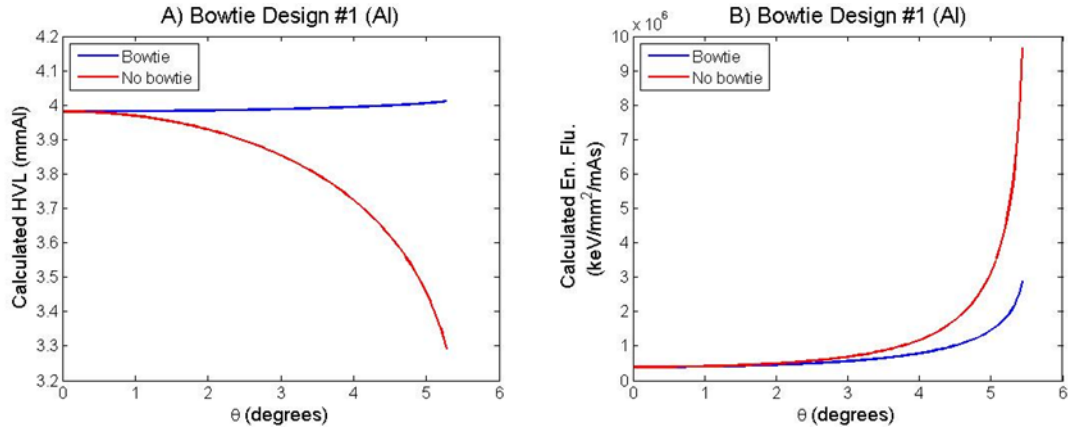
Figure 3.2: Calculated HVL (A) and energy fluence (B) as a function of fan angle with and without bowtie filter design #1.

Figure 3.3 shows similar plots for the BeO/B$_4$C bowtie design #2 for a 14-cm

diameter phantom with 40% fibroglandular/60% adipose composition at 50 kVp. This

design is meant to transmit the same spectrum and intensity as the breast tissue it

replaces. The calculated HVL is kept nearly constant across the phantom FOV compared

to the no-bowtie filter case, and the energy fluence calculated at the detector is

independent of the position behind the phantom.
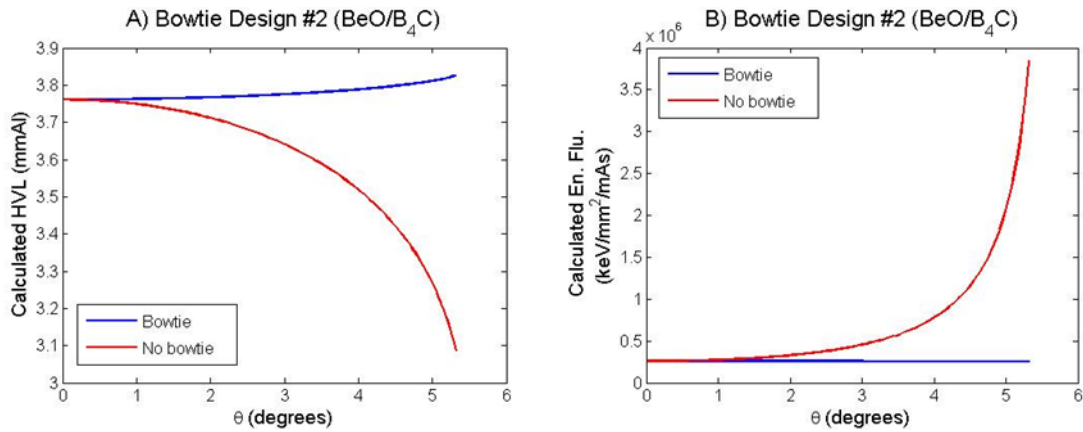
Figure 3.3: Calculated HVL (A) and energy fluence (B) as a function of fan angle with and without bowtie filter design #2.

The HVL and energy fluence were also plotted against fan-angle for bowtie design #3 (PMMA). Although this design is not expected to generate HVL or energy fluence values independent of fan-angle, the results show that the percent change in HVL from center to periphery is decreased from 24% to 11% with the inclusion of bowtie design #3 (Figure 3.4A). The dynamic range requirement is also decreased compared to the no-bowtie filter case (Figure 3.4B).
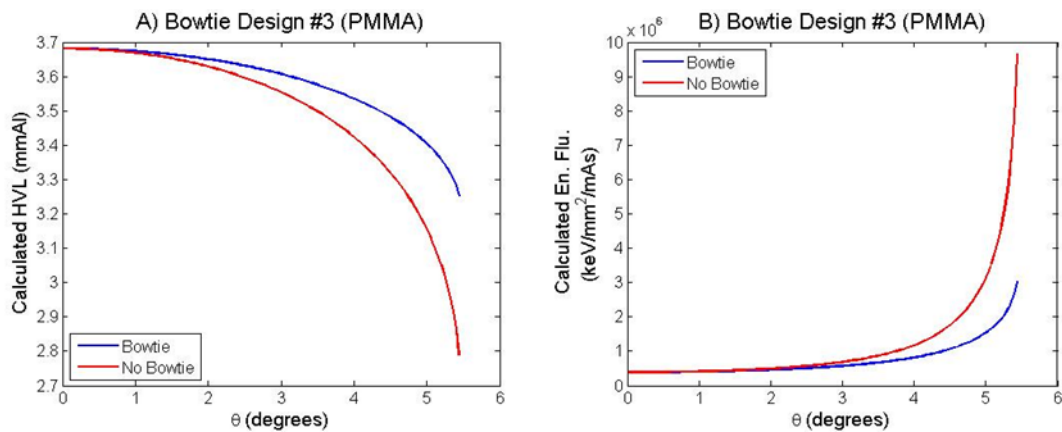
Figure 3.4: Calculated HVL (A) and energy fluence (B) as a fuction of fan-angle with and without bowtie design #3 (PMMA).

The plots of the calculated effective attenuation coefficient for all bowtie designs and the no-bowtie filter case are shown in Figure 3.5. Without the bowtie filter, there is an 8% increase in the value of the μ_{eff} from the center to periphery. This change in μ_{eff} would manifest as cupping artifacts in reconstructed images without additional corrections. Bowtie designs #1 and #2 produce variations across the phantom FOV that shows a 2.7% and 3.8% decrease in the μ_{eff} from the center to the periphery, respectively. While the use of bowtie designs #1 and #2 reduces the variation of the effective attenuation coefficient across the object FOV, there would still need to be an additional software correction applied to the calibration images to eliminate this variation that would be presented as capping in a reconstructed image. When bowtie design #3 is used in the computation, the calculated μ_{eff} at the detector is constant at all angles.
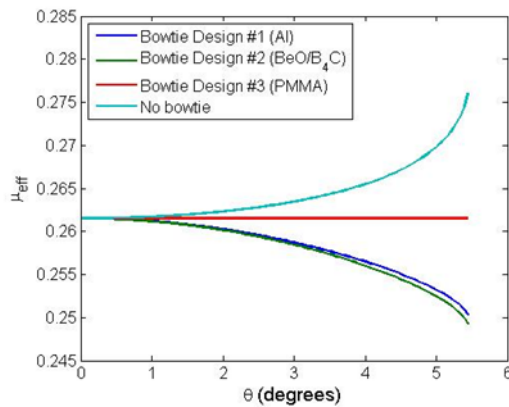
Figure 3.5: Calculated effective attenuation coefficient for all bowtie filters and the no-bowtie filter case.

3.3.1.2 Computational evaluation

The following set of figures shows the variation in the calculated values when different design input parameters were used. Figure 3.6 shows the variation in the

calculated HVL with breast composition, breast diameter, and tube voltage when using

bowtie design #1 made of aluminum.
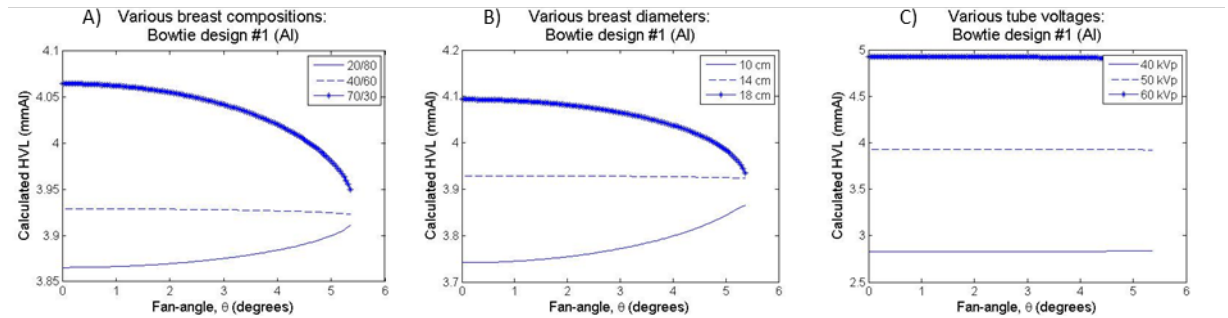
Figure 3.6: Calculated HVL for (A) various breast compositions, (B) various breast diameters, and (C) various tube voltages.

When using bowtie design #1 (Al) with different breast compositions and

diameters, there is less than a 4% change in calculated HVL from the center to the

periphery. The variation in the calculated HVL is less than 1% for tube voltages between

40 kVp and 60 kVp, showing the robustness of the design. Similar plots for bowtie

design #2 (BeO/B$_4$C) show the calculated HVL and energy fluence as a function of angle

for various breast compositions, diameters, and tube voltages (Figure 3.7).
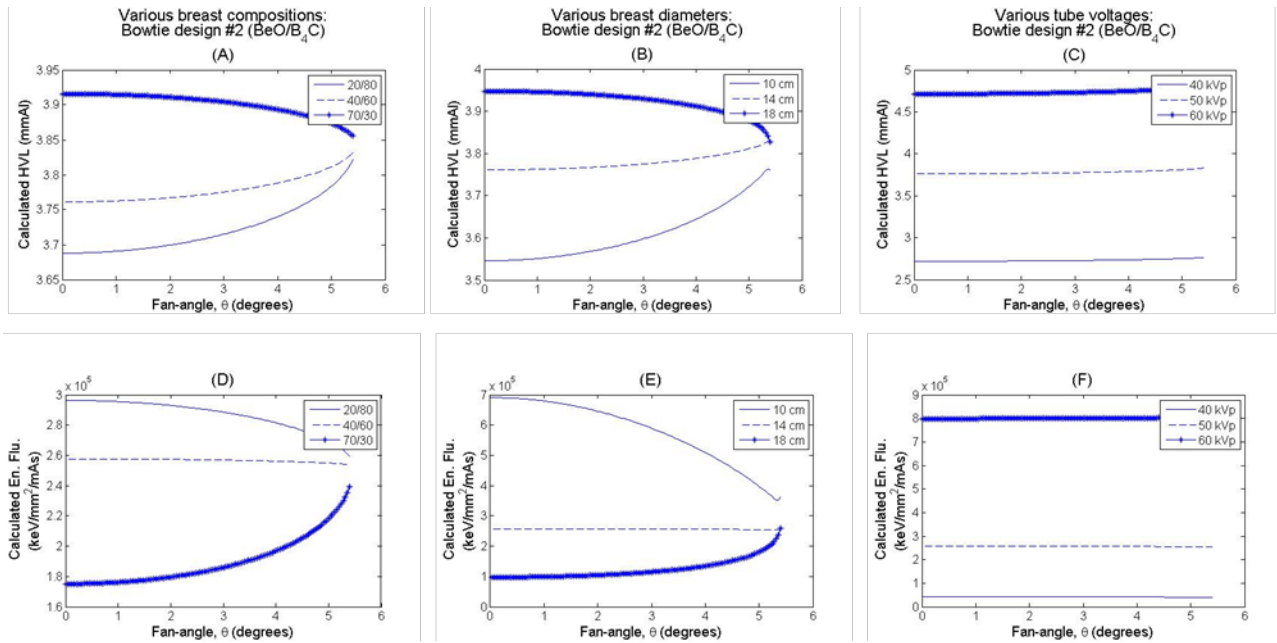
Figure 3.7: Calculated HVL and energy fluence for various breast compositions, breast diameters, and tube voltages for bowtie design #2 (BeO/B$_4$C). Plots (A) – (C) show the calculated HVL and (D) – (F) show the calculated energy fluence.

There is less than a 5.5% variation in the calculated HVL using bowtie design #2 (BeO/B$_4$C) for different breast compositions and diameters. Again, there is less than a 1% variation in the calculated HVL and energy fluence as functions of angle for different tube voltages between 40 kVp and 60 kVp. The transmitted energy fluence varies much more with different breast compositions and diameters with a maximum percent change of 50% from center to periphery occurring with a 10-cm diameter breast phantom. This value is to be compared to an energy fluence variation from center to periphery of 1400% with no bowtie filter.

The μ_{eff} as a function of angle for various breast compositions, diameters, and tube voltages for bowtie design #3 (PMMA) is shown in Figure 3.8. This design is also

47

robust against non-ideal design parameters: the μ_{eff} varies by less than 1.5% with different compositions, diameters and tube voltages used.
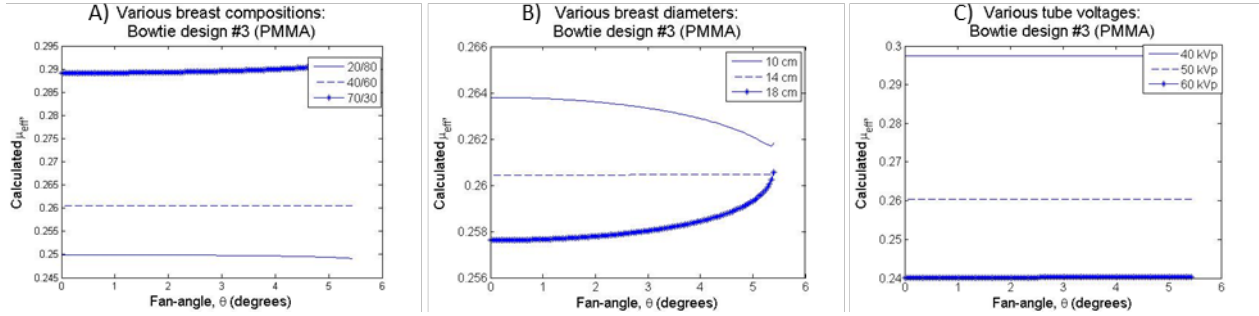
Figure 3.8: Calculated effective attenuation coefficient across object FOV for (A) various breast compositions, (B) various breast diameters, and (C) various tube voltages using bowtie design #3 (PMMA).

3.3.2 Monte Carlo validation and evaluation

The Monte Carlo x-ray transport simulation tool PENELOPE[50] with the penEasy_Imaging program[51] was used to obtain projection images of cylindrical breast phantoms. The bowtie filters were also modeled in the simulation environment using quadric geometry. A single parabola could not capture the unique curvature of the bowtie filters, so multiple parabolas were fit to multiple segments of the bowtie filters. For each projection image, 10^{10} histories were simulated using a message passing interface (MPI) code implemented on a 207 node cluster. Each simulated projection image took approximately 500 seconds to simulate. PENELOPE separates the images into primary + scatter radiation and primary radiation. Since the computational analyses assume a scatter-free case, the primary images were used in the subsequent analyses. The resulting simulated images were fed into a filtered-backprojection reconstruction algorithm.[52, 53] These reconstructed images were used to look at the line profile for each bowtie design and to analyze the noise uniformity and contrast-to-noise ratio (CNR)

homogeneity in the image with and without the bowtie filter. Dose distribution maps in the radial direction were also obtained with and without the bowtie filters.

The assumptions used in the computational analyses of the bowtie designs were translated into the simulation set-up. The bowtie shapes were placed a distance of 16.25 cm from the x-ray source with a 14 cm-diameter cylindrical tube made of PMMA placed at the isocenter 73.5 cm away from the x-ray source. The cylindrical tube was 24 cm in height and had inner and outer diameters of 13.4 and 14 cm, respectively. The tube was filled with a uniform 40/60 breast composition material. The ideal detector with a matrix of 1536 x 2048 pixels and pixel pitch of 194 µm was placed 98.5 cm away from the x-ray source, which gives a magnification of about 1.3, similar to previous simulation and experimental studies.[5, 54] Figure 3.9 shows the simulation set-up with a bowtie filter.
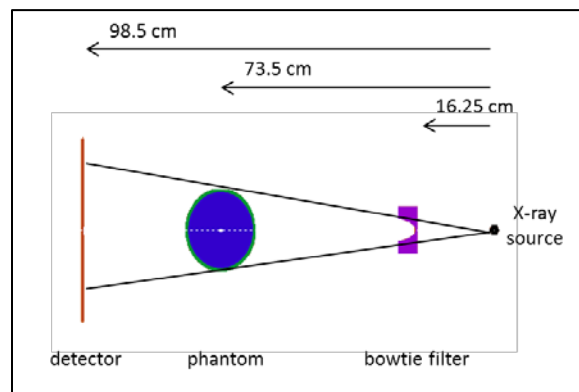
Figure 3.9: Breast CT simulation set-up.

The collimation was determined such that the largest breast diameter of 18 cm would be contained in the FOV. The fan-angle (spanning horizontally relative to the detector) and cone-angle (spanning vertically relative to the detector) for the simulations were 16.58° and 18.58°, respectively. The IPEM Report 78 spectrum of 50 kVp for a 10°

tungsten anode tube was filtered with 0.8 mm beryllium, 2 mm aluminum, and 0.1 mm copper and used as the input spectrum.

3.3.2.1 Dose distribution

PENELOPE allows the user to specify the location and size of cylindrical bins to be used in the dose distribution analysis. Since we assumed no variation in the z-direction of the phantom or bowtie filter, only the radial dose distribution was investigated. Radial bins were defined every 0.15 cm from the center of the phantom to approximately 0.5 cm outside of the phantom. The dose to each bin was given in eV/g/history. The results shown here are normalized to the dose deposited in the center of the phantom to yield arbitrary units of dose for the 14-cm diameter phantom with a 40% fibroglandular/60% adipose composition at 50 kVp (Figure 3.10). Each plot shows the bowtie filter case and the no bowtie filter case.

With all three investigated bowtie filters, the dose is reduced at the periphery of the phantom. The distribution of the dose from center to periphery is also more uniform with the use of the bowtie filters. Using bowtie design #1 (Al) and design #3 (PMMA), there is a 28.2% and 24.1% reduction, respectively, in the dose at the periphery. The dose reduction at the periphery is even more pronounced with bowtie design #2 (BeO/B_4C). Using this bowtie design, the dose profile is nearly flat and yields a 61.9% reduction in the dose. The sharp decreases toward the edge of the phantom are due to the PMMA cylinder.
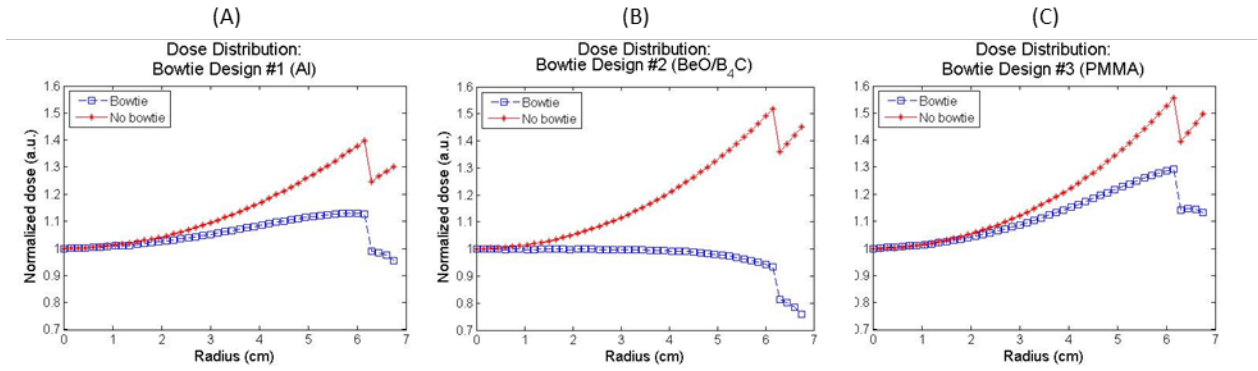
Figure 3.10: Dose profile from center to periphery of cylindrical phantom for all bowtie filter and no bowtie filter cases. Normalized dose for the 14-cm phantom at 50 kVp using bowtie design #1 (A), bowtie design #2 (B), and bowtie design #3 (C).

Compared to previous reports on peripheral dose reductions with the use of bowtie filters, the results are very similar. Lück *et al.* determined an approximate 50% dose reduction at the periphery of a cylindrical phantom with the use of a bowtie filter designed to provide a uniform noise distribution.[30]

3.3.2.2 Line Profiles

The line profile through the center of the central reconstructed slice was plotted. The central image was convolved with a smoothing kernel in order to reduce the amount of variation in the line profile. These line profiles were normalized to the maximum value which occurs at the periphery of the phantom. Figure 3.11 shows the line profile for all bowtie filter designs and the corresponding no-bowtie filter case for a 10-cm breast phantom filled with 40% glandular/60% adipose material.
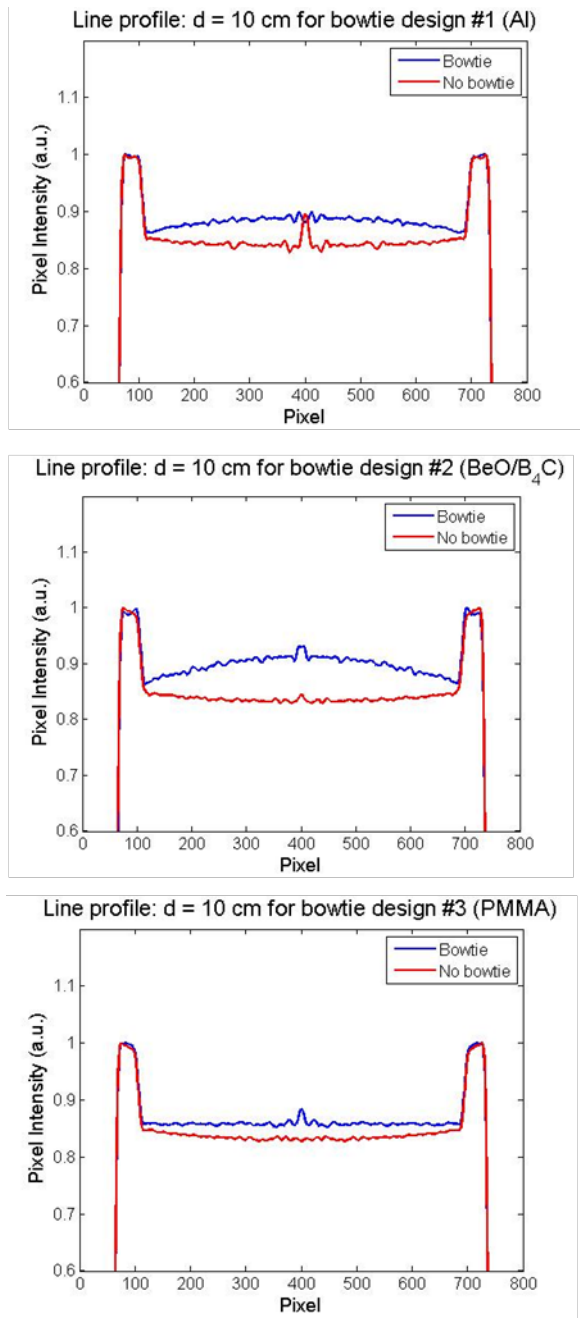
Figure 3.11: Line profiles through the center of the 10-cm phantom, plotted for bowtie design #1 (Al) (top), bowtie design #2 (BeO/B4C) (center), and bowtie design #3 (PMMA) (bottom).

With bowtie design #1 (Al) and bowtie design #2 (BeO/B$_4$C), the capping artifact that was seen in the computational analysis is seen in the reconstructed images. These line profiles become flat once an additional software correction is done to the flat-field image to correct for the beam hardening. The bottom plot of Figure 3.11 shows the line profile through the reconstructed central slice using bowtie design #3 (PMMA). As predicted by the computational results, the line profile through the slice is flat with no corrections to the flat field image. Similar results are seen for the 14-cm breast phantom and 18-cm breast phantom (Figures 3.12 and 3.13).
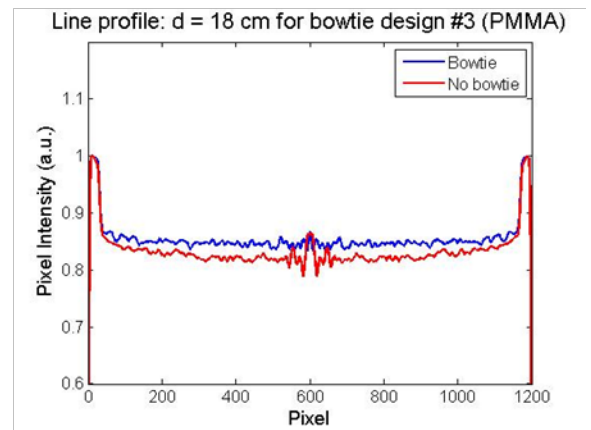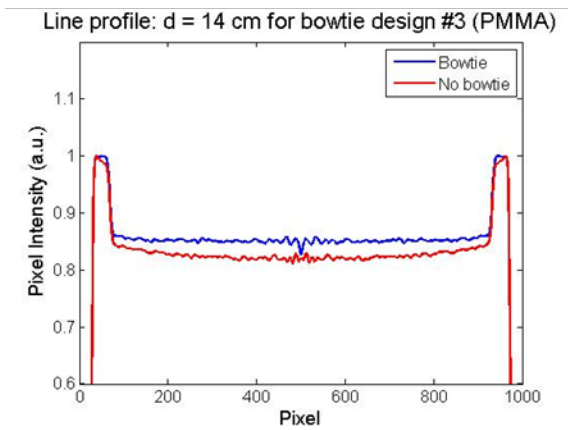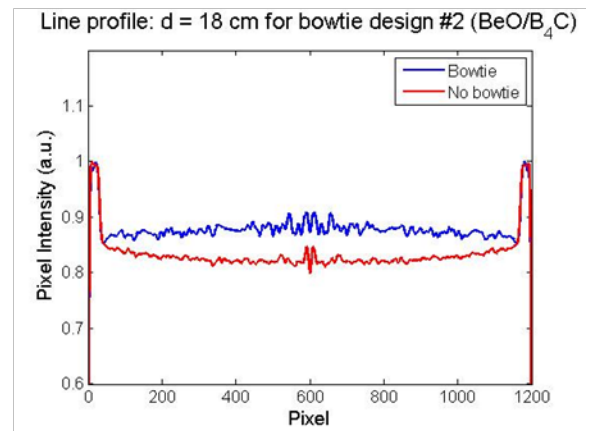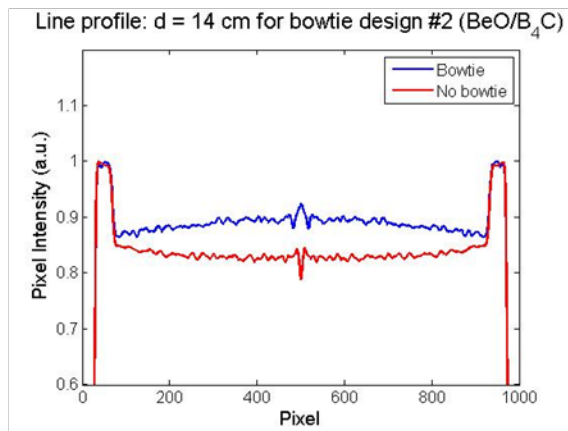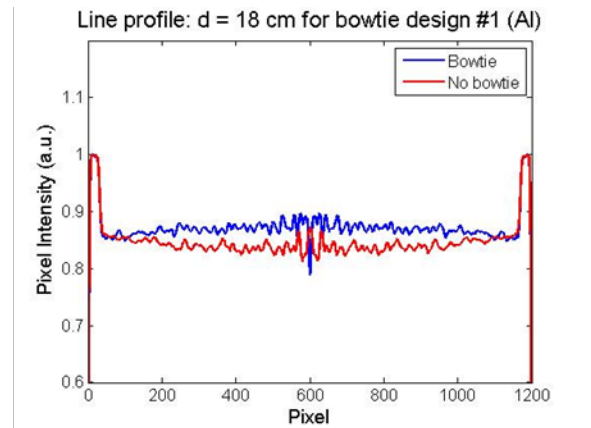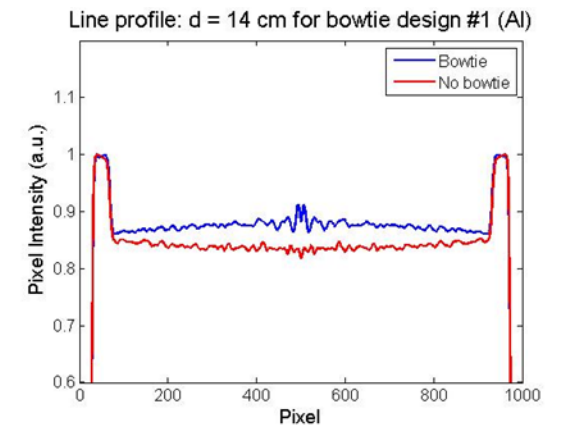
Figure 3.12: Line profiles through 14-cm breast phantom with and without bowtie design #1 (Al) (top), bowtie design #2 (BeO/B4C) (center), and bowtie design #3 (PMMA) (bottom).

Figure 3.13: Line profiles through 18-cm breast phantom with and without bowtie design #1 (Al) (top), bowtie design #2 (BeO/B4C) (center), and bowtie design #3 (PMMA) (bottom).

When comparing the line profiles for bowtie design #1 and bowtie design #2 over all breast diameters, the degree of capping decreases as the breast phantom diameter increases. This is due to the fact that the same bowtie filter designed for the 14-cm diameter phantom is used for each breast diameter by varying the SFD. The 14-cm bowtie designs slightly overcompensate for the change in path length through the 10-cm phantom, which produces more beam hardening in the flat field image. This leads to more of a capping artifact compared to the 14-cm phantom line profiles. The opposite is true of the 18-cm phantom. The bowtie design slightly undercompensates for the change in path length, so less beam hardening is occurring in the flat-field image which results in a reduced capping artifact compared to the 14-cm phantom case. For all breast diameters, bowtie design #3 produces a nearly flat line profile.

3.3.2.3 Noise uniformity index

The noise uniformity was calculated using five different volumes-of-interest (VOI). The percent difference between the center VOI and four peripheral VOI's was calculated using the equation for noise uniformity index described in Eq. 3.8.[30, 55]

$$UI = \sum_{n=1}^{4} \left(\frac{\sigma_{n,periphery} - \sigma_{center}}{\sigma_{center}} \right) * \frac{1}{4} * 100 \tag{3.8}$$

Figure 3.14 shows the placement of the VOI's on a single slice for the cylindrical breast phantom geometry designed in PENELOPE.
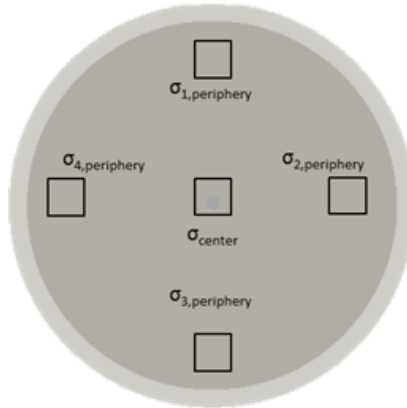
Figure 3.14: Placement of the VOI in the uniform composition breast phantom to calculate the noise uniformity index.

The results are shown in Figure 3.15. Each plot shows the noise uniformity index for the bowtie filter cases and no-bowtie filter cases for a given breast diameter.
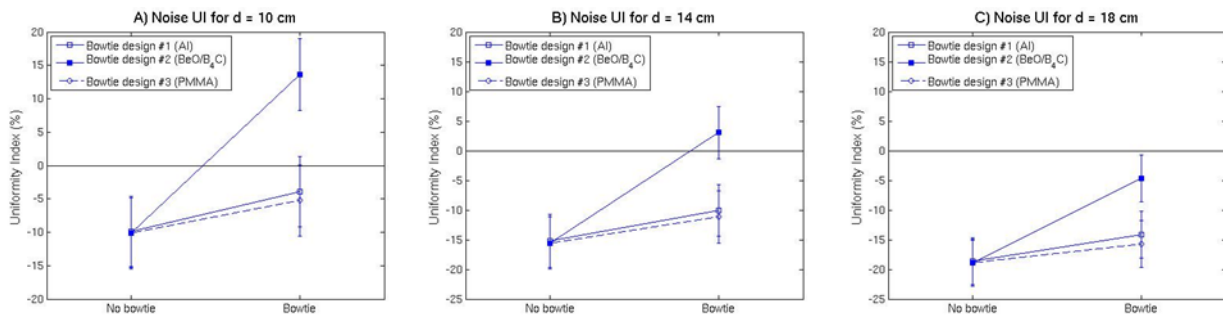
Figure 3.15: Noise uniformity index for all bowtie filter designs and no bowtie filter cases for three breast diameters. The bowtie and no bowtie case for all three bowtie filters is shown in each plot for breast diameters of (A) 10 cm, (B) 14 cm, and (C) 18 cm.

Non-uniformity in the noise without a bowtie filter arises from the variation in photon fluence that hits the detector. In the center, where the path length through the cylindrical object is greatest, the noise is increased due to a lower photon fluence. At the periphery, the path length is shorter and noise is decreased due to the increased

photon fluence. The black line at UI = 0 in each plot in Figure 16 is included as a visual reference. This is the desired case: the closer the points are to this line, the better the noise uniformity. Since bowtie design #2 (BeO/B$_4$C) simulates both the spectrum and intensity of breast tissue, it was expected that this design would show the most improvement in the noise UI. As shown in Figure 3.15B and 3.15C, this is the case for the 14-cm phantom and 18-cm phantom. The noise UI using bowtie design #2 for the 10-cm phantom is worse compared to the no bowtie filter case. The noise UI improves by approximately 5% using bowtie designs #1 (Al) and #3 (PMMA) for all breast phantom diameters.

The clinical importance of noise uniformity in low contrast detectability has been demonstrated through experimental and simulation work.[56-58] A few groups have designed bowtie filters for breast CT with the aim to achieve uniform noise distribution.[30, 59] These results indicate that noise uniformity can be achieved in addition to uniformity of other important characteristics, such as dose distribution and energy fluence.

3.3.2.4 CNR homogeneity

To evaluate the CNR homogeneity with and without the bowtie filters, the uniform phantom described above was modified to include four 7-mm diameter cylindrical inserts of 100% glandular breast composition placed from the center to the periphery of the phantom. Another set of projection images was acquired for each bowtie filter design. 300 projection images were acquired over 360° with a degree increment of 1.2° and reconstructed using the FDK filtered backprojection algorithm

previously described.[53] Four other regions the same radial distance away from the

center were used to calculate the noise in the CNR calculation. The CNR as a

function of radial distance from the center is shown in Figure 3.16 for all three bowtie
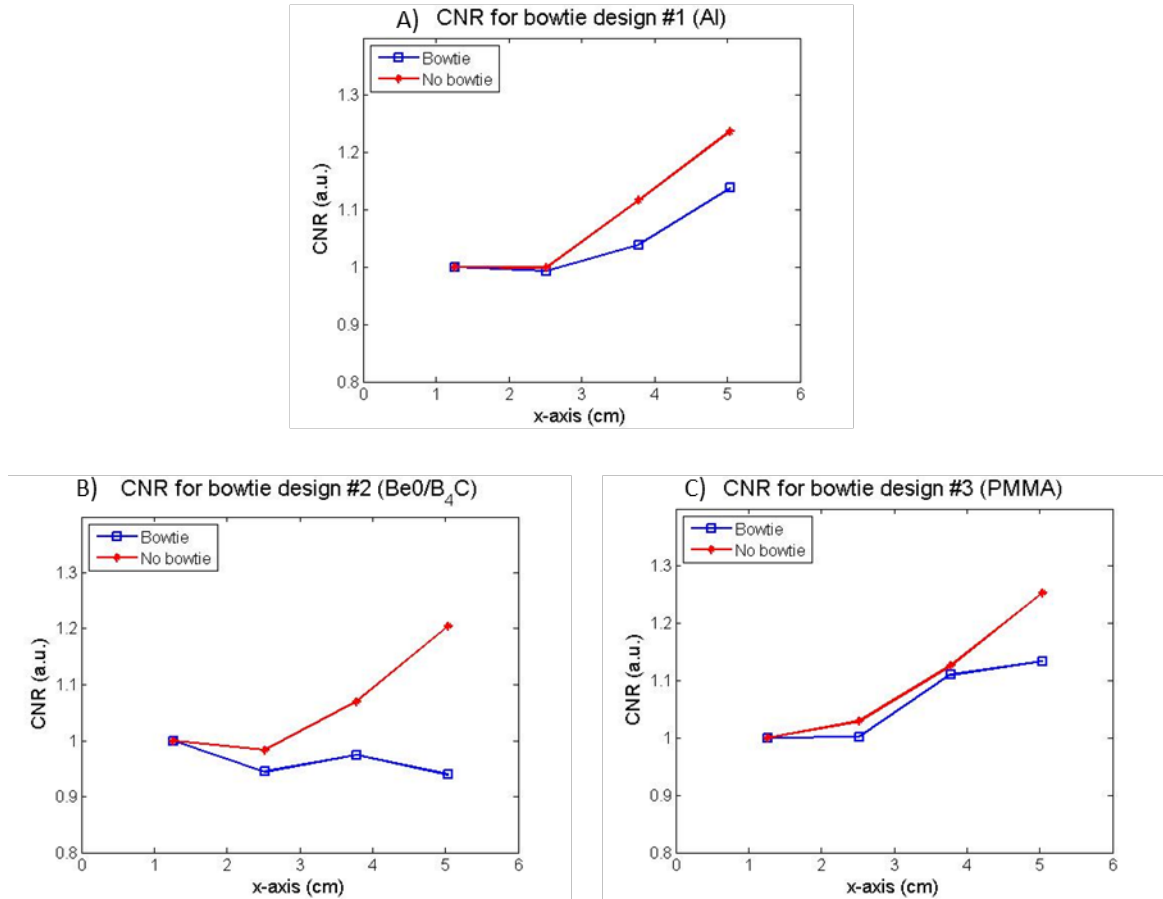
filter designs.

Figure 3.16: CNR values normalized to the innermost contrast insert value for three
different bowtie filters. These data points were calculated for the 14-cm diameter
phantom at 50 kVp.   The results are shown for (A) bowtie design #1 (Al), (B) bowtie
design #2 (BeO/B_4C), and (C) bowtie design #3 (PMMA) with the respective no-
bowtie filter cases.

Without the bowtie filter, the CNR increases by about 30% from center to

periphery. Bowtie designs #1 and #3 decrease the variation in the CNR such that the

CNR only increases about 10% from center to periphery. Bowtie design #2 maintains roughly the same CNR at all radial distances.

3.4 Discussion

All bowtie filter designs showed robustness against non-ideal design input parameters such as variations in breast composition, diameter, and tube voltage. The designs were most robust against variations in tube voltage. Since the design approaches were based on spectral matching, the design outcome was not limited to a specific energy, but applicable over a large energy range for diagnostics energies. Even if the same analyses were completed outside the specified energy range, the expectation of independence from tube voltage would still hold. Given the variability in the suggested optimal tube voltage for dedicated breast CT,[5, 6, 13, 14, 60] the use of a bowtie filter independent of tube voltage is desirable.

Among the input parameters tested, the bowtie designs were the least robust against variation in breast diameter. Varying the SFD such that the periphery of the bowtie filter matched with the ray that was tangent to the periphery of the breast phantom may not be the most appropriate placement method. The bowtie designs were designed for the 14-cm breast phantom. As mentioned in the results section, using this bowtie design with a 10-cm phantom means that the bowtie filter is overcompensating and attenuating the x-rays more than what is required. By moving the filter closer to the source, the same ray that is tangent to the breast phantom will travel through less material since the bowtie filters get thinner toward the center. Lück *et al.* conducted an optimization study by varying the SFD in small increments

and measuring the noise UI and dose reduction. [30] Their results showed the optimal

SFD for various breast diameters could be determined to achieve uniform noise and

dose reductions up to 30%. The bowtie designs in the present study have other design

goals besides dose reduction and noise uniformity (i.e. constant energy fluence, HVL,

effective attenuation coefficient), so a more comprehensive study of all the

parameters would need to be done to determine the optimal SFD for different breast

diameters. Even with this optimization of filter placement, the fact that various sizes

of bowtie filters for varying breast diameters may produce better results in terms of

image quality and dose to the patient cannot be ignored. Just as body CT scans utilize

different size bowtie filters when imaging patients of different sizes,[61, 62] breast CT

may be optimized by employing two or three different size filters to cover the range

of breast diameters seen in the clinic.

Using the bowtie filters designed for the 14-cm breast phantom to analyze the

noise uniformity for a 10-cm breast phantom may also help to explain why the UI

using bowtie design #2 is worse than the no-bowtie filter case. The 14-cm bowtie

filter design is thicker toward the periphery than is required for the 10-cm phantom,

which causes more photons to be attenuated than necessary. The decrease in photon

fluence toward the periphery causes an increase in the noise, leading to the +15%

noise uniformity index.

The dose reduction achieved with bowtie design #1 (Al) and bowtie design #3

(PMMA) was similar to results seen in previous studies.[29, 30] The largest peripheral

dose reduction of approximately 60% was seen with bowtie design #2 (BeO/B_4C).

The dose profile was also constant from the center of the phantom to the periphery.

This was the expected result since the two-material design is able to accurately represent the attenuation characteristics of breast tissue in terms of intensity and spectrum. With this bowtie filter, it appears as if we have imaged a uniform block in the projection view. This can be seen by looking at the projection views of the 14-cm phantom using all three bowtie filters (Figure 3.17). The edges of the phantom can easily be seen near pixels 100 and 1050 in the x-direction with bowtie designs #1 and #3 projection views (Figure 3.17A, 3.17C). With bowtie design #2, the signal intensity beyond the phantom is similar to the signal intensity within the phantom since the bowtie filter accurately represents the attenuation characteristics of breast tissue (keeping in mind the fact that the bowtie filters are extended to a length of 80 mm) (Figure 3.17B).
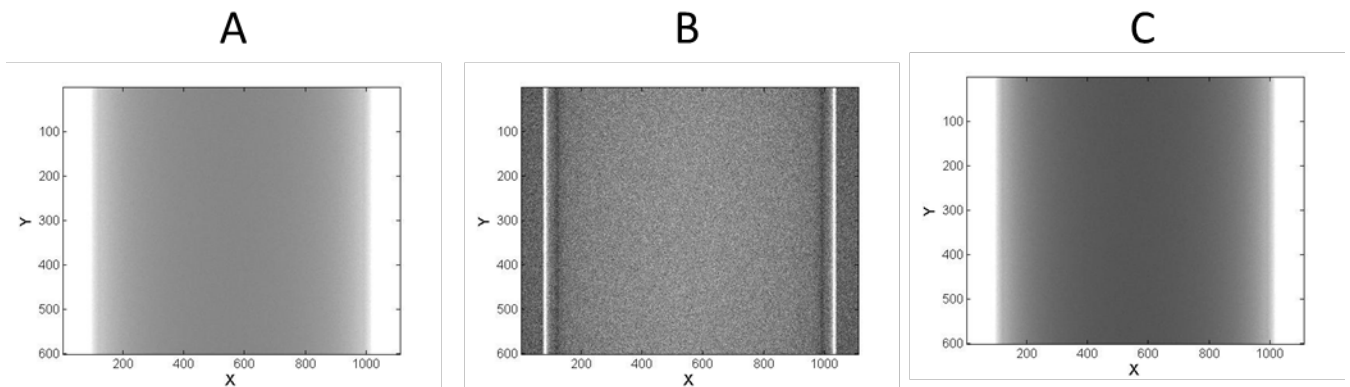
Figure 3.17: Projection views of the 14-cm phantom with (A) bowtie design #1, (B) bowtie design #2, and (C) bowtie design #3. Due to the extension of the bowtie filter at the maximum thickness, the signal intensity in the projection view beyond the phantom for bowtie design #2 is the same as the intensity within the phantom. This is another validation of the bowtie filter design.

From looking at the projection views with the three different bowtie filters, one important design flaw was revealed. In Figure 3.17B, there are two distinct lines that appear at the edges of the phantom. This feature was only evident in the bowtie

design #2 projection images because of the reasons discussed above. The bowtie filters are designed with sharp edges toward the periphery. This sharp edge is most likely the cause of the artifact seen in the projection images. Redesigning the bowtie filter such that the edges are rounded may alleviate this problem.

The CNR variation from center to periphery was calculated to be as large as 30% without the use of a bowtie filter. With the inclusion of bowtie design #2 (BeO/B_4C), there was less than a 5% variation in the CNR from center to periphery. Similar results were seen from Lück *et al*.[30]

The bowtie filter materials used in this study were chosen based on practical considerations. Aluminum and PMMA are readily available, which makes manufacturing of the bowtie filters for experimental comparisons possible, and the materials provide appropriately sized filters such that they may fit into existing scanners. Although these materials provide reasonable results, they may not be the optimal materials. One characteristic of the bowtie filters is the ability to decrease the dynamic range requirement on the detector. The selection of material will change the dynamic range. With bowtie design #3, for example, two materials can be used. The ratio of thicknesses between those two materials will control the dynamic range. This type of control over the dynamic range may be beneficial for systems using photon counting detectors. [12, 45, 46]

The goal of this study was to introduce three new bowtie filter designs, validate the designs through computational and simulation analyses, and perform some initial evaluation of the designs with non-ideal design input parameters. Future work will focus on the material of the bowtie filters and optimization of SFD for

various breast diameters (which will also change depending on the material selected), as well as the design of an anthropomorphic bowtie filter to take into account the change in breast diameter in the z-direction.

Chapter 4: Computational and simulation analysis of materials for bowtie filter designs

4.1 Introduction

Over the last several years, research groups have been investigating a new imaging modality for breast cancer detection called dedicated breast CT.[5, 6, 8, 13, 14] Dedicated breast CT provides better low contrast detectability and improved breast lesion location than conventional digital/screen-film mammography while maintaining similar dose to the breast as two-view mammography.[10, 63, 64] Since the shape of the breast is relatively symmetric and the tissue composition is more homogeneous compared to other regions of the body, dedicated breast CT may permit the design of bowtie filters that compensate for the variations in the object being imaged in a more detailed fashion than is the case with bowtie filters in conventional CT.

Several groups have suggested the use of a bowtie filter in dedicated breast CT due to its ability to reduce the dose to the patient, reduce the scattered radiation at the detector, and reduce the dynamic range requirement on the detector. [12, 29, 30] Our group has designed three different types of bowtie filters that can mimic certain x-ray characteristics of breast tissue or produce a constant effective attenuation coefficient at the detector.[65] Bowtie designs #1 and #2 use the ideas of spectral matching and

basis material decomposition to match either the transmitted spectral shape of breast tissue using a single material design or to match both the transmitted spectral shape and intensity of transmitted radiation through the breast using a two material design. Bowtie design #3 produces the same effective attenuation coefficient at the detector. Experiments and simulations to evaluate and validate each of the bowtie filter designs are ongoing. Initial results indicate that the bowtie filters accomplish the desired result.[66]

In the previous evaluation of these three bowtie filter designs, only one bowtie filter was modeled for each design type. Bowtie design #1 was modeled using aluminum, bowtie design #2 was modeled using beryllium oxide/boron carbide, and bowtie design #3 was modeled using PMMA. The selection of the material is important for each design type. Ideally, the material would be higher in density and lower in atomic number composition so that the size of the bowtie filter is not so small that it cannot be manufactured, but not so large that it will not be able to fit into existing scanners. There are also several other considerations to take into account when selecting the material for a given bowtie design such as the resulting dynamic range requirement on the detector, the fluence distribution across the object FOV, the dose distribution throughout the object, and the scatter. Different materials will affect these parameters in different ways. We describe here a methodology for analyzing the effects on these parameters of choosing different bowtie filter materials for each bowtie design.

One of the advantages of bowtie filter implementation is the reduction of the dynamic range requirement on the detector and ability to produce a more uniform

fluence at the detector. [16, 19, 61] These traits are especially important given the recent technological advancements in the development of energy resolved detectors. Several groups have developed and investigated the use of photon counting detectors in general purpose CT and x-ray (XR) imaging. [46, 67-70] Most of these detector technologies are still in the developmental stage for CT and XR imaging, but due to the size, shape and general uniformity of the breast, some detector technologies are applicable to breast CT.[12, 30, 71, 72] Regardless of the application, these photon counting detectors suffer from pulse pile-up due to high fluence rates that can degrade energy resolution and require the dynamic range to be lower than normal energy integrating detectors.[46, 67, 68] The selection of the materials in the three proposed designs will vary the dynamic range requirement on the detector and also the flux rates, so incorporating the dynamic range and fluence distribution as parameters of interest when analyzing different materials for our bowtie filter designs is necessary.

Dedicated breast CT has several advantages over mammography, one being that the dose delivered to the breast is more spatially uniform.[8, 73] Studies have also shown that with the inclusion of a bowtie filter in dedicated breast CT, the dose distribution can be even more spatially invariant due to the reduction of fluence at the periphery of the breast.[30] However, since the fluence distribution will vary depending on the material selection for each bowtie design, the dose distribution as a function of radius of the breast will also vary with the material. To ensure that the selected material for a given bowtie filter design achieves the desired goal of uniform dose distribution, the dose distribution should also be included as a parameter of interest.

Since dedicated breast CT employs a cone-beam geometry, scattered radiation can contribute a substantial amount of noise in the images. Bowtie filters are also used to reduce the amount of scattered radiation at the detector. [74-77] Bowtie filters made of different materials will vary in their shape/thickness, and also vary in the scatter cross-section. A certain material may be more likely to cause scattered radiation within the bowtie filter itself, so an analysis of how the scatter is affected with various materials of our bowtie designs needs to be done.

A few other research groups have developed bowtie filters specifically for dedicated breast CT.[29, 30] Kwan *et al*. created a bowtie filter made of Teflon that accurately transmits the same intensity as 50% fibroglandular/50% adipose breast tissue for photons at 50 keV.[29] Lück *et al*. designed two different bowtie filters that focus on uniform dose distribution and noise distribution, respectively.[30] Four different materials were used in the design of those bowtie filters: Teflon, aluminum, carbon, and copper. As mentioned previously, the new bowtie designs used in this study have not undergone a thorough material analysis to determine how the dynamic range, dose, noise, and scatter are affected. The goal of this study is to develop a methodology to analyze our bowtie designs with different materials to help determine the best material and design to be used.

4.2 Methods

4.2.1 Over view of bowtie filter design approach

The bowtie filter designs have been previously described in Chapter 3, Section 3.2.1. The only difference between the designs described in Chapter 3 and those used

in this material analysis study is the added thickness base: for the material analysis study, no added thickness base was used.

4.2.2 Computational analysis

Using Matlab programming, the computational environment was created to mimic the dedicated breast CT geometry. A 14-cm diameter phantom was used with a breast composition of 40% fibroglandular/60% adipose. The source-to-filter (SFD) and source-to-object (SOD) distances were 16.25 cm and 73.5 cm, respectively. Table 4.1 summarizes the parameters used in the computational analysis.

Table 4.1: Initial design parameters for three bowtie filter designs

Design parameter	Value
Breast diameter	14 cm
Breast composition	40/60
SFD	16.25 cm
SOD	73.5 cm

IPEM Report 78 spectra were manipulated according to Eq. 10 and 11 to generate transmitted spectra as a function of energy and fan-angle, and values of energy fluence as a function of fan-angle. The fan-angle variable (θ) spanned from -5.44° to +5.44° with an increment of 0.04°. In these equations, the incident spectrum (I_0) was the same as described above. The linear attenuation coefficient of the bowtie material and phantom material are μ_{bt} and μ_{phan}, respectively. The pathlengths a given photon at angle θ would need to travel through the bowtie filter material and the phantom are given by t_{bt} and p, respectively. With these variables, the transmitted spectrum behind the phantom was sampled 273 times across the object FOV.

$$I_t(E, \theta) = I_0 e^{-\left[\mu_{bt}(E) * t_{bt}(\theta) \, + \, \mu_{phan}(E) * p(\theta)\right]} \tag{4.1}$$

$$E_{flu}(\theta) = \int_0^{Emax} I_0 * e^{-\left(\mu_{bt}(E) * t_{bt}(\theta) + \mu_{phan}(E) * p(\theta)\right)} dE \tag{4.2}$$

4.2.3 Simulation analysis

Using the Monte Carlo x-ray transport code PENELOPE[50] with the penEasy_Imaging main program[51], representations of each of the bowtie filters were created and inserted into the dedicated breast CT simulation environment. The same parameters that were applied to the computational environment in Table 4.1 were used in the simulation geometry. The detector used in the simulations was an ideal detector with 1536 x 2048 pixels covering a detector FOV of 30 cm x 40 cm. The pixel pitch was 0.194 mm. The fan-angle and cone-angle were 12.58° and 18.58°, respectively. These parameters allowed complete coverage of a 14-cm diameter cylindrical phantom that was approximately 24 cm in height. The phantom consisted of a hollow PMMA cylinder with 3 mm wall thickness that was filled with a liquid matching the attenuation properties of 40/60 breast tissue material as defined by the composition data of Hammerstein *et al.*[39] The x-ray tube, phantom, and detector were placed so that the projection of the focal spot through the center of the phantom coincided with the center of the detector. Figure 4.1 shows the simulation set-up with a bowtie filter.
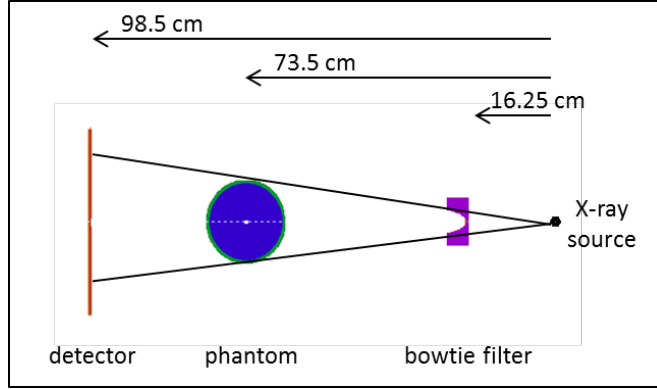
Figure 4.1: Breast CT simulation set-up.

With 10^{10} photons simulated per projection, 300 projection images were acquired over 360° for each bowtie filter and a no-bowtie filter case. These images were used in a Feldkamp, Davis and Kress filtered backprojection reconstruction algorithm to obtain a reconstructed volume.[52, 53] The noise uniformity was calculated using five different volumes-of-interest (VOI). The percent difference between a center VOI and four peripheral VOI's was calculated and then averaged according to the equation for noise uniformity index described in Eq. 4.3.[30, 55]

$$UI = \sum_{n=1}^{4} \left(\frac{\sigma_{n,periphery} - \sigma_{center}}{\sigma_{center}} \right) * \frac{1}{4} * 100 \qquad (4.3)$$

PENELOPE allows the user to specify the location and size of cylindrical bins to be used in the dose distribution analysis. Since there is no variation in the z-direction of the phantom or bowtie filter, only the radial dose distribution was investigated. Radial bins were defined every 0.15 cm from the center of the phantom

to approximately 0.5 cm outside of the phantom. The dose to each bin was given in eV/g/history.

PENELOPE also is able to separate primary photons hitting the detector from scattered photons. Using these data, the spatially dependent SPR can be calculated for each bowtie filter and the no-bowtie filter case using a method similar to that described in Kwan *et al.*[29] A small rectangular region of dimensions 1536 x 50 pixels spanning the center of the scatter image horizontally was divided into several sub-regions. The same sub-regions were defined in the primary-only images. The pixel values in each sub-region of the scatter image were averaged, and divided by the average value of the pixels in the corresponding sub-region in the primary-only image to obtain the SPR as a function of horizontal distance across the object FOV. This was repeated for all 300 projection images, and the results were averaged to obtain the SPR with associated error.

4.3 Results

4.3.1 Bowtie filter designs

When determining the shape of the bowtie filter for designs #1 and #2, thickness ratios were mathematically determined according to Eqs. 3.1-3.3. The ratios for bowtie design #1 are listed in Table 4.2.

Table 4.2: Thickness ratio calculated for all investigated materials for bowtie design #1. The name of the material and the chemical composition is given in the first column.

Material	Calculated a_1
Aluminum (Al)	0.051
Boron Carbide (B_4C)	1.15
Beryllium Oxide (BeO)	0.28
Copper (Cu)	0.00147
Polyethylene (C_2H_4)	1.825
PMMA ($C_5H_8O_2$)	0.645
Teflon (C_2F_4)	0.24

Since seven materials were initially investigated in this study, there were 21 possible combinations for the two-material bowtie design #2 filter assuming that the order of the materials did not matter and the same material could not be used twice in the same design. For several of the possible combinations, the algorithm computed a negative value for one of the materials in order to achieve the design outcome of transmitting the same spectral shape and intensity as breast tissue. While this is a perfectly reasonable result from a mathematical standpoint, physical implementation is impossible. Therefore, only 12 possible combinations were investigated for bowtie design #2. The materials and the calculated thickness ratios are listed in Table 4.3.

Table 4.3: Thickness ratios for bowtie design #2 materials.

Material 1 (Outer filter)	Material 2 (Inner filter)	Calculated a_1	Calculated a_2
Boron Carbide	Copper	0.4519	0.0008
Boron Carbide	Aluminum	0.4317	0.0274
Boron Carbide	Teflon	0.313	0.1625
Beryllium Oxide	Boron Carbide	0.29	0.11
Polyethylene	Copper	0.9958	0.0007
Polyethylene	Aluminum	0.9496	0.024
Polyethylene	Beryllium Oxide	0.3247	0.253
Polyethylene	Teflon	0.313	0.1625
PMMA	Copper	0.75	0.0002
PMMA	Aluminum	0.8348	0.0053
PMMA	Beryllium Oxide	0.5852	0.1151
PMMA	Teflon	0.7775	0.0412

The bowtie filters were created in Matlab. To compare the size and shape of each bowtie filter, the cross-section profile was plotted in the following figures. The profiles for the possible combinations for bowtie design #2 were split into three different plots for easier viewing (Figure 4.3). The profile above the line y = 0 represents material 1 listed first in the legend entry. The profile below the line y = 0 represents material 2 listed second in the legend entry.
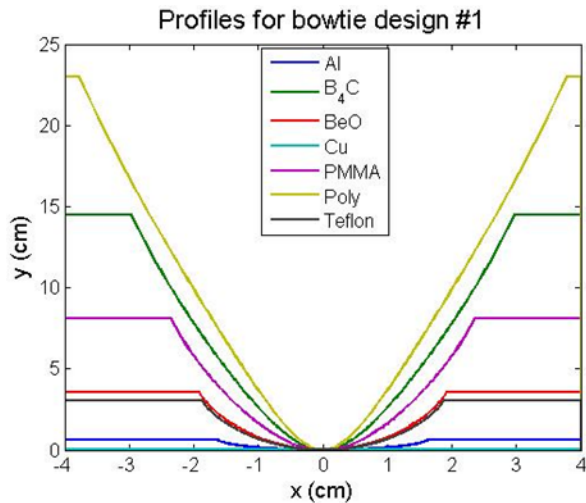
Figure 4.2: Cross-section profile of bowtie design #1 materials using seven different investigated materials.

The material that creates the thickest bowtie filter design for bowtie design #1 is polyethylene. At the maximum thickness, the polyethylene bowtie filter is 23.01 cm. The low atomic compositions makes polyethylene a good material for the bowtie filter designs, but the lower density of 0.94 g/ml requires the filter thickness to be very large in order to achieve the bowtie filter design goal. On the other hand, copper creates the thinnest bowtie filter design with a maximum thickness of 0.01853 cm. The higher atomic number and higher density of 9.8 g/ml of copper require the bowtie filter to be very thin. There are a few materials that combine the ideal characteristics of low atomic composition and high density to create bowtie filter that are reasonable in size. Aluminum, for example, has a maximum thickness of 0.6429 cm. Beryllium oxide and Teflon both have similar shapes for bowtie design #1, with a maximum thickness of 3.53 cm and 3.026 cm, respectively.

The filter shapes for bowtie design #2 also vary depending on the two materials being used (Figure 4.3). As seen with bowtie design #1, using copper with

74

bowtie design #2 produces a very thin filter thickness due to the higher atomic composition and high density of copper. The combination of PMMA and aluminum also requires a very thin filter thickness of aluminum. All other material combinations, however, produce machine - feasible designs, meaning it is possible to manufacture the bowtie filter shapes. Again, the bowtie filters for design #2 that use polyethylene have a larger maximum thickness compared to other material combinations, which would make implementation of this design difficult in existing dedicated breast CT scanners.
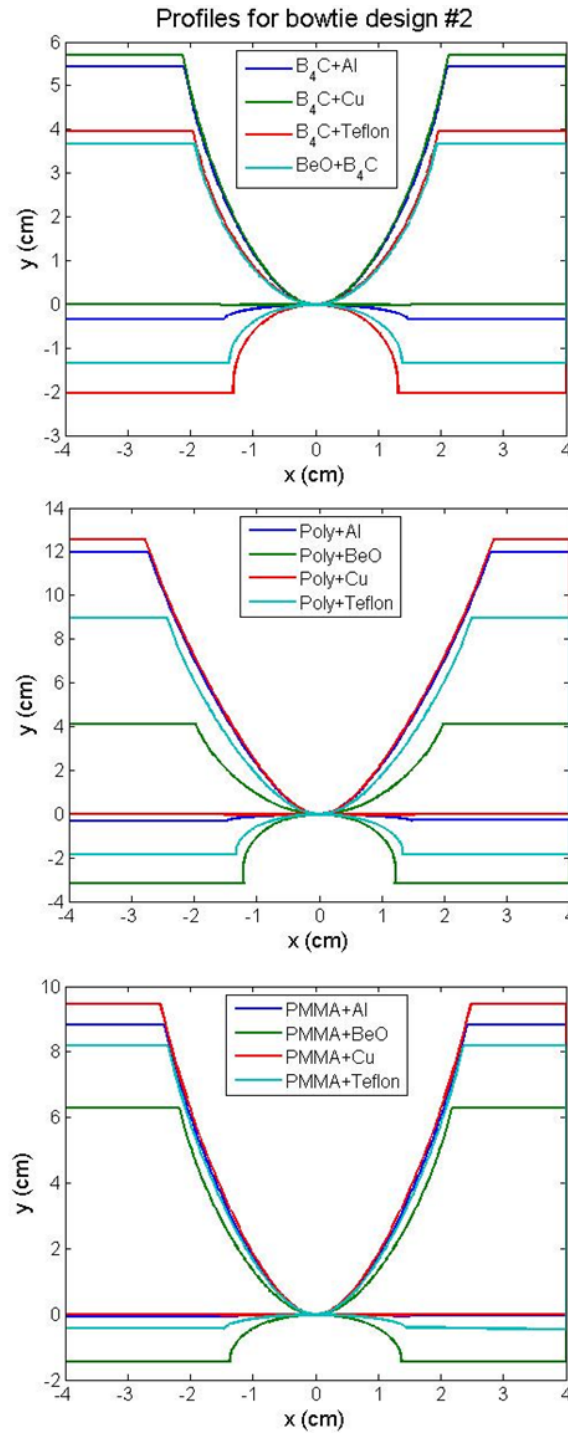
Figure 4.3: Cross section profile of bowtie design #2. The profiles of the 12 possible combinations from the seven materials being investigated were plotted in three different plots for easier viewing. Each bowtie filter combination is listed as a legend entry. The first material in the legend entry is plotted as a colored line above $y = 0$. The second material in the legend entry is plotted as the same colored line below $y = 0$.
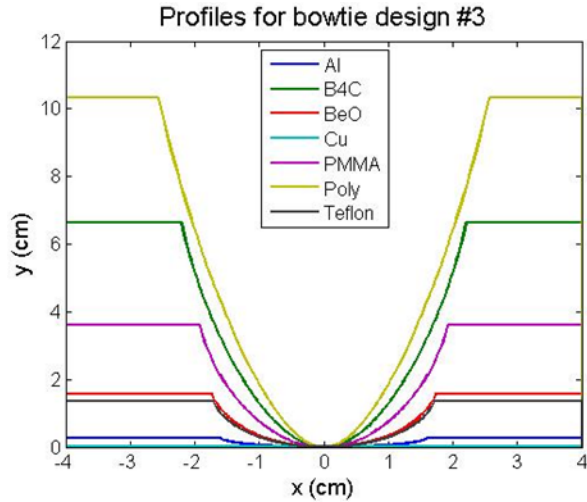
Figure 4.4: Cross section profile for bowtie design #3 using seven different investigated materials.

Similar design results are seen for bowtie deign #3 using all materials (Figure 4.4). Polyethylene creates the largest thickness while copper creates the smallest thickness filter. The maximum thickness of the largest filter for bowtie design #3 is less than half of the maximum thickness of the largest filter for bowtie design #1.

4.3.2 Dynamic range calculations

The energy fluence was calculated as a function of fan-angle for all materials and all three different bowtie filter designs to examine the reduction in the dynamic range requirement. Figure 4.5 shows these data compared to the no-bowtie filter case.

The dynamic range is defined as the ratio between the largest value of energy fluence and the smallest value of energy fluence. Without a bowtie filter, the dynamic range was calculated to be about 25. For both bowtie design #1 and #3, the

use of any bowtie filter material reduces the dynamic range. The greatest reduction

for bowtie design #1 is seen when using BeO. The dynamic range is approximately

1.77 when using this filter material and design. For bowtie filter design #3, the

greatest reduction in dynamic range is seen using B_4C, with a value of 1.15.
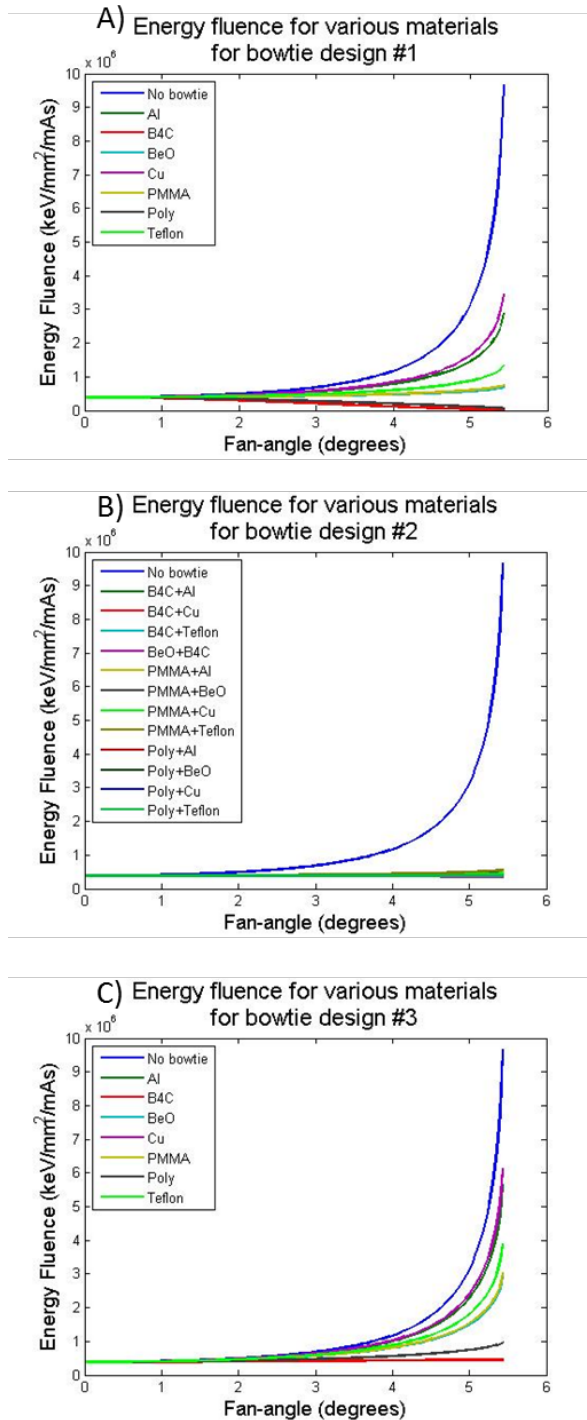
Figure 4.5: Energy fluence as a function of fan-angle plotted for three different bowtie filters using different materials to examine the dynamic range requirement. These plots show the energy fluence after the photons have traveled through the bowtie filter and the phantom. (A) Bowtie design #1 energy fluence for all materials. (B) Bowtie design #2 energy fluence for all different possible material combinations. (C) Bowtie design #3 energy fluence for all materials.

Another benefit to these bowtie filter designs is the ability to tailor the dynamic range. By adding another material to bowtie design #1 or bowtie design #3, the dynamic range can be specified while still maintaining the desired outcome of each respective bowtie filter. Figure 4.6 shows the energy fluence as a function of angle, θ, for bowtie design #3 made of PMMA and polyethylene. The dynamic ranges were calculated to be 7.84 and 2.50 for the PMMA and polyethylene bowtie design #3 filters, respectively. If it was desirable to achieve a dynamic range between those two values, combining the two materials in the appropriate ratios could achieve such a goal while still keeping the effective attenuation coefficient constant. By taking a fraction of the full bowtie thickness of the PMMA bowtie filter for bowtie design #3, the thickness of polyethylene needed to satisfy the design constraint in Eq. 3.9 can be iteratively determined. Depending on the fraction of the PMMA bowtie design #3 used, the resulting two-material design using PMMA and polyethylene can have a dynamic range between 2.50 and 7.84. In this example, 15% of the original PMMA bowtie design #3 was used, resulting in a maximum thickness of 5.5 cm of polyethylene. The resulting dynamic range was 4.88 (Figure 4.6).
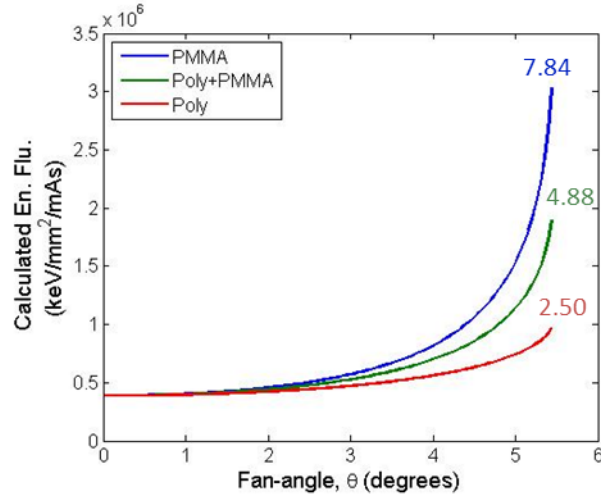
Figure 4.6: Demonstration of the flexibility of bowtie design #3 in specifying the dynamic range. The calculated energy fluence for bowtie design #3 made of PMMA and polyethylene as a function of fan-angle are shown, as well as the achieved dynamic range with the combination of PMMA and polyethylene. The numbers next to each line show the dynamic range.

4.2.3 Dose distribution

The dose distribution as a function of radial distance from the center was calculated for all three bowtie filter types and all different materials. The results in Figure 4.7 show the dose normalized to the dose at the center of the phantom. Since the cylindrical phantom that is modeled in PENELOPE contains a finite thickness of PMMA surrounding the breast tissue material, there is a sharp drop off that is seen between r = 6.15 and 6.3 cm.

With the inclusion of the bowtie filters, the peripheral dose is decreased for all bowtie filter types and all different materials compared to the no-bowtie filter case. When using bowtie design #2, the dose distribution is nearly uniform for all material combinations (Figure 4.7B). A uniform dose distribution was also obtained using certain materials of bowtie designs #1 and #3 (Figure 4.7A and 4.7C). For example,

bowtie design #1 made of BeO had less than a 3% change in the dose from center to periphery and bowtie design #3 made of B_4C had less than a 2% change in the dose from center to periphery.   The bowtie design and material that produced the greatest change in dose compared to the no-bowtie filter case was bowtie design #1 made of B_4C. The dose decreased as a function of radial distance from the center of the phantom, leading to a maximum dose reduction of 54% at the periphery.
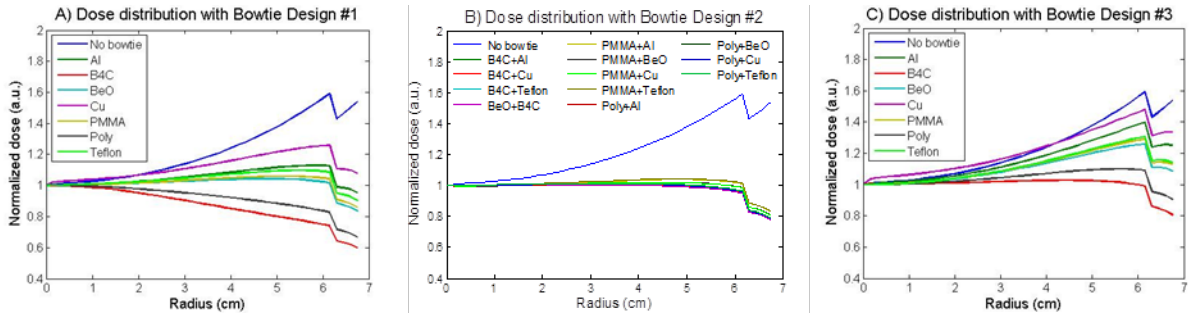
Figure 4.7: Dose distributions as a function of radial distance from the center of the phantom for (A) bowtie design #1, (B) bowtie design #2, and (C) bowtie design #3, using various materials. The y-axis is the dose normalized by the dose value at the center of the phantom.

4.3.4 Noise uniformity

The noise uniformity index (UI) was calculated using the reconstructed images from the primary-only simulation projection images. A positive value means that the noise at the periphery of the phantom was higher than the noise at the center. A negative value means that the noise at the periphery was less than the noise at the center. The results are shown in Figure 4.8. The black line at UI = 0 in each plot in Figure 4.8 is included as a visual reference. This is the desired case: the closer the points are to this line, the better the noise uniformity.
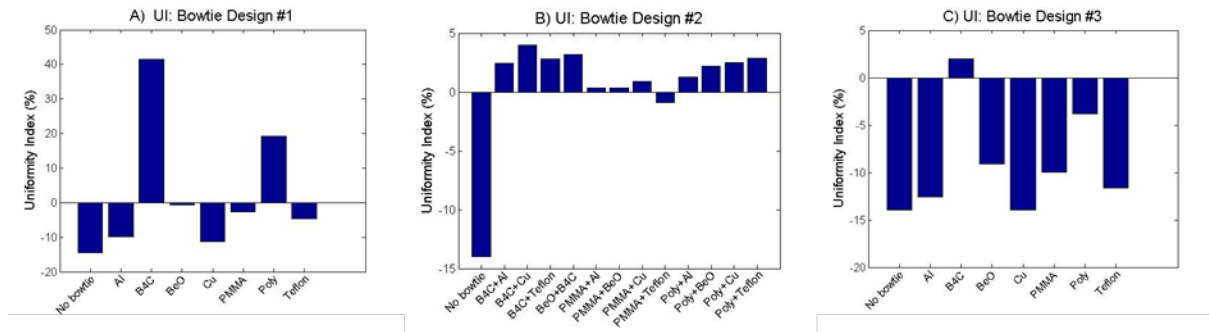
Figure 4.8: Noise uniformity index for (A) bowtie design #1, (B) bowtie design #2, and (C) bowtie design #3 with various materials.

Bowtie design #2 yields a noise UI very close to the line UI = 0, meaning there is the least amount of noise variation from the center to periphery when using this particular design regardless of the chosen materials. The noise UI comes very close to zero for other bowtie filer designs as well. Bowtie design #1 made of BeO, for example, yields a noise UI of -0.57%. Bowtie design #3 made of B$_4$C yields a noise UI of 1.99%.

Most of the chosen materials for each different bowtie design show an improvement in the noise UI compared to the no-bowtie filter case which varies by -14%. There are a few cases that show degradation in the noise UI for bowtie designs #1 and #3, however. Bowtie designs #1 made of B$_4$C and polyethylene show an increase in the noise UI from the no-bowtie filter case. Bowtie design #3 made of copper also shows an increase in the noise UI compared to the no-bowtie filter case.

4.3.5 Scatter

The SPR was calculated for each bowtie filter type with each different material. The results are shown in Figure 4.9. The x-axis of the plots represents the

horizontal distance across the phantom. The line x = 0 corresponds to the center of

the phantom. The no-bowtie filter case is shown for each different bowtie filter type.

The associated error with the scatter calculations was less than 1×10^{-2}, so the error

bars in the following plots were omitted.
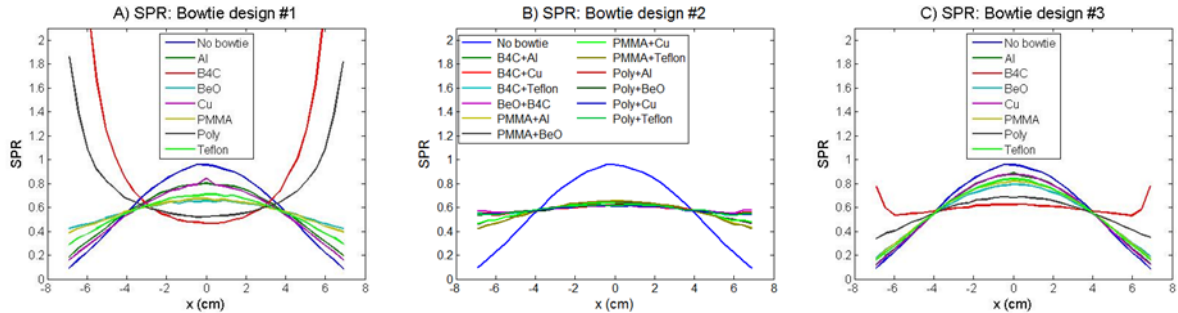
Figure 4.9: SPR calculated from simulated projection data for (A) bowtie design #1,
(B) bowtie design #2, and (C) bowtie design #3 for various materials.

With the inclusion of any bowtie filter type made of any of the materials used

in this study, the SPR is reduced at the center of the phantom. A maximum decrease

in the SPR of 51% at the center of the phantom was obtained using bowtie design #1

made of B_4C compared to the no-bowtie filter case (Figure 4.9A). However, this

same bowtie filter yields very large SPR values toward the periphery of the phantom.

To examine this further, the averaged scatter and primary pixel intensity values from

the simulated projection images that were used to compute the SPR were plotted for

all bowtie filter materials of design #1 and the no-bowtie filter case. Figure 4.10A

shows that the scatter signal for each bowtie filter material has the same general

shape, with the maximum scatter signal at the center of the phantom. The primary

signals shown in figure 4.10B, however, are not the same for all materials. B_4C and

polyethylene both decrease the primary signal at the periphery of the phantom, while

other materials show an increase in the primary signal. Given the results in figure

4.5A showing the decrease in energy fluence as a function of fan-angle for bowtie

design #1 made of B_4C and polyethylene, this result is expected.
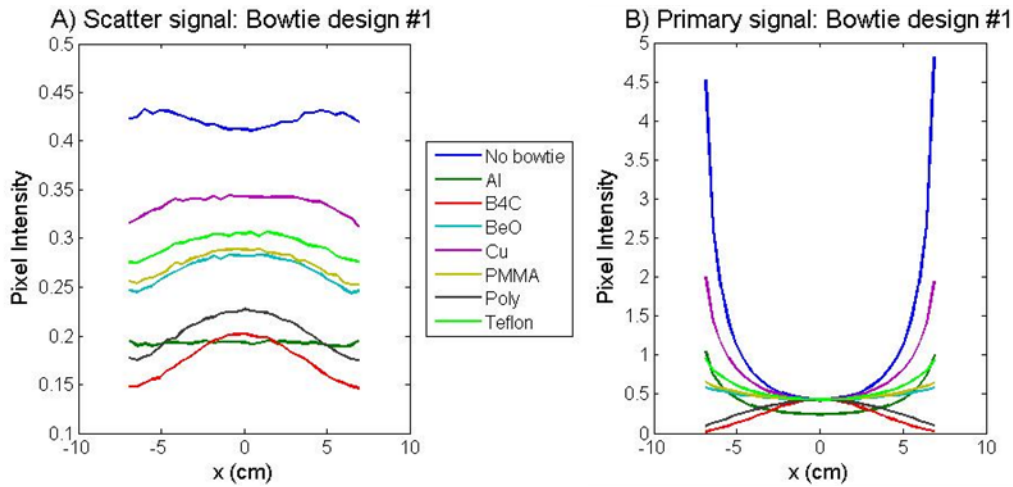
Figure 4.10: Scatter and primary signal from simulated projection images using various materials for bowtie design #1. (A) The averaged scatter signal over all projection images as a function of horizontal distance across the phantom for different materials. (B) The averaged primary signal over all projection images as a function of horizontal distance across the phantom for different materials.

4.4 Discussion

The development of dedicated breast CT systems that incorporate an energy-

resolved detector in the imaging chain[30] is at an early stage, but as the technology

improves, more dedicated breast CT systems may employ this feature due to its many

advantages. With the advances in energy-resolved detector technology comes the

need to control certain aspects of the incident beam upon the detector, such as the

fluence distribution. One way to achieve this control is through the use of bowtie

filters. Bowtie filters are also advantageous for systems that use energy integrating

detectors due to their ability to reduce dose to the patient, reduce scatter, and improve noise uniformity. Three different types of bowtie filters have been designed to achieve the previously mentioned goals, but each design outcome will vary depending on the material of the bowtie filter. The goal of this work was to evaluate each bowtie filter design using different materials to get an idea of what kinds of materials provide the best results in terms of energy fluence distribution, dose reduction, scatter reduction, and noise uniformity.

For some of the materials chosen, the bowtie thickness is required to be very large to achieve the design goal. The thickest bowtie filter design was design #1 made of polyethylene. The maximum thickness was about 23 cm. Implementation of a bowtie filter of this size would be difficult in the existing scanner geometries. The smallest bowtie filter thickness of 0.018 cm resulted from bowtie design #1 made of copper. Accurate manufacturing of this design would also be very difficult, given the size. The performance of bowtie filters made of these materials was poor in some areas compared to other materials. For example, bowtie designs #1 and #3 made of copper had very poor dose distributions compared to the results obtained from other materials (Figures 4.7A and 4.7C). Also, the noise UI for bowtie design #1 made of polyethylene was worse than the noise UI for the no-bowtie filter case (Figure 4.8A). Materials with either very large or small atomic number compositions and very high or low densities are not suitable as materials with the specific bowtie designs used in this study.

Bowtie design #2 is meant to transmit the same spectrum and intensity as breast tissue, which was shown in this study to lead to a uniform energy fluence

distribution, uniform dose distribution, and spatially uniform noise. This design does require two materials that can be somewhat bulky. From the results presented in this study, there exists the possibility of selecting a material for bowtie designs #1 and #3 (both single material designs) that achieve the same design goals as the two-material bowtie design #2. Bowtie design #1 made of BeO and bowtie design #3 made of B_4C both achieve an energy fluence distribution that is nearly independent of fan-angle (Figure 4.5A and 4.5C). In looking at the bowtie filter profiles in Figure 4.2 and Figure 4.4, the sizes of both of these filters are reasonable for manufacturing purposes and implementation in existing scanners.

The noise UI was improved for nearly all bowtie filter types and materials. For bowtie design #2, all material combinations generated reconstructed images with noise uniformity better than the no-bowtie filter case. For bowtie design #1, all materials except for B_4C and polyethylene gave better results than the no-bowtie filter case. B_4C and polyethylene yielded a noise UI of 41% and 19%, respectively. These results can be explained by looking at the energy fluence as a function of fan-angle for bowtie design #1 (Figure 4.5A). The energy fluence decreases with increasing fan-angle for those two materials, which means there are fewer photons hitting the phantom and detector at the periphery. This causes the noise level to increase in a non-linear fashion at the periphery. The percent change in energy fluence from the center to periphery was -96.7% for bowtie design #1 made of B_4C and -84.2% for bowtie design #1 made of polyethylene. Due to the larger negative percent change in energy fluence for B_4C, the noise UI is greater.

The ability of the bowtie filter to reduce the scattered radiation incident upon the detector is shown from the results in Figure 4.9 and Figure 4.10A. The selection of material and design has a large effect on the amount of scatter reduction that can be obtained. Depending on how the bowtie filter distributes the energy fluence across the phantom, the SPR could suffer. All materials for bowtie design #2 yielded a nearly uniform SPR as a function of horizontal distance across the phantom since this bowtie design generates a uniform fluence distribution. With certain materials used in bowtie design #1, however, the SPR increased rapidly toward the periphery of the phantom. In terms of scatter reduction and uniform SPR distribution, materials with characteristics similar to BeO and PMMA would work well when implementing bowtie designs #1 and #3.

These bowtie filters are designed for a specific breast that is 14 cm in diameter and contains 40% fibroglandular/60% adipose breast tissue. Since women being imaged with breast CT will present with breasts of different shapes and compositions, the ability to design a bowtie filter that achieves all the desired design goals and is also specific to the patient would be desirable. Any of these bowtie designs can be generated for different breast diameters and compositions. One can imagine a situation where the patient comes in to a clinic for breast imaging and undergoes a scout scan to obtain necessary dimensions of the breast and some information about the breast density that will be used as input to design a bowtie filter. This design could then be fed into a 3D printing machine to create a patient-specific bowtie filter. The materials available for use in current 3D printing machines are limited, but investigation of these materials and their performance in energy fluence distribution,

dose distribution, noise uniformity, and scatter reduction would be a step forward

toward personalized medicine in breast imaging.

Chapter 5: Characterization of scatter magnitude and distribution in dedicated breast CT with bowtie filters

5.1 Introduction

The majority of the dedicated breast CT systems undergoing clinical evaluation employ a cone-beam configuration.   Several investigators have characterized scatter in clinical cone-beam CT imaging and have concluded that scatter contributes to image artifacts (such as cupping), increases noise, and decreases the contrast-to-noise ratio (CNR). [78, 79] Given the unique features of dedicated breast CT, the conclusions from studies on general cone-beam CT imaging may not be applicable, so that further investigation is needed. A few groups have done such an investigation by looking at the scatter-to-primary ratio (SPR) and scatter profile for different breast compositions, breast diameters, air gap distances, and tube voltages in dedicated breast CT. [29, 77, 80] These studies found that tube voltage and breast composition had little impact on SPR values. Breast diameter and air gap were the most significant parameters impacting SPR. It was also concluded that the best way to reduce the SPR in the center of the phantom is through the use of a compensator filter, or bowtie filter. [29]

Bowtie filters are designed to deliver a more uniform fluence at the detector in order to reduce the dynamic range requirement on the detector, preferentially harden the x-ray beam, and reduce the dose to the patient. [12, 17, 19] These types of filters are already used in conventional CT scanners. In general, bowtie filters

achieve the goal of reducing the dynamic range in the radiation intensity reaching the detector by acting as a complement or inverse of the patient, i.e., where the ray path through the patient is highly attenuating, the bowtie filter has low attenuation, and vice versa. Due to the lack of symmetry of the human body and to the large differences in attenuation properties of bone and soft tissue, it is not feasible to design bowtie filters that compensate for the patient in a detailed fashion. In dedicated breast CT systems, however, only the breast is irradiated. Given the homogeneity of the tissue in the breast and its symmetry, a bowtie filter that more precisely compensates for the x-ray characteristics of the breast can be designed.

Our group has designed three different types of bowtie filters that can match certain x-ray characteristics of breast tissue or produce a constant effective attenuation coefficient at the detector.[65] Bowtie designs that we have previously referred to as #1 and #2 use the ideas of spectral matching and basis material decomposition to match either the transmitted spectral shape of breast tissue using a single material, or to match both the transmitted spectral shape and intensity of transmitted radiation through the breast using two materials. For this study, bowtie design #1 was made of aluminum and bowtie design #2 was made of beryllium oxide (BeO) and boron carbide (B_4C). Bowtie design #3, which produces the same effective attenuation coefficient at the detector, was made of polymethylmethacrylate (PMMA). Experiments and simulations to evaluate and validate each of the bowtie filter designs are ongoing. Initial experimental and computational results indicate that the bowtie filters accomplish the desired result with regard to the primary (unscattered) beam.

Given the degrading effects of scatter in cone-beam CT images, it is important to understand the consequences and advantages of integrating these bowtie filters into the dedicated breast CT imaging scheme. Several studies have examined the effect of bowtie filters on the distribution and magnitude of x-ray scatter in general cone-beam CT.[74, 75, 81] Results from one study in cone-beam CT using a copper bowtie filter show that the scatter signal is significantly diminished and the horizontal scatter profile is flattened out.[74] The decrease in the structure of the spatial distribution of the scatter caused by the bowtie filter may be beneficial in certain scatter techniques where the scatter is assumed to be contained primarily in the low-frequency portion of the projection images.[74] This report describes our evaluation of the scatter effects of the particular bowtie designs we have developed.

5.2 Methods

5.2.1 Phantoms

5.2.1.1 Experiments

Hollow cylindrical breast phantoms constructed of PMMA[82] were filled with a liquid simulating the x-ray characteristics of 40% glandular/60% adipose composition breast tissue.[21] Research has shown the average fibroglandular percentage of the female breast to be as low as 20%[47], while other studies have cited 50% as the average.[5, 13, 48] The breast composition of 40% fibroglandular/60% adipose that was used to design the bowtie filters described in this paper falls in between these two values. The clinical work by Boone *et al.* showed that 95% of the uncompressed breast diameters from a cohort of 200 women were between

approximately 10 cm and 18 cm, with the average breast diameter being 14 cm.[44]

For this reason, the bowtie filters were designed for a 14-cm diameter cylindrical

phantom, and three phantoms were used with outer diameters of 10 cm, 14 cm, and

18 cm and a PMMA wall thickness of 0.3 cm.

5.2.1.2 Simulations

Since the liquid mixture used in the physical phantom matched the x-ray

characteristics of a breast with composition based on the Hammerstein data to within

0.5% in the energy range of interest[20, 21, 83], the phantoms in the simulation were

modeled in PENELOPE using the breast composition data from Hammerstein *et al.*[39]

The 0.3 cm PMMA shell was also modeled in the simulation geometry. The x-ray

source, phantom, and detector were positioned such that the projection of the focal

spot through the center of the phantom coincided with the center of the detector.

5.2.2 Bowtie filters

The choice of material for each bowtie filter was based upon the availability

and the ease of fabrication of the given material. The beam-hardening properties and

densities of the materials affect the size and shape of the resulting filters. In order to

design a filter that is not too large to fit into clinical scanners or too small to

manufacture, a material composed of relatively low atomic number elements and

having a high density is desired. Aluminum and PMMA are two materials that

produced reasonably sized filters. These two bowtie designs were implemented in

both the experimental and simulation analyses. Figure 5.1 shows images of bowtie

design #1 (Al) and bowtie design #3 (PMMA) that were studied experimentally.
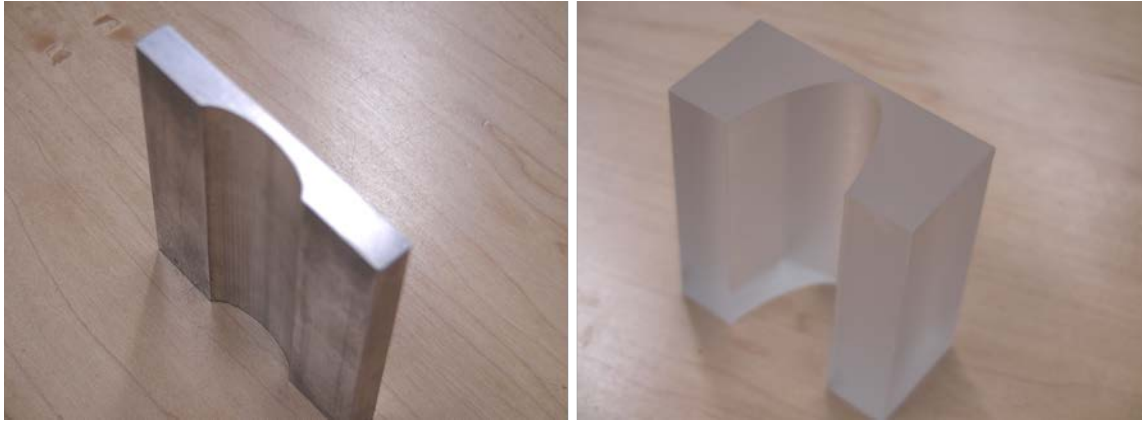
Figure 5.1: Images of the two bowtie filters used for experimental analysis of scatter in dedicated breast CT. (Left) Bowtie design #1 made of aluminum that transmits the same quality of radiation as breast tissue. (Right) Bowtie design #3 made of PMMA that yields the same effective attenuation coefficient at the detector.

Bowtie design #2 was computationally modeled using BeO and B_4C. These

materials are commercially available but quite expensive and also require specialized

fabrication techniques, so an experimental version was not made. These materials

were considered because their low atomic number compositions and higher densities

resulted in reasonably sized filters that could be implemented experimentally in the

future. For this study, the two-material bowtie design #2 filter made of BeO/B_4C

was only implemented in simulations. Figure 5.2B shows the cross section profile of

this bowtie filter. The cross section for bowtie designs #1 and #3 are shown in

Figures 5.2A and 5.2C, respectively.
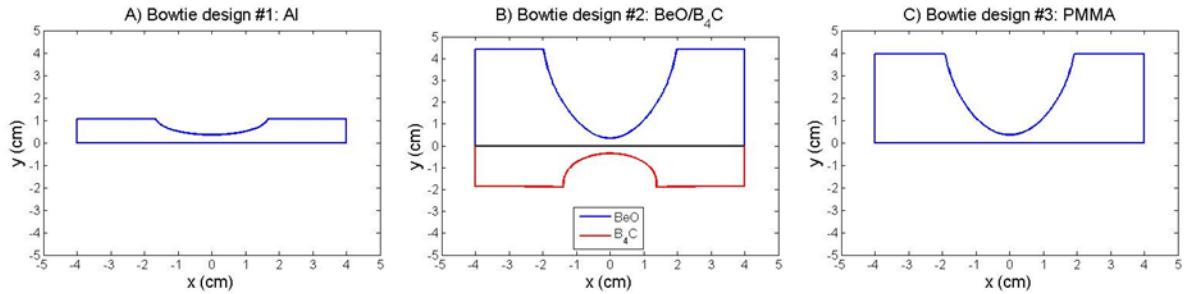
Figure 5.2: Cross-section views of the bowtie filter designs using (A) aluminum for bowtie design #1, (B) BeO/B$_4$C for bowtie design #2, and (C) PMMA for bowtie design #3.

5.2.3 Dedicated breast CT system

5.2.3.1 Experimental set-up

During a dedicated breast CT scan, the patient lies in the prone position with their breast hanging through a hole in the patient support couch as the x-ray tube and detector assembly rotate around the pendant breast. Our laboratory simulator of this configuration[84] uses a Varian G1582-BI rotating tungsten anode x-ray tube and Varian PaxScan 4030CB detector with 0.194 mm pixel pitch. Cylindrical phantoms are placed on a rotation stage in the x-ray field. The source-to-object distance (SOD) and source-to-detector distance (SDD) were held constant for all experiments at 73.5 cm and 98.5 cm, respectively.

The bowtie filter designs of all three types were based on the 14 cm phantom. This was based on the assumption that only a single bowtie would be employed in a clinical system. For the 10 and 18 cm phantoms, the source-to-filter distance (SFD) was changed so that the projection of the edges of the bowtie filter matched up with the projection of the periphery of the breast phantom. Table 5.1 shows the SFDs for three breast diameters.

Table 5.1: SFD for three different breast diameters

Breast Diameter	Source-to-filter distance
10 cm	28.4 cm
14 cm	16.25 cm
18 cm	14.9 cm

5.2.3.2 Simulation set-up

The simulation geometry was designed to match the experimental conditions so that a direct comparison between the SPR measurements could be made. The half cone-angle and fan-angle of the x-ray beam used in the simulation were 9.29° and 8.29°, respectively, to irradiate the entire breast phantom for all diameters. Just as in the experimental conditions, the bowtie SFD was adjusted depending on the diameter of the breast phantom. The Monte Carlo simulations used the PENELOPE code[50] with the penEasy_Imaging main program.[51] This program uses quadrics to represent the geometry in the simulation. A single parabola could not capture the unique curvature of the bowtie filters, so multiple parabolas were fit to multiple segments of the bowtie filter. For each projection image, 10^{10} histories were simulated using a message passing interface (MPI) code implemented on a 207 node cluster. Each simulated projection took approximately 1350 seconds.

5.2.4 X-ray source spectrum

Our computational analysis of the optimal tube voltage for dedicated breast CT indicates that lower tube voltages will provide the best contrast-to-noise ratio while also maintaining appropriate dose levels. [85] The Varian G-1582BI x-ray tube, in combination with our CPI Indico x-ray generator has a lower kVp limit of 40; therefore, tube voltages of 40 kVp, 50 kVp, and 60 kVp were investigated experimentally. In the simulations, a tube voltage of 30 kVp was also investigated since tube output was not an issue.   Starting spectra were taken from IPEM Report 78 assuming a 10° tungsten anode for each tube voltage (Figure 5.3). Each simulated spectrum was filtered with 0.8 mm of beryllium and 1 mm of aluminum to match the inherent filtration in the x-ray tube. A 0.1 mm copper filter was also placed in the x-ray beam.
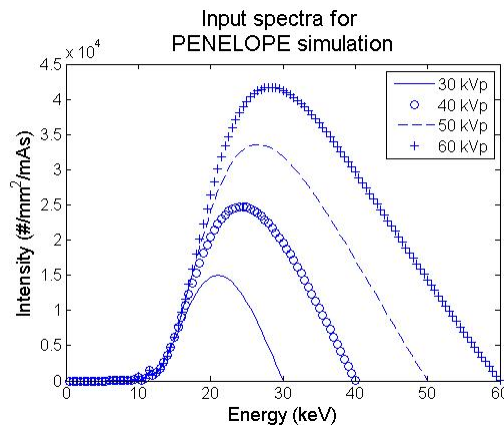
Figure 5.3: Number of simulated photons per energy bin for each simulated tube voltage.

5.2.5 SPR and scatter distribution

The SPR was experimentally measured in the x-direction using the lead strip beam block method.[29, 86, 87] Since the initial bowtie filters are not designed to account for variations in the z-direction, only the SPR in the x-direction was measured. A rectangular lead strip with dimensions 2 mm x 250 mm x 3 mm thick was sandwiched between two thin sheets of PMMA, and placed in the x-ray beam between the bowtie filter and phantom (Figure 5.4).
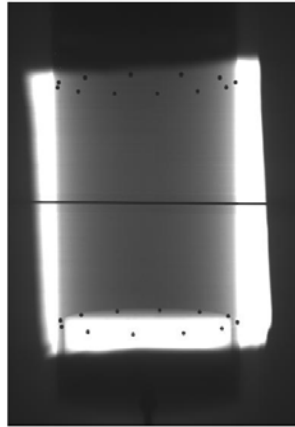
Figure 5.4: Experimental projection image using the lead strip beam block method.

Two sets of images were acquired: one with the lead strip and one without the lead strip. These projection images were dark-field corrected, and regions of interest (ROI) in the projection of the lead beam block in both images were averaged and analyzed to determine the SPR as a function of distance across the detector according to the following equation:

$$SPR(x) = \frac{\xi_S(x)}{\xi_{P+S}(x) - \xi_S(x)} \tag{5.1}$$

In this equation, x is the horizontal distance across the detector, ξ_S is the gray-scale pixel value of the beam block projection image, and ξ_{P+S} is the gray-scale pixel value of the primary + scatter image without the beam block.

The Monte Carlo code PENELOPE is capable of generating images without scatter, with scatter, and also images from individual types of scatter events (i.e. Compton, Rayleigh, etc.). Using these images, the SPR can easily be calculated over the detector FOV. To match the experimental methodologies, however, a lead beam block strip with the same dimensions as the strip used experimentally was included in the geometry of the simulation in the x-direction. The SPR was then calculated according to Eq. 5.1, using the same size ROI's.

Information on the scatter distribution was obtained using the simulation images. Bootsma *et al.* introduced a scatter ratio relationship that helps to highlight subtleties in the scatter signal that might otherwise be overwhelmed by the primary signal in the SPR.[74] The scatter-to-open-field center pixel ratio (SOCR) looks at the ratio of the scatter only signal (S) and the central pixel value in the flat-field image (I_{open}^0) where no object attenuation occurs (Eq. 5.2). To compute this ratio, the scatter signal image was re-binned from a 1536 x 2048 image to a 48 x 64 image. In Eq. 5.2, x' and y' represent the bin number of the re-binned images.

$$SOCR(x', y') = \frac{S(x', y')}{I_{open}^0} \tag{5.2}$$

The ratio was computed for all diameter phantoms for all three bowtie filters and no-bowtie filter cases for the 50 kVp simulation. The resulting bowtie/no bowtie images that correspond to the projection of the cylindrical phantom were shown on the same scale.

5.3 Results

5.3.1 SPR dependency on tube voltage

The SPR was calculated for three different tube voltages in the experiments, and for four different tube voltages in the simulations. Figure 5.5 shows the experimental SPR values obtained with the 10 cm breast phantom with and without bowtie design #1 and bowtie design #3. The 10 cm phantom results were used because the limits of the tube output did not allow for accurate SPR measurements for the 14 cm and 18 cm diameter phantoms at low tube voltages.
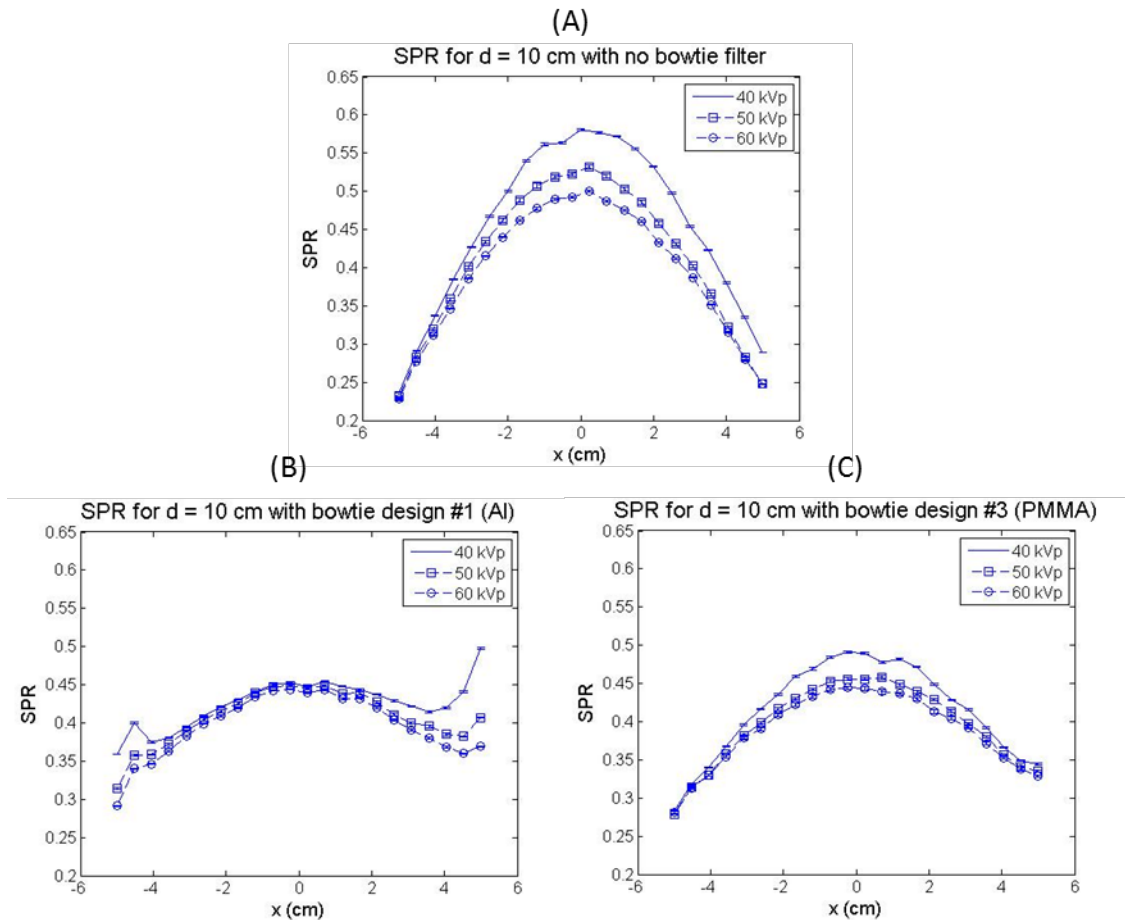
Figure 5.5: Experimental SPR values for various tube voltages using (A) no-bowtie filter, (B) bowtie design #1 and (C) bowtie design #3.

Figure 5.6 shows the SPR calculations from the simulated images for the 10 cm breast phantom as a function of tube voltage.

(A)   (B)

(C)   (D)
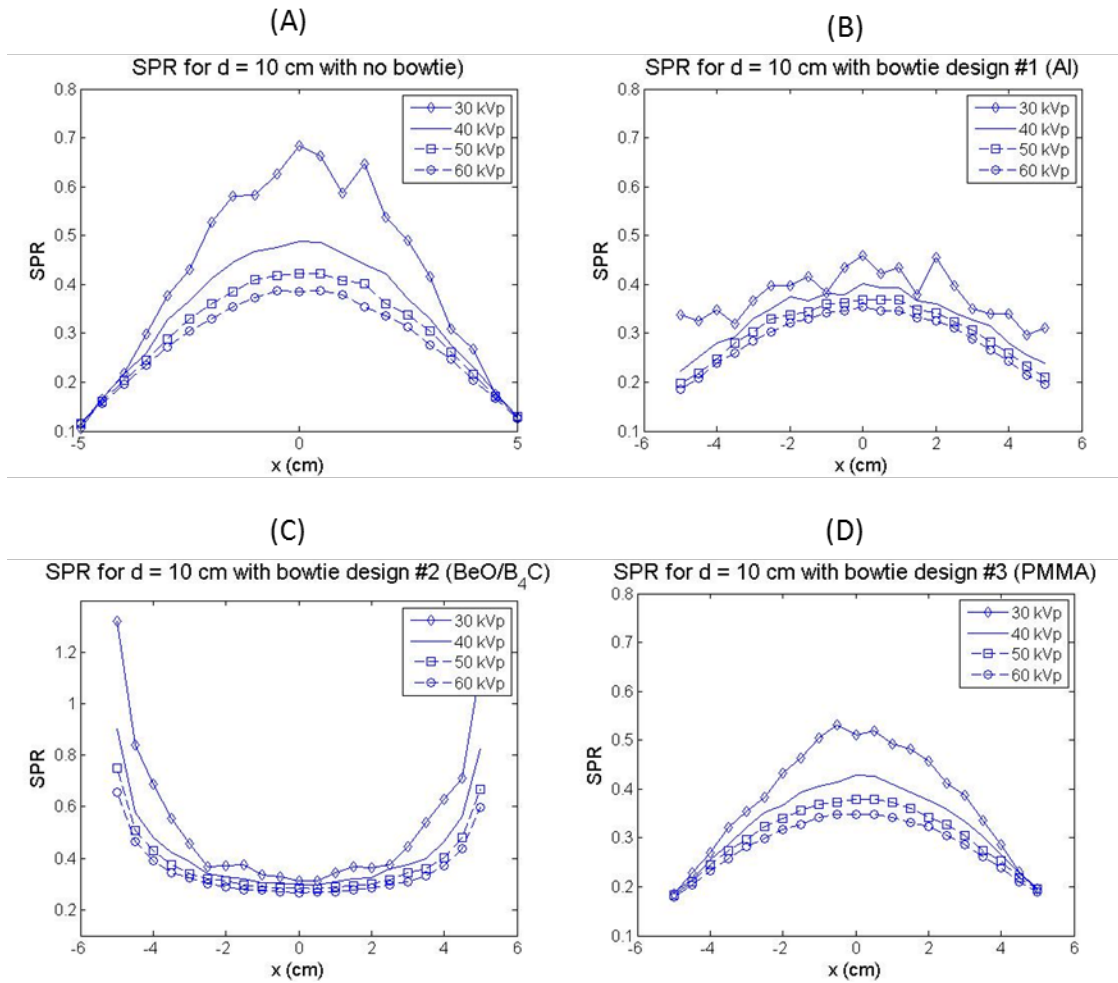
Figure 5.6: SPR calculations from simulated images for various tube voltages using
(A) no-bowtie filter, (B) bowtie design #1 (Al), (C) bowtie design #2 (BeO/B$_4$C),
and (D) bowtie design #3 (PMMA).

The experimental and simulation results both show that for higher tube

voltages, the SPR does not drastically change. However, as the tube voltage

decreases, the SPR tends to increase. This same trend was seen in the experimental

and simulation work characterizing the scatter in dedicated breast CT by Chen *et*

al.[80] With the use of the bowtie filters, the SPR can be decreased even with the

lower tube voltages. Figure 5.7 shows percent decrease from the SPR value at the

center of the phantom (x = 0) with no bowtie filter to the center SPR value (at x = 0) with the three different bowtie filters from the simulation data. The greatest reduction in the SPR value was obtained at the lower tube voltages. The center SPR value was reduced the most with the use of bowtie design #2 (BeO/B$_4$C) for all tube voltages.
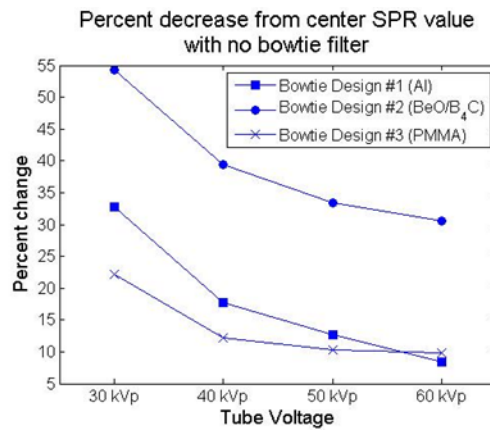
Figure 5.7: Calculated percent change from center SPR value (at x = 0) with no-bowtie filter and center SPR value with bowtie filter for various tube voltages.

5.3.2 SPR dependency on breast diameter

The bowtie filters are designed for a specific breast diameter. From initial computational results analyzing the robustness of the bowtie filter designs, breast diameter did not change the desired result greatly. The following plots show how the SPR is affected by varying breast diameters with the use of the three bowtie filters.

Figure 5.8 shows the SPR calculated through experimental images and simulation images for all bowtie designs and for three different breast diameters at

50 kVp. There is no physical prototype of bowtie design #2 (BeO/B4C) so only simulation data are available. The experimental and simulation data match for the larger diameter breast phantoms, but deviate slightly for the 10 cm phantom. For each breast diameter, the use of the bowtie filter decreases the SPR value at the center, and also flattens the SPR value in the x-direction direction.

Bowtie designs #1 (Al) and #3 (PMMA) both exhibit similar behavior for all three breast diameters. According to the simulation data, the overall magnitude of the scatter (maximum in the SPR curve) is decreased for each breast diameter by an average of approximately 18% by these two bowtie filter designs.
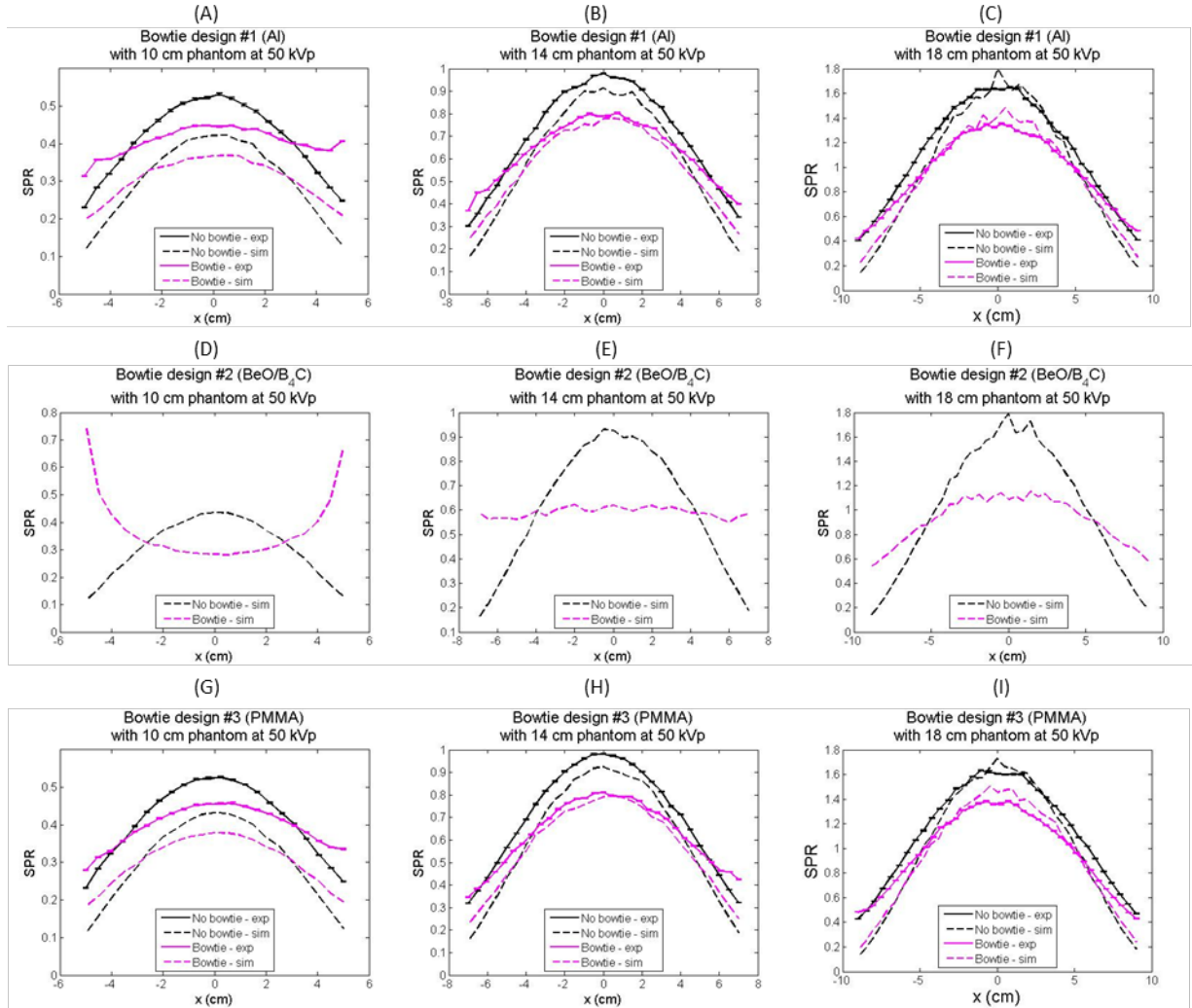
Figure 5.8: SPR value for various diameter phantoms using (A-C) bowtie design #1 (Al), (D-F) bowtie design # 2 (BeO/B$_4$C) and (G-I) bowtie design #3 (PMMA). Both experimental and simulation values of SPR are shown at a tube voltage of 50 kVp.

The largest reduction in SPR of approximately 35% comes from using bowtie design #2 (BeO/B$_4$C). For this bowtie design, the SPR as a function of distance across the detector is nearly flat for the 14-cm phantom. With the 10-cm phantom, bowtie design #2 produces cupping in the SPR compared to the 14-cm plot: the lowest value is located in the center while the edges of the phantom exhibit large SPR values. A similar result was found by Kwan *et al.* in their characterization of

scatter properties in dedicated breast CT.[29] The bowtie filter used in the Kwan study was made of Teflon (C_2F_4) and designed for a 14-cm cylindrical phantom made of 50% fibroglandular/50% adipose composition at 80 kVp. Their results show the SPR at the center of the 10-cm phantom to be approximately 0.23, increasing to a value of approximately 0.6 at the periphery. The results in the present study show an SPR value of 0.28 at the center of the 10-cm phantom and approximately 0.7 at the periphery. With the larger breast diameter, bowtie design #2 causes capping in the SPR compared to the 14-cm plot. Again, this same result is seen in Kwan *et al*.

Lück *et al*. recently reported on the effects of bowtie filtration on image quality and dose in dedicated breast CT.[30] This simulation study included the characterization of scatter with bowtie filters for different breast diameters. Figure 5.9 shows the center SPR value for each breast diameter and bowtie filter in the present study as well as the values obtained by Lück *et al*. The central SPR values are in fairly good agreement. The same general trend is seen with the central SPR values calculated using the three bowtie filter designs in this study compared to the bowtie design from Lück *et al*. A direct comparison is difficult to do, however, since the design goals and bowtie filter materials differ between the two studies.
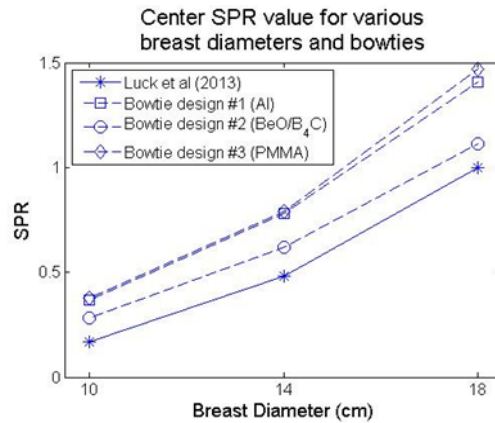
Figure 5.9: Comparison of central SPR values obtained in the present study and those values obtained from Lück *et al* (2013). The central SPR value for the simulation data were plotted for each bowtie filter type and breast diameter.

5.3.3 Scatter distribution

Using the ratio given by Eq. 5.2, the effect of the bowtie filter on the distribution of scatter was analyzed. Each bowtie filter contains a constant thickness base of 0.35 cm of the bowtie material(s). This base thickness was included in the no-bowtie configurations, so the no-bowtie filter case for the scatter distribution was different for each bowtie filter. Figures 5.10-5.12 show the scatter distribution for 10 cm, 14 cm, and 18 cm diameter phantoms at 50 kVp. The left column shows the no-bowtie filter case with the added thickness base of each bowtie filter material. The right column shows the scatter distribution with the bowtie filter. For each phantom diameter, the images are on the same scale so that the difference between the bowtie/no-bowtie distributions can easily be seen, and a comparison between the distributions for each bowtie filter can be made.
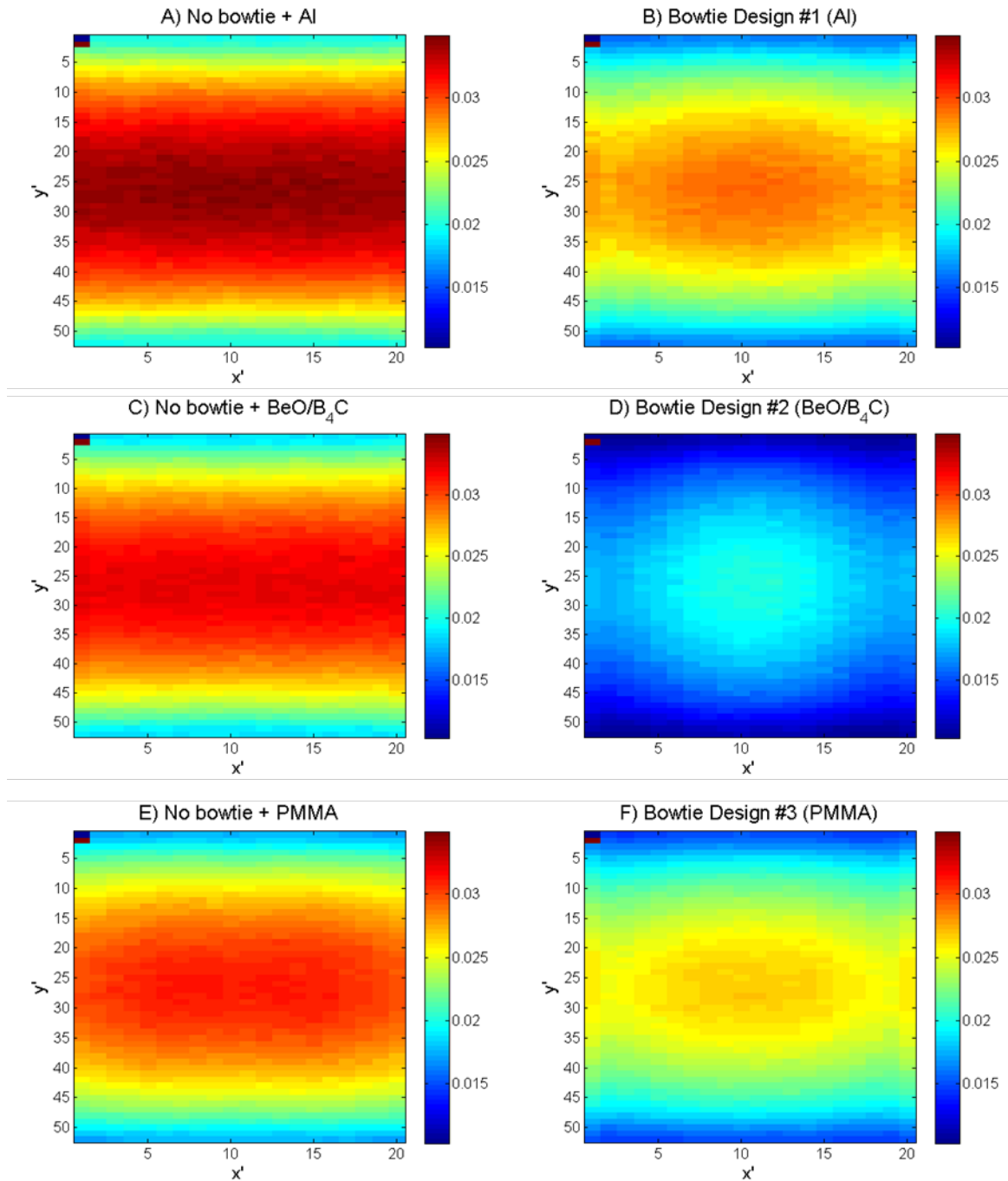
Figure 5.10: Scatter distribution using the SOCR metric for the three bowtie filter types using a 10 cm diameter breast phantom and a tube voltage of 50 kVp. A, C, E show the scatter distributions with no-bowtie filter, but include the constant thickness base from the bowtie filter so that a valid comparison between the two cases can be made. The variables x' and y' represent the bin number of the re-binned scatter image used to compute the SOCR.
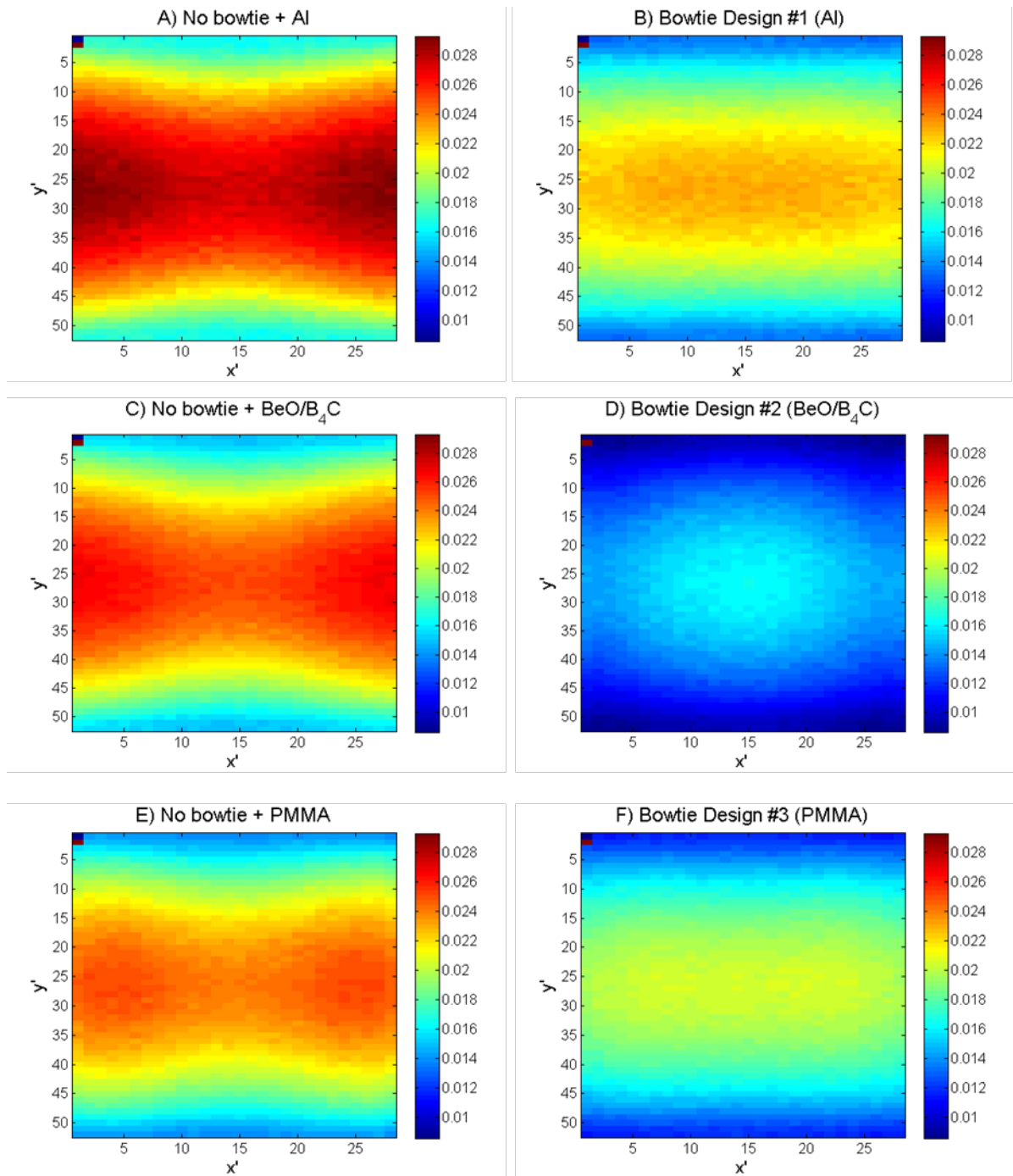
Figure 5.11: Scatter distribution using the SOCR metric for the three bowtie filter types using a 14 cm diameter breast phantom and a tube voltage of 50 kVp. A, C, E show the scatter distributions with no-bowtie filter, but include the constant thickness base from the bowtie filter so that a valid comparison between the two cases can be made. The variables x' and y' represent the bin number of the re-binned scatter image used to compute the SOCR.
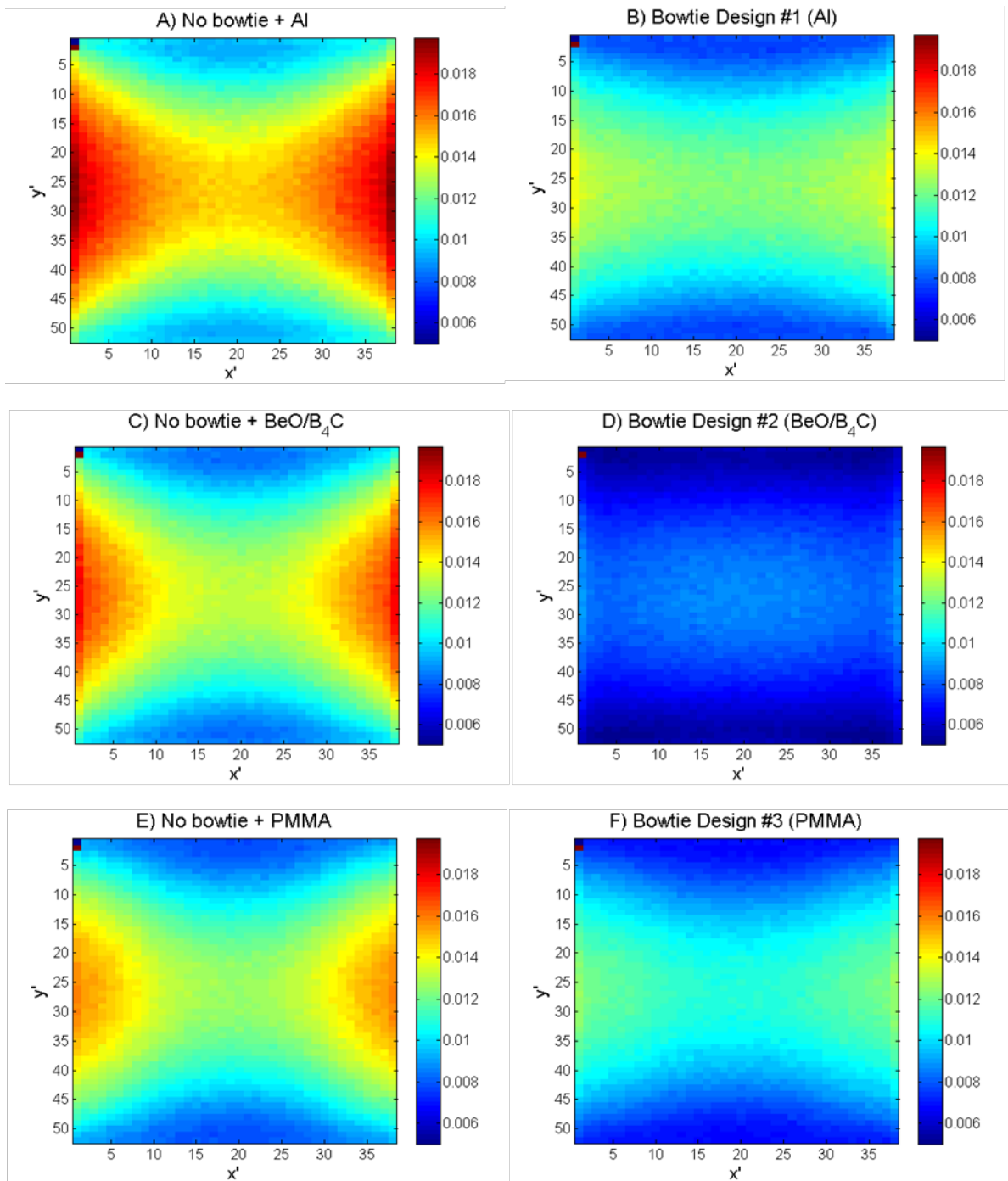
Figure 5.12: Scatter distribution using the SOCR metric for the three bowtie filter types using a 18 cm diameter breast phantom and a tube voltage of 50 kVp. A, C, E show the scatter distributions with no-bowtie filter, but include the constant thickness base from the bowtie filter so that a valid comparison between the two cases can be made. The variables x' and y' represent the bin number of the re-binned scatter image used to compute the SOCR.

The scatter distributions are very similar for the no-bowtie filter cases for a given breast diameter. With these plots, it is easy to see the reduction in the magnitude of the scatter signal for all three bowtie types. The greatest reduction in the scatter magnitude can be seen using bowtie design #2, as was indicated with the SPR measurements. As the breast phantom diameter is increased, the structure in the scatter distribution plots also increases with the no-bowtie filter case. With the inclusion of the bowtie filters, It can be seen that the distributions of the scatter in the x- and y-directions are more uniform compared to the no-bowtie filter cases. While this result can be readily seen in the SPR measurement for bowtie design #2 (BeO/B4C), the increased uniformity in the scatter distribution with bowtie designs #1(Al) and #3 (PMMA) is more difficult to see using the SPR metric. With the SOCR metric, the decrease in the structure of the scatter signal easier to appreciate.

5.4 Discussion

Through experimental and computational methods, the scatter in dedicated breast CT with the use of three different bowtie filters has been characterized in terms of magnitude and distribution. These filter designs were evaluated to see how they affect the scatter with varying breast diameters and tube voltages. SPR values were obtained in the x-direction. Since the photons travel through the same filter thickness

at the center in the bowtie and no-bowtie filter cases, the SPR results obtained in the y-direction would be similar between the no-bowtie and bowtie filter cases.

For different tube voltages, the experimental and simulation data both showed an increase in the SPR value with decreasing tube voltage. A similar trend was reported in previous studies.[29, 80] A wide range of optimal tube voltages has been proposed for dedicated breast CT ranging from low values near 30 kVp to higher values around 80 kVp.[5, 13-15, 85] It would be advantageous to use a bowtie filter that reduces the scatter independent of the tube voltage, given this range. With the inclusion of a bowtie filter, the SPR was decreased for all tube voltages, but this decrease was not completely independent of tube voltage. There was also some variability in the amount of scatter reduction obtained using each bowtie filter at various tube voltages.

The difference seen between bowtie filters in the scatter reduction at different tube voltages (Figure 5.7) may be partly due to the amount of scatter generated by the bowtie filter itself. The ratio between the incoherent scatter cross section and the total linear attenuation coefficient for the four bowtie filter materials increases rapidly with increasing energy between 10 keV and 50 keV.[49] Since incoherent scatter contributes the most to the scatter contamination signal reaching the detector for these materials, this ratio would help to explain the decrease in scatter reduction seen with higher tube voltages for each bowtie filter design. Future studies could include analysis of the scatter contribution from each individual component in the CT scanner/simulation environment.[80, 88, 89]

The experimental and simulation SPR data for the three different bowtie filters with three different breast diameters matched well. Although there was an approximate -17% change between the experimental and simulation SPR values for the 10-cm breast phantom, the overall shape of the SPR curves matched reasonably well.

Bowtie filter design #2 (BeO/B_4C) showed the greatest reduction in the SPR for all breast diameters. The SPR as a function of horizontal distance was nearly flat for the 14-cm diameter phantom using this bowtie design. Since this bowtie is designed to attenuate x-rays the same way that 40% glandular/60% adipose breast tissue does, it would seem as if the x-rays all traveled the same path length to get to the detector at all fan angles.

The variation in bowtie filter performance for different breast diameters for bowtie designs #1 (Al) and #3 (PMMA) is very small compared to the variation in bowtie filter performance with bowtie design #2 (BeO/B_4C). The SPR is reduced using bowtie designs #1 and #3 for all breast diameters, and the general shape of the SPR curve remains the same. Although the center SPR value is reduced for all three breast diameters using bowtie design #2 (BeO/B_4C), the shape of the SPR curve changes with the breast diameter. At smaller breast diameters, the SPR curve is higher at the periphery of the phantom and lower at the center.   The bowtie filters are designed by taking into account the change in the path length of a photon through a cylindrical phantom as a function of fan-angle. The bowtie filter thickness is minimum at the center, and the same for the bowtie and no-bowtie filter cases so the effect of the bowtie filter is not applicable. Moving toward the periphery, however,

the variation of the bowtie filter is meant to account for the 14-cm phantom, and not

the 10-cm phantom. Figure 5.13 shows the shape of the bowtie filter if it were

specifically designed for the 10-cm phantom.
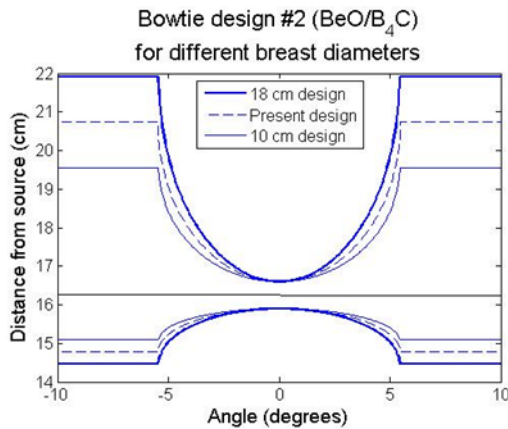
Figure 5.13: Comparison of bowtie designs for the 10-cm diameter and 18-cm diameter phantoms with the design used in the present study (14-cm diameter phantom). The shape of the two-material bowtie filter designed specifically for the 10-cm phantom is shown as the thin solid line while the specific design for the 18-cm phantom is shown as the thick solid line. The 14-cm phantom design used in the present study is shown as a dotted line.

The difference in the thickness of the filter can be easily seen. This means

that when imaging a 10-cm phantom with the bowtie filter that was designed for a 14-

cm phantom, the photons are being attenuated too much. This results in fewer

primary photons hitting the detector at the larger fan-angles, which drives the SPR

value higher and higher. The opposite is seen for the 18-cm phantom. The bowtie

filter #2 design used in the study is undercompensating for the path length through the

18-cm diameter phantom which results in more primary photons hitting the detector

at larger fan-angles. This explains the decrease in SPR toward the periphery of the

phantom with the larger breast diameter.

The last analysis done on the simulation images looked at the spatial distribution of the scatter signal with the three different bowtie filters for three different diameter phantoms and 50 kVp spectrum. These results reveal more information about the distribution of the scatter signal than the SPR since the SPR values can be overshadowed by the large variation in the primary signal. As indicated by the plots in Figures 5.10-5.12, the bowtie filters reduce the magnitude of the scatter and the spatial variation in the scatter distribution. The benefit of a bowtie filter in reducing the scatter structure is more evident with larger phantoms. Bowtie design #2 (BeO/B$_4$C) achieves the highest degree of uniformity in the scatter signal distribution. The ability of these bowtie filter designs to produce a more uniform scatter signal distribution could be beneficial when applying scatter correction algorithms that use primary modulation to separate the primary and scatter signals in the frequency domain. [90, 91] This feature could also increase the computational efficiency in Monte Carlo based scatter corrections that rely on fitting functions to reduce the number of photons required to estimate the scatter.[92, 93]

Chapter 6: Experimental validation and evaluation of bowtie filter designs

6.1 Introduction

Bowtie filters are designed to compensate for the variable path length of a patient across the object FOV.[16] These types of filters are commonly used and widely applied in body and head CT scans[18, 19, 94, 95], and are becoming an important inclusion for dedicated breast CT scanning.[29, 30, 65, 85] There are several benefits to bowtie filter implementation. One benefit is the ability to reduce the dynamic range requirement on the detector by delivering a more uniform fluence to the peripheral detector elements.[95-97] Other well-known benefits include the reduction of scattered radiation[74, 75, 93] and the reduction of dose to the patient.[18, 61, 62]

Several groups have designed bowtie filters for body and head CT applications with various design objectives.[23-26, 95, 98] The idea of a dynamic bowtie filter using different wedge designs was presented by a couple of researchers as well. These studies looked at bowtie filter designs optimized to reduce the dynamic range requirement on the detector for abdomen, shoulder, thorax, and head imaging,[24] or general matching of the patient attenuation characteristics[25, 26] as a function of view angle. The regions that were tested generally have an elliptical shape that changes as the source and detector rotate around the patient. For example, in an abdominal CT scan, the projection image of the abdomen taken from the front of the patient will

generally be much different from the projection image taken at the side of the patient since humans are generally thicker in the coronal plane compared to the sagittal plane. Other groups have designed stationary bowtie filters for helical CT scanning of the thorax designed for dose reduction[98] and for cone-beam CT of the head designed for uniform flux intensity in the projection.[95]

While these studies have shown the clinical feasibility and advantages of bowtie filter implementation in body and head CT scans, the fact still remains that these regions of the body contain different materials that vary greatly in their attenuation characteristics (i.e. bone). The ideal bowtie filter would be able to simulate all the tissues in the region-of-interest (ROI), but this is not possible in these body regions. The breast, however, is more homogenous in composition compared to other regions of the body and is relatively symmetric in the coronal and sagittal planes, making dedicated breast CT an ideal candidate for bowtie filter implementation.

Since the initial studies validating the usefulness of dedicated breast CT,[5, 6, 8, 14, 99] there have been a few different bowtie filter designs for this imaging modality that all vary in their design objective. Boone *et al.* designed a bowtie filter made of Teflon (C_2F_4) that delivered ideal beam flattening for 50% fibroglandular/50% adipose breast tissue for 50 keV photons. [44] Silkwood *et al.* investigated the effect of bowtie filtration on CT number, noise and CNR using a simulated bowtie filter composed of uniform breast tissue.[12] Most recently, Lück *et al.* designed two different bowtie filters: one aimed at delivering uniform dose to a cylindrical phantom used in the study, and another aimed at achieving uniform noise distributions in the

reconstructed images.[30] All of these studies showed that the use of a bowtie filter

improves image quality and reduces the dose to the patient.

The bowtie filter designs used in this experimental study differ from those

reported in the literature. By using the ideas of spectral matching and basis material

decomposition, three different bowtie filters were designed that better represent the

object being imaged (i.e. breast) and allow the user to have more control of certain

design parameters. These designs have been previously validated through

computational and simulation methods.[65, 66]

6.2 Methods

6.2.1 Bench top cone-beam CT system

The experimental, bench top CBCT[84] system simulates the geometry and

acquisition procedure of a cone-beam breast CT system. The x-ray tube is a Varian

G1582BI tube with a 10° rotating tungsten anode and 0.3/0.6 mm focal spots. The

detector is a Varian Paxscan 4030CB that uses a CsI scintillator with 1536 x 2048

pixels and a 0.194 mm pixel pitch. No binning was used when images were acquired.

With the use of a collimator, the FOV was approximately 300 mm x 250 mm to

accommodate the large breast phantom. The tube output for each breast diameter was

chosen such that the same average pixel value in a central ROI was obtained.

Instead of rotating the source and detector around the phantom, the phantom

was placed on a rotary table with three linear stages (Velmex , location) to position

the phantom anywhere between the source and detector. For these experiments, the

source-to-object distance (SOD) and source-to-detector distance (SDD) were 735 mm

and 985 mm, respectively.

6.2.1.1 Heel effect compensation

The heel effect arises from the attenuation of photons in the anode material

itself. This causes an uneven intensity and HVL distribution from the anode side of

the x-ray tube toward the cathode side. By increasing the SDD, the prominence of

the heel effect can be reduced.[96] This solution, however, is not achievable in current

dedicated breast CT systems. For our validation and evaluation of the presented

bowtie filter designs, it is important that the empty x-ray field is uniform. For that

reason, a wedge filter made of Teflon was fabricated to generate the desired uniform

field.

Using a Radcal 10x5-0.6 cc ion chamber and AccuGold radiation monitoring

system (Radcal, Monrovia, CA), air kerma and HVL measurements were acquired

across the detector FOV at a distance approximately equal to 0.9*SDD from the x-ray

source. The air kerma measurements were acquired for three different tube voltages:

40 kVp, 50 kVp, and 60 kVp. The wedge filter was designed for the 50 kVp data. A

50 kVp spectrum from IPEM Report 78 spectra was filtered with the tube's inherent

(0.8 mm Be + 2 mm Al) filtration and a Matlab program was written to determine the

thickness of Teflon required to obtain the same air kerma value as the experimentally

measured air kerma value of the furthest position toward the anode (the lowest value

in the field).

The dimensions of the wedge filter for the 50 kVp measurements were used to

fabricate a physical filter. The wedge filter was taped on the inside of the collimator,

and air kerma and HVL measurements at the same positions using the same

measurement tools were acquired for all three tube voltages. The results were plotted

to verify the reduction in intensity variation as a function of position and tube voltage,

and also to determine the reduction in HVL variability.

6.2.2 Bowtie filters

Three different bowtie filters have been designed and computationally

validated.[66] Two of the three bowtie filters (bowtie design #1 and bowtie design #3)

were designed and fabricated from aluminum and PMMA, respectively. Briefly,

bowtie design #1 (Al) was designed so that, in combination with a 14-cm diameter,

40% fibroglandular/60% adipose composition breast phantom positioned 735 mm

from the source, a constant spectral shape across the FOV would be transmitted. The

HVL was used as the metric to determine the validity of the design in the

computational analyses and was also used to experimentally verify the design.

Bowtie design #3 (PMMA) was designed to produce the same effective attenuation

coefficient at the detector behind the phantom FOV. This design would not require

the use of additional software corrections to the flat-field image. Line profiles

through scatter-free simulated images were obtained to validate the design. For both

bowtie designs, the energy fluence was expected to be dependent on the position

behind the phantom. Figure 6.1 shows an image of each bowtie design used

experimentally.
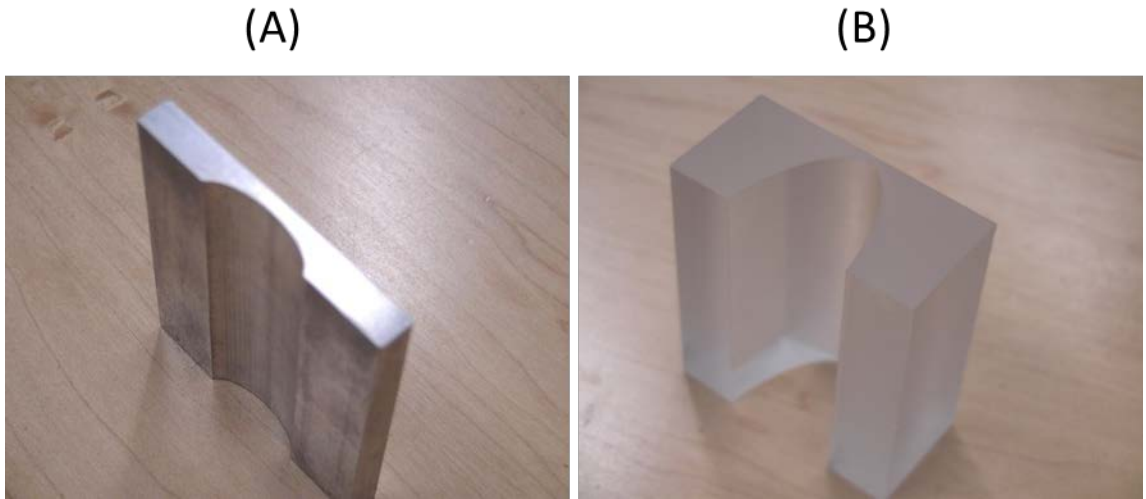
Figure 6.1: Images of the two bowtie filters validated computationally and manufactured for experimental validation and evaluation. The image is (A) shows bowtie design #1 made of aluminum and (B) shows bowtie design #3 made of PMMA.

6.2.3 Phantoms

Three hollow cylindrical phantoms made of PMMA with diameters of 10 cm, 14 cm, and 18cm were used. Each phantom was approximately 24 cm in length. A row of lead beads were placed on the top and bottom of the 14 cm phantom for geometric calibration purposes. Some details of the phantoms and inserts used in this study can be found in Keely *et al*.[82] The cylinders were filled with liquid mixtures of water, isopropyl alcohol, and glycerin in appropriate proportions such that the liquid simulated the x-ray characteristics of various breast compositions.[20, 21, 83]

6.2.3.1 CNR analysis

To perform CNR analyses, an insert was placed inside the hollow phantom with three 19 x 19 x 19 mm^3 blocks simulating 100% glandular tissue spanning from

the center of the phantom to the periphery (Figure 6.2). The phantom was then filled

with a liquid simulating the x-ray characteristics of a breast with a composition of

40% fibroglandular/60% adipose.

Figure 6.2: Cylindrical 14-cm diameter phantom with CNR insert.[82] The phantom
contains three 100% glandular equivalent blocks from the center to the periphery to
calculate the CNR homogeneity.

6.2.3.2 Dose distribution analysis

The 14-cm diameter phantom was also fitted with a removable cap with two

hollow PMMA cylinders in the center and at the periphery that allow an ion chamber

to be placed in the center while images are being acquired (Figure 6.3). A separate

set of images were acquired with this cap for the no-bowtie filter cases and bowtie

filter cases to assess the air kerma values from the center to the periphery. The

Radcal Accu-Pro radiation monitor system was used with the 10x5-0.6 ion chamber

(Radcal Corp. Monrovia, CA). Since only the effect of the bowtie filters on dose

distribution from center to periphery is of interest, the air kerma values at the center

and periphery are used as a surrogate to dose in the tissue.

Figure 6.3: Cylindrical phantom with hollow PMMA inserts used for the dose distribution analysis. The Radcal 10x5-0.6 ion chamber is seen here in the peripheral cylinder.

6.2.4 Radiation field mapping

To validate the bowtie designs experimentally, a solid state multi-sensor was used in conjunction with the Radcal Accu-Gold Digitizer (Radcal Corporation, Monrovia, CA). The sensor was able to collect measurements of HVL and intensity simultaneously as it was moved behind the phantom across the FOV on a linear stage. The multi-sensor is typically used for quality assurance measures and was used only to characterize the radiation field behind the phantom with and without the bowtie filters.

Accurate measurements of the HVL were not necessary to validate the design, but experiments were done to test the accuracy and reproducibility of the Accu-Gold

multi-sensor. HVL and intensity measurements were obtained for arbitrary added filtration thicknesses of aluminum using the Accu-Gold multi-sensor and the Radcal 10X5-6 general purpose ion chamber. The results showed good agreement between the HVL as measured by the multi-sensor and the HVL measured using the ion chamber.

Because of tube output limitations, the Accu-Gold multi-sensor was not able to produce reliable results with the 18-cm diameter breast phantom across the entire object FOV. Therefore, the HVL was measured by placing the 10x5-6 ion chamber (Radcal Corporation, Monrovia, CA) on the linear stage instead of the multi-sensor. The ion chamber was moved to seven different positions behind the object to acquire measurements across the entire object FOV. Different thicknesses of aluminum were added to the x-ray beam in order to reduce the measured intensity to half of its initial value. The ion chamber positions corresponded to the sensor positions that were used for the 10 and 14 cm phantoms.

Although the bowtie filters were designed for a 14 cm diameter cylindrical breast phantom of 40/60 composition at 50 kVp, measurements were obtained for several different cases to test the robustness of the designs against changes in tube voltage, breast composition, and breast diameter. For each bowtie design, the following cases were realized: variable tube voltage from 40 – 60 kVp in 10 kVp increments while breast diameter (14 cm) and composition (40/60) were held constant; variable breast diameter from 10 – 18 cm in 4 cm increments while tube voltage (50 kVp) and breast composition (40/60) were held constant; and variable breast composition of 25/75, 40/60, 75/25 while tube voltage (50 kVp) and breast

diameter (14 cm) were held constant. It is important to note that the same bowtie

filters were used in the investigation of variable breast diameter; the bowtie filters

were translated along the source-detector axis to obtain appropriate coverage of the

larger and smaller breast phantoms.

The HVL and intensity were sampled at approximately 25 different positions

behind the phantom, with three measurements being acquired at each position. The

sampling positions across the detector FOV were the same for each phantom

diameter, meaning as the breast phantom diameter increased, more measurements

were acquired from behind the phantom as opposed to measurements outside the

object FOV.   The entire object FOV was sampled for each breast diameter.

6.2.5 Image analysis

300 projection images were acquired over 360° using the uniform composition

phantoms and the CNR insert phantoms and reconstructed using a filtered

backprojection algorithm. [52, 53] The voxel size of the reconstructed images was 0.14 x

0.14 x 1 mm^3. For the 10-cm, 14-cm, and 18-cm diameter phantoms, the

reconstructed image sizes were 800 x 800, 1000 x 1000, and 1200 x 1200,

respectively. A scatter correction method proposed by Sechopoulos using a tungsten

plate with an array of small holes was used to obtain estimates of the primary-only

images, and then subtract the estimates from the projection image without the plate to

obtain an estimate of the scatter signal at the location of each small hole.[54] Further

details on this method are given below. These scatter-corrected images were used to

analyze the beam hardening artifact, noise uniformity, and CNR uniformity with and

without the bowtie filters.

6.2.5.1 Scatter correction method

In addition to the typical methods of reducing scatter (field size, air gap, bowtie filtration, anti-scatter grid), there are several scatter correction algorithms currently used in cone-beam CT.[100] There are several measurement-based methods that propose the use of beam-blockers to acquire the scatter signal[79, 101-104] while other methods utilize primary modulation as a means of separating the scatter signal from the primary signal in the frequency domain.[90, 91] Other methods suggest the use of fast Monte Carlo GPU simulations of scatter to be used for correction.[105] The method proposed by Sechopoulos is similar to an inverse beam-block method. This method was easy to implement, accurate, and clinically relevant as dose measurements indicate that there was less than a 0.5% increase in the total patient dose.[54]

The scatter correction method employed on our bench-top cone-beam CT system used a 330 mm x 280 mm x 2.54 mm tungsten plate with an array of over 1800 holes, each 0.35 mm in diameter and 6.7 mm apart (Figure 6.4). For each experimental technique, there were five image data sets acquired: (1) flat-field images, (2) dark-filed images, (3) phantom projection images, (4) phantom + scatter plate projection images, and (5) scatter plate projection images (with or without bowtie).
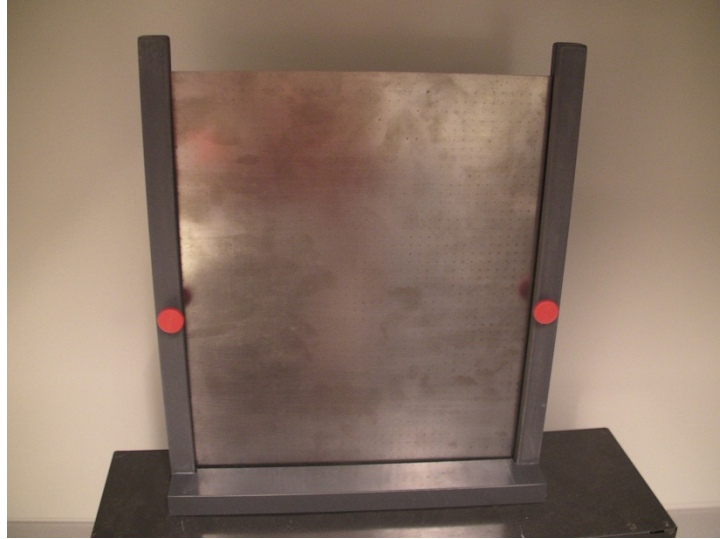
Figure 6.4 Tungsten plate used for scatter correction in experimental study

For the phantom + scatter plate projection images, the scatter plate was placed in front of the phantom in the path of the x-rays. The projection image of the phantom + scatter plate would consist of hundreds of pinhole projections through the phantom. These pin-hole projections were assumed to contain only the primary signal. The phantom + scatter plate projection images were flat-field and dark-field corrected. Using Matlab programming, the pixel location and intensity value of the maximum intensity pixel in each pin-hole projection for the phantom + scatter plate image was determined and saved. Before this estimate of the primary signal could be subtracted from the primary + scatter phantom projection images, an intensity correction factor was applied to each pin-hole location using the scatter plate only projection images.

Due to the unfocused nature of the small pin-holes on the tungsten plate, there was a reduction in the intensity in the pin-hole projection with the scatter plate compared to no scatter plate.[54] To account for this reduction in intensity in the

projection of the pin-hole for the phantom + scatter plate images, the flat-field image set and the scatter plate only image set was used. The same Matlab program was used to determine the location and intensity of the maximum intensity pixel in each pin-hole projection in the scatter plate only images. The pixel intensities at the same locations previously determined in the flat-field image were divided by those in the scatter plate only image. These pin-hole specific intensity correction factors were then multiplied by the pixel intensities for the corresponding locations in the phantom + scatter plate image. This methodology is an extension of Sechopoulos's work, as he did not take into account the intensity correction factor for each individual pin-hole projection.

After subtraction of the primary estimates multiplied by the intensity correction factors from the phantom images (primary + scatter), an estimate of the scatter at each pin-hole location was obtained. Using a radial basis function built-in to Matlab to interpolate between the points, an estimated scatter image was obtained for each phantom projection image (Figure 6.5). The work by Sechopoulous suggested using an inverse distance weighting function[106] for interpolation, but our results indicated that the radial basis function provided better interpolation. The scatter image was subtracted from the corresponding phantom projection image, and the result was used as an input to the reconstruction algorithm.
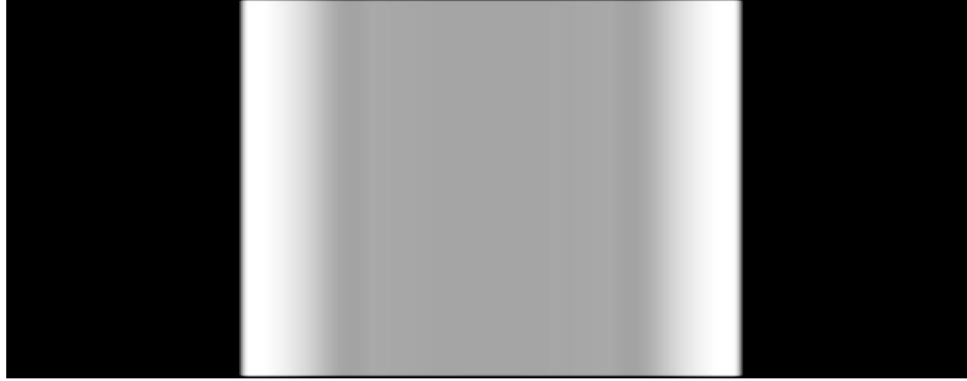
Figure 6.5: Interpolated estimation of the scatter image using the radial basis function in Matlab. This scatter estimate was for a 10 cm diameter phantom with bowtie design #1 (Al).

6.2.5.2 Beam hardening artifact

The resulting reconstructed images were smoothed with a Gaussian kernel. Line profiles using the central slice through the center of the phantom were plotted and normalized to the central pixel value for all bowtie filter cases and no-bowtie filter cases.

6.2.5.3 Noise uniformity

The noise uniformity was analyzed by selecting four volumes-of-interest (VOI) on the periphery of the reconstructed images and one central VOI. The standard deviation of each region in each slice of the reconstructed volume was obtained and applied to Eq. 6.1.[30, 55]

$$UI = \sum_{n=1}^{4} \left(\frac{\sigma_{n,periphery} - \sigma_{center}}{\sigma_{center}} \right) * \frac{1}{4} * 100 \qquad (6.1)$$

In this equation, $\sigma_{n,periphery}$ represents the standard deviation of the nth VOI, σ_{center} represents the standard deviation of the pixel values in the central VOI, and UI is the resulting uniformity index. This analysis was done only on the 14-cm phantom since the lead BB method used for geometric calibration of the bench-top CT scanner[107] was only applied to the 14-cm phantom.

6.2.5.4 CNR homogeneity

Images were acquired using the contrast insert phantom previously described and reconstructed. On each reconstructed slice, an ROI was selected in the glandular block and in a uniform area the same radial distance from the center of the phantom as the glandular block. For a given block (denoted by i), the CNR_i was computed on each slice by taking the difference between the average pixel value in the block ROI ($I_{block,i}$) and the average pixel value in the uniform ROI ($I_{noise,i}$), and dividing by the corresponding noise. The values were then averaged over all slices (N) in the reconstructed volume (Eq. 6.2).

$$CNR_i = \frac{\sum_{j=1}^{N} \frac{I_{block,i} - I_{noise,i}}{\sigma_{noise,i}}}{N} \tag{6.2}$$

6.3 Results

6.3.1 Heel effect reduction

A wedge filter was designed and fabricated to generate a uniform field in terms of intensity and HVL distribution as a function of position across the detector

FOV. Figure 6.6 shows plots of the normalized air kerma distribution as a function of position across the detector (anode side to cathode side of x-ray tube) for three different tube voltages.
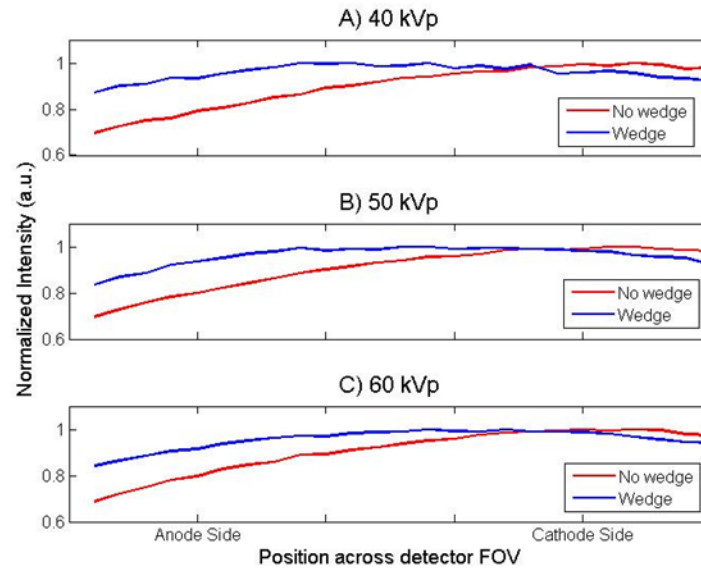
Figure 6.6: Air kerma measurements with and without a Teflon wedge filter to account for the heel effect. The values are normalized to the maximum intensity value. Measurements were acquired at (A) 40 kVp, (B) 50 kVp, and (C) 60 kVp.

For all tube voltages, the addition of the Teflon wedge filter reduced the variation in the measured air kerma from about 30% to less than 15%. The measured HVL also showed similar results, with the variation in HVL as a function of position varying by less than 3% of the furthest anode-side position. Based on these results, the Teflon wedge filter was integrated into the imaging system for all radiation field mapping and image acquisition protocols.

6.3.1 Radiation Field Mapping

Bowtie design #1 was designed with a specific design goal of equalizing the measured HVL in the object FOV and decreasing the variation in intensity from the center of the phantom to the periphery of the phantom. Computational results indicate that this design goal can be achieved, but experimental validation was needed. Although the design goal of bowtie design #3 was to produce a uniform effective attenuation coefficient at the detector, measurements of the HVL and intensity behind the object were taken and analyzed for the 14-cm, 40% fibroglandular/60% adipose phantom even though these results will not validate the design.

The HVL behind the object FOV was also measured for various parameters to determine the robustness of bowtie design #1 against variations in tube voltage, breast diameter and breast composition. Only measurements for bowtie design #1 (Al) were taken for this analysis.

6.3.1.1 Bowtie filter design validation

The following plots show the measured values behind the 14-cm diameter phantom using a spectrum of 50 kVp with and without bowtie design #1 (Al). Figure 6.7A shows the measured HVL as a function of position behind the phantom with and without the bowtie filter design #1. Figure 6.7B shows the measured intensity as a function of position behind the phantom with and without bowtie design #1 (Al). Both plots were normalized to the center value.
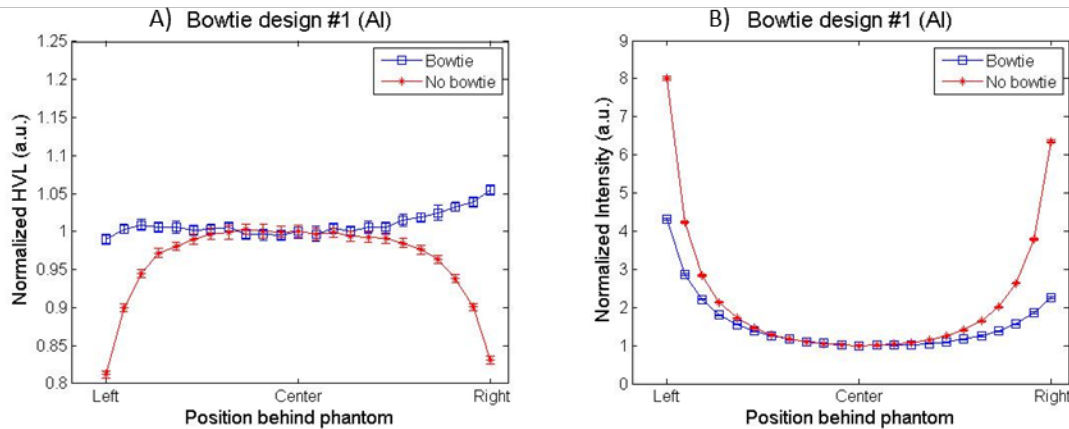
Figure 6.7: Measured values behind phantom FOV with and without bowtie design #1 (Al) normalized to the center value. (A) The measured HVL is plotted as a function of position behind the phantom with and without the bowtie filter. (B) The measured intensity as a function of position behind the phantom is plotted with and without the bowtie filter.

The data from these figures validate the design goal of bowtie design #1. The measured HVL is nearly constant in the object FOV with the use of bowtie design #1 (Al) while the HVL varies by approximately 20% from center to periphery with no bowtie filter. The decrease in the variation of the intensity is also seen with the use of bowtie design #1 (Figure 6.7B).

Figure 6.7 shows the measured HVL and intensity variation across the object FOV using bowtie design #3 (PMMA). Although these measurements will not validate the bowtie filter design, it is still important to note that the variation in HVL is slightly decreased with the use of the bowtie filter compared to the no bowtie filter case (Figure 6.8A). The same degree of variation in intensity from center to periphery can be seen using bowtie design #3 (PMMA) as with bowtie design #1 (Al) (Figure 6.8B).
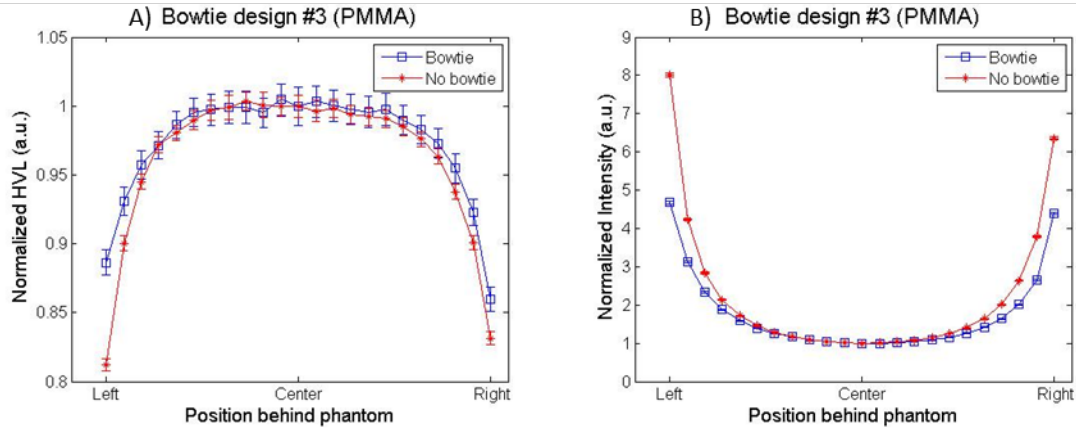
Figure 6.8: Measured values behind phantom FOV with and without bowtie design #2 (PMMA) normalized to the center value. (A) The measured HVL is plotted as a function of position behind the phantom with and without the bowtie filter. (B) The measured intensity as a function of position behind the phantom is plotted with and without the bowtie filter. These plots will not validate the design but are important features of the bowtie design.

6.3.1.2 Bowtie filter design evaluation

Figure 6.9 shows the measured HVL using the AccuGold system for bowtie design #1 (Al) with various breast compositions, breast diameters, and tube voltages. The HVL measurements were normalized to the measurement that was obtained at the left peripheral side of each phantom since we are interested in looking at how the HVL measurements vary as a function of position behind the phantom.

With the different breast compositions and breast phantom diameters, the measured HVL varied more compared to the variability with different tube voltages. Bowtie design #1 is meant to achieve its design goal of uniform HVL behind the phantom FOV independent of photon energy in the diagnostic range. The results in Figure 6.9C show that the bowtie filter achieves this goal. The error bars are very large with the measurements taken at 40 kVp due to the decreased photon fluence hitting the solid state detector. Even with this limitation, these results show that the

HVL measurements at different tube voltages behind the phantom FOV vary, at most, by approximately 7% from the peripheral measurement.

When using different breast compositions with bowtie design #1, there is more variability as the position behind the phantom changes (Figure 6.9A). With a breast composition with less fibroglandular percentage than the composition for which the bowtie filter is designed (i.e. 40% fibroglandular/60% adipose), the measured HVL decreases as the radiation sensor is moved toward the center of the phantom, and then increases again. The measured HVL does not change greatly with the 75% fibroglandular/25% adipose breast tissue mixture compared to the 40% fibroglandular/60% adipose mixture. For all different breast compositions investigated, the maximum variation from the peripheral measurement is about 4%.

The largest variation in the measured HVL at different positions behind the phantom occurs with different breast diameters shown in Figure 6.9B. Compared to the 14-cm diameter phantom measurements, the measurements for the 10-cm phantom decrease by 5% compared to the peripheral measurement as the radiation monitor is moved to the center of the phantom and then increase. The measurements behind the 18-cm phantom increase by approximately 8% compared to the peripheral measurement as the radiation monitor is moved toward the center, and then decrease.
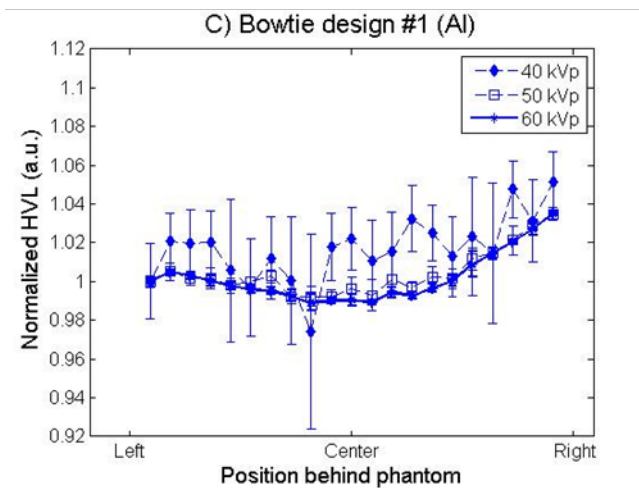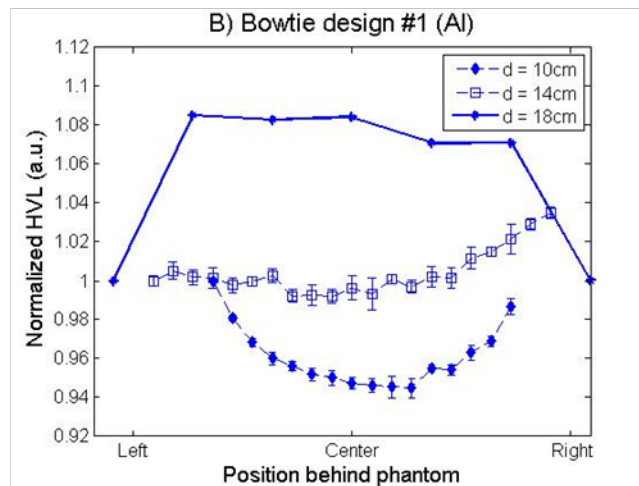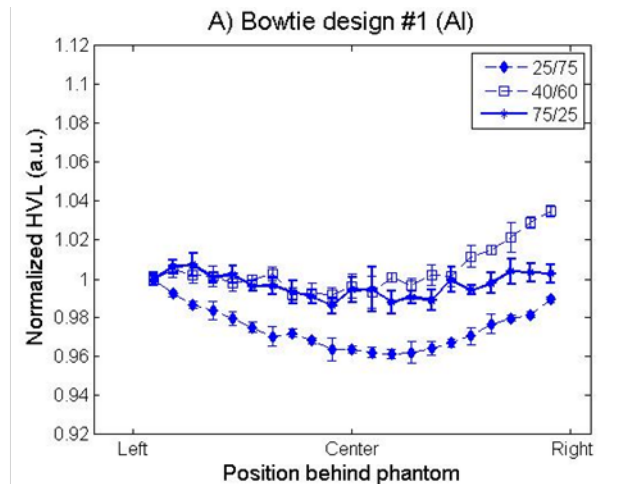
Figure 6.9: Normalized HVL measurements behind the phantom FOV for various parameters using bowtie design #1 (Al). The HVL was measured with various (A) breast compositions, (B) breast phantom diameters, and (C) tube voltages.

The intensity behind the phantom was also measured for different breast compositions, breast diameters, and tube voltages. For all different parameters, the intensity measured behind the phantom was decreased compared to the no-bowtie filter case for both bowtie design #1 (Al) and bowtie design #3 (PMMA). These results indicate that independent of the breast phantom characteristics and spectrum, the dynamic range can be reduced with the inclusion of the bowtie filters described in this study.

6.3.2 Beam hardening artifact

The bowtie filters were included in the imaging scheme during the collection of 300 projection images used for reconstruction. The line profile through the center of the phantom in the central slice of the reconstructed images were used to as an additional validation for bowtie design #1 (Al), and primary validation for bowtie design #3 (PMMA). Bowtie design #3 (PMMA) was designed so that the effective attenuation coefficient would be constant such that the line profile through the scatter-free reconstruction image would be flat.

Figure 6.10 shows the line profile of the uniform phantom filled with 40% fibroglandular/60% adipose equivalent tissue material with bowtie design #1 (Al), bowtie design #3 (PMMA), and with no bowtie. The line profiles are normalized to the central pixel value. For each no-bowtie filter case, additional filtration was added to account for the constant thickness base added on to each bowtie filter so that an accurate comparison could be made. In this study, the constant thickness base was

03.5 mm, so for the no-bowtie filter cases for bowtie design #1 and bowtie design #3, 3.5 mm of aluminum and PMMA were added, respectively.

The Figure 6.10C and 6.10D show the line profiles for the 14-cm phantom using both bowties. Since each bowtie filter was designed for a 14-cm cylindrical phantom, these plots validate the designs. Figure 6.10C shows that with bowtie design #1 (Al), there is a capping artifact due to the beam hardening in the calibration scan, as expected. Figure 6.10D shows that with the use of bowtie design #3 (PMMA), there is no such capping artifact and the line profile through the center of the phantom is constant compared to the no-bowtie filter case.

Bowtie design #3 (PMMA) is fairly robust against variation in the breast phantom diameter. For the 10-cm and 18-cm phantoms, the line profiles using this bowtie design remain fairly constant compared to the no-bowtie filter case. This result was expected based on computational and simulation studies previously reported.[66]
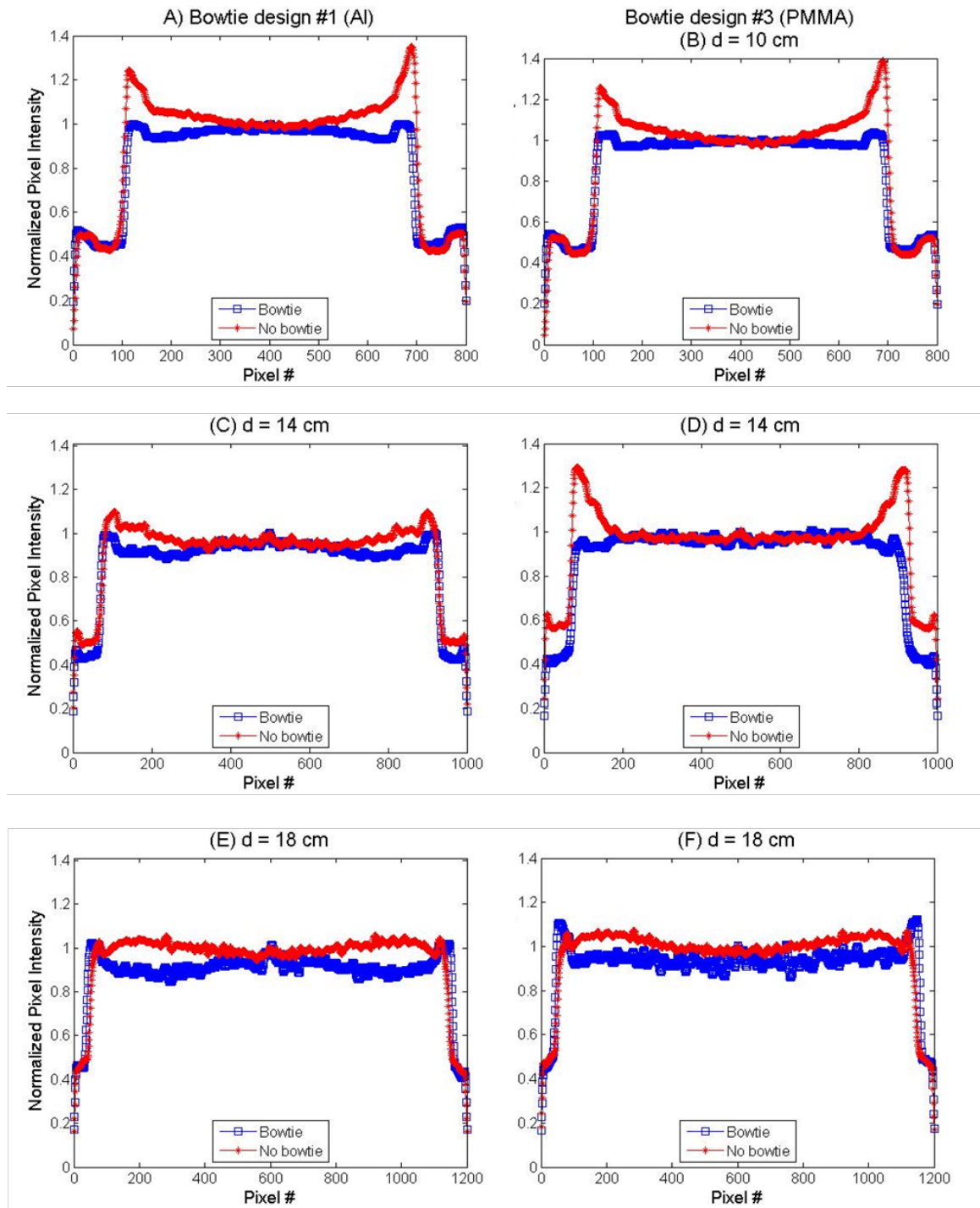
Figure 6.10: Line profiles of central slice of reconstructed images with and without bowtie design #1 (Al) and bowtie design #3 (PMMA). Plots A, C, E show the line profiles with and without bowtie design #1 (Al) for various phantom diameters. Plots B, D, F show the line profiles with and without bowtie design #3 (PMMA) for various phantom diameters.

6.3.3 Noise uniformity

The change in the noise distribution for the 14-cm diameter phantom was investigated by calculating the noise UI. The results for the no-bowtie filter cases and the bowtie filter cases are shown in Figure 6.11. Again, since the bowtie filters each contain a constant thickness base of 3.5 mm, the no-bowtie filter cases contain the 3.5 mm of the same bowtie filter material to allow for comparisons.

Non-uniformity in the noise without a bowtie filter arises from the variation in photon fluence that hits the detector. In the center, where the path length through the cylindrical object is greatest, the noise is increased due to a lower photon fluence. At the periphery, the path length is shorter and noise is decreased due to the increased photon fluence. The black line at UI = 0 in each plot in Figure 6.11 is included as a visual reference. This is the desired case: the closer the points are to this line, the better the noise uniformity. Without the bowtie filter, the noise varies from center to periphery, on average, by approximately 7% . The noise UI is improved with the inclusion of the bowtie filters such that the noise varies by less than 2% from center to periphery.
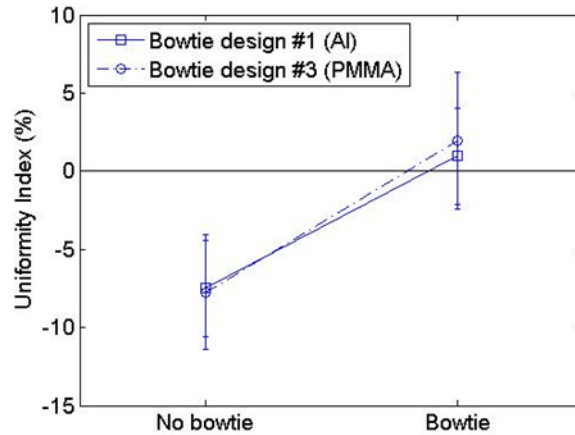
Figure 6.11: Noise uniformity index calculated using the 14-cm diameter phantom with and without bowtie design #1 (Al) and bowtie design #3 (PMMA).

6.3.4 CNR homogeneity

Using the contrast phantom described above, the CNR was calculated at three different locations within the 14-cm diameter phantom to understand how the CNR homogeneity is affected by the inclusion of a bowtie filter.   Figure 6.12 shows the results of the calculation.

With the inclusion of both types of bowtie filters, the CNR was more uniform compared to the no-bowtie filter case. Without the bowtie filter, the CNR increased by approximately 20% from the central measurement (Figure 6.12A). With bowtie design #1 (Al), the CNR only varied by 10%. With bowtie design #3, the CNR varied by less than 5% (Figure 6.12B).
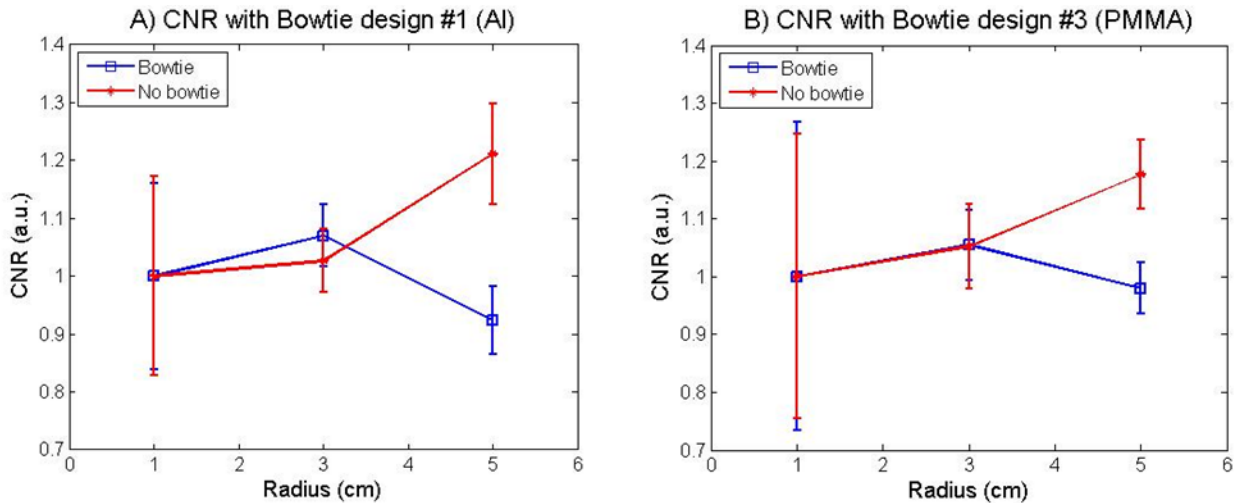
Figure 6.12: CNR calculations as a function of radial distance using (A) bowtie design #1 (Al) and (B) bowtie design #3 (PMMA). The results are normalized to the central CNR value.

6.3.5 Dose distribution

The dose distribution for each bowtie and no-bowtie filter case was measured using a CT ion chamber. Measurements were acquired in the center and at the periphery of the 14-cm diameter phantom using a 50 kVp tube voltage. The measurements were normalized to the values at the center in order to investigate the variation in the dose from center to periphery. The results with and without bowtie design #1 (Al) and bowtie design #3 (PMMA) are shown in Figure 6.13.
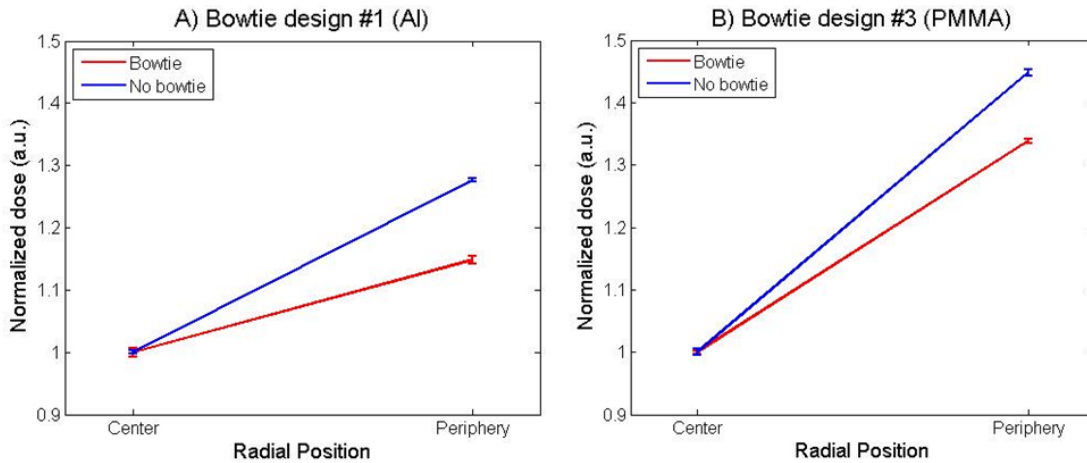
Figure 6.13: Experimentally measured dose distribution for the bowtie and no-bowtie filter case using (A) bowtie design #1 (Al) or 3.5 mm added Al filtration, and (B) bowtie design #3 (PMMA) or 3.5 mm added PMMA filtration.

With the inclusion of the bowtie filter, the dose distribution was less variable from the center to the periphery. Bowtie design #1 (Al) resulted in an approximate 20% reduction in the variation of the dose distribution compared to the no-bowtie filter case while bowtie design #3 resulted in a slightly smaller reduction of 15% compared to the no-bowtie filter case. Similar results were seen in the simulation analysis done using these two bowtie filters, with bowtie design #1 (Al) resulting in a 30% reduction in variation compared to the no-bowtie filter case and bowtie design #3 (PMMA) resulting in a 25% reduction.

6.4 Discussion

The measured values of HVL and intensity across the object FOV validated bowtie design #1 (Al). Similar measurements were obtained and plotted for bowtie design #2 (PMMA), even though these data would not validate the bowtie design. Looking at the intensity variation from center to periphery, both bowtie designs show

a decrease in intensity variation compared to the no bowtie filter case. The intensity as measured by an ion chamber can serve as a measure in calculating the dynamic range. With the dynamic range being defined as the ratio of the largest energy fluence to the smallest energy fluence, Figures 6.7B and 6.8B show that there is a decrease in the dynamic range requirement on the detector with the use of these bowtie filters. Low dynamic range is desired when implementing CT systems with photon counting detectors.[12, 108-110]

All of the bowtie filters are designed for a specific breast composition, breast diameter, and tube voltage. It is important to see how the design goals change when different parameters are used. The results in Figures 6.7 - 6.9 show the radiation field mapping with various breast compositions, breast diameters, and tube voltages to validate and evaluate the design goal of bowtie design #1. This bowtie design is meant to yield a constant HVL measurement independent of position behind the phantom. Figure 6.7A shows that this bowtie filter does achieve this design goal, but when different breast phantom diameters are used with the same bowtie filter design #1 that was designed for a 14-cm phantom, the results vary. Figure 6.9B shows that with larger breast phantoms, the measured HVL will increase from the periphery toward the center of the phantom rather than remain constant as indicated with the 14-cm phantom. Since the bowtie filter is designed for a 14-cm phantom, increasing the breast phantom size increases the amount of tissue that the x-rays need to travel through. This causes the x-ray beam to harden, and the HVL to increase. The same concept can be used to explain why the measured HVL decreases toward the center

for the 10-cm phantom. There is less tissue for the x-rays to travel through, so the x-ray beam does not get hardened as much as it would for a 14-cm phantom.

Both types of bowtie filters gave more homogeneous CNR calculations as a function of radial distance. These results are consistent with previously reported simulation and experimental experiments with different types of bowtie filters.[12, 30] This improvement is most likely due to the more uniform noise distribution that is obtained when the bowtie filters are used. Since there are fewer photons reaching the periphery of the breast with the bowtie filter in place, the CNR decreases. The error bars in the center-most ROI used for the CNR calculation are very large compared to the other ROIs. After further examination of the reconstructed volume, there are ring artifacts that appear in the central contrast ROI that may be causing the large variations in CNR calculation.

Although the CNR metric is important in determining the distinguishability between two different tissues, it is an object-independent metric and does not give as much information about the detectability of an object. The signal-to-noise ratio (SNR) is a task-based metric that takes into account the size, shape, and contrast of an object, as well as background in the image.[96] As shown by Brunner *et al.[111]*, the line spread function (LSF) will change as a function of contrast material, which will change the transfer function of the object used in the spatial definition of the SNR.[112] The CNR metric does not capture all of this information. The point spread function (PSF) is also location dependent, and will affect the detectability of objects. Therefore, future studies should investigate the location-dependent PSF and SNR

with and without the bowtie filters to get a better understanding of how bowtie filters change the detectability of objects.

The results of the noise UI calculations indicate that the inclusion of either bowtie design #1 (Al) or bowtie design #3 (PMMA) causes a reduction in the variation of the noise from the center to the periphery. Bowtie design #3 (PMMA) had a slightly worse noise UI compared to the noise UI for bowtie design #1 (Al), but these results are not surprising. Figures 6.7B and 6.8B show the measured intensity as a function of position behind the 14-cm diameter phantom for both bowtie types. While both bowtie filters decrease the variation in intensity behind the phantom FOV, bowtie design #1 (Al) generates a slightly more uniform distribution. This translates to a slightly lower fluence hitting the periphery of the phantom with bowtie design #1, which causes an increase in the noise to a level closer to that at the center of the phantom.

The noise UI is also dependent upon the material chosen for a given bowtie filter design. We have conducted a computational and simulation study to analyze the noise UI and other parameters with various materials for all of the bowtie filter designs proposed by our group.[66] However, we have yet to conduct an experimental validation of the study so future work would include an experimental analysis of different filter materials.

Since the lead BBs used in the geometric calibration method were only present on the 14-cm phantom, only the images of that phantom were analyzed for noise uniformity and distribution given that previous studies have shown that lack of geometric calibration can lead to noise variations that decrease the SNR.[113-115] The

line profiles that were obtained from the 10-cm and 18-cm diameter phantoms should not be affected by the lack of geometric calibration. Aside from the slight blurring artifact that was present at the edges of the phantom in the reconstructed images, there were no noticeable changes. Future studies would implement the geometric calibration method for all phantom sizes so that noise analyses could be done.

The bowtie filters investigated in this study only account for changes in the path length through a cylindrical phantom in the fan direction. Future work will focus on the design and manufacturing of anthropomorphic bowtie filters that take into account the change in the cross-sectional diameter of the breast as a function of z-direction. Lück *et al*. suggested dynamic modification of a bowtie filter with the spiral breast CT system used in the group.[30, 99] There are several other breast CT prototypes currently undergoing clinical trials and/or feasibility studies that employ a flat panel cone-beam geometry[10, 48, 60, 64], therefore, a bowtie filter that is able to achieve the desired design goals independent of the cross-sectional diameter for a projection image would be desirable.

Chapter 7: Computational and simulation framework for optimal spectrum analysis with bowtie filtration in dedicated breast CT

7.1 Introduction

Given that dedicated breast CT is a new imaging modality, researchers have yet to converge on the parameters for optimal usage. Although there are several parameters to optimize with a new modality, most groups have focused on the spectral optimization over the last several years.[5, 9, 13-15] The most common FOM used to determine the optimal spectrum takes into account one aspect of image quality (CNR) and the dose. This FOM, called the dose efficiency (DE), is defined as the ratio of the square of the CNR to the dose in a specific region. Several groups have used this FOM to determine the spectrum that yields the best image quality for the lowest patient dose. Weigel *et al.* determined a tube voltage between 50 – 60 kVp, with added aluminum filtration, would be a sufficient compromise between dose penalties and tube requirements[13] These results were obtained using a uniform cylindrical phantom with a centrally located insert composed of either iodine or calcium hydroxyapatite material. Prionas *et al.* investigated optimal tube voltages and filters for contrast-enhanced dedicated breast CT and concluded that a tube

voltage of 60 kVp with 0.2 mm of copper would yield the highest soft-tissue contrast and microcalcification contrast.[14] The DE analysis was done using multiple ROIs varying in position within a cadaveric breast. McKinley *et al.* and Chen & Ning conducted simulation studies using the signal-to-noise ratio (SNR) instead of the CNR to calculate the DE metric for lesions embedded in a uniform breast material. The conclusions from McKinley *et al.* study showed that the use of highly attenuating filter materials with tube voltages between 50 – 70 kVp can produce maximized DE for lesions placed at the edge of a uniform phantom.[15] Chen & Ning used monochromatic spectra to determine the optimal effective energy that yields the highest DE metric to be between 30 – 40 keV, and recommended a tube voltage of 40 – 55 kVp with aluminum filtration.[5] The phantom used in this study contained three groups of several inserts varying in both radial position and z-position. The insert used to obtain the DE result, however, was not specified.

Other studies did not use the DE metric as the FOM, but generated applicable results. One study looked at the optimization of the spectrum for a lesion detectability task (instead of the CNR and dose) using the Hotelling ideal observer.[9] A range of tube voltages for various filter materials of different thicknesses were modeled and the ideal observer SNR was calculated for each case. The results showed that the optimal tube voltage was found to be approximately 40 kVp for filter materials with an atomic number between 40 and 55. For filter materials with an atomic number between 57 and 65, the optimal tube voltage was found to be 40 – 70 kVp.[9]

The methodology used by most groups for spectral optimization in dedicated breast CT is similar. Some studies use easily accessible, cost effective filtration such as aluminum and copper, to generate the ideal spectrum. The simulation studies described above, however, indicate that higher Z materials may provide an improvement in the DE metric over the common filters. The lanthanide metals (Z = 57 – 60) fit the description of an appropriate filter to achieve the maximal DE metric, according to the simulation studies.[9, 15]

Lanthanide metals have an advantage over lower atomic number filters because of their sharp k-edges[116] that allow the use of higher kVp's to obtain a narrow energy spectrum with maximum energies defined by the specific lanthanide metal used. Conclusions from the studies using lanthanide foils indicate that as the filter thickness increases, the incident spectrum becomes more monochromatic and figures of merit such as DE improve [15, 48]. Copper filtration also shows an increase in monochromatic nature with increasing filter thickness, but to a lesser extent. Figure 7.1 shows computed transmitted spectra for different thicknesses of lanthanum and copper using an initial 50 kVp tungsten anode spectrum from IPEM Report 78. The colored vertical lines represent the calculated average energy of the spectrum for each thickness of lanthanum and copper filtration. A highly monochromatic beam in the correct energy range is ideal because it will be able to separate tissues with closely matched attenuation coefficients [48]. From the figure, it is clear that the monochromatic nature of the beam increases as filter thickness increases for both the lanthanide and copper filters. We also see lower average energies in the optimal

range for lesion detection[5, 117] with the lanthanum filter, suggesting that these filters

allow for improved discrimination between low contrast objects found in

the breast.
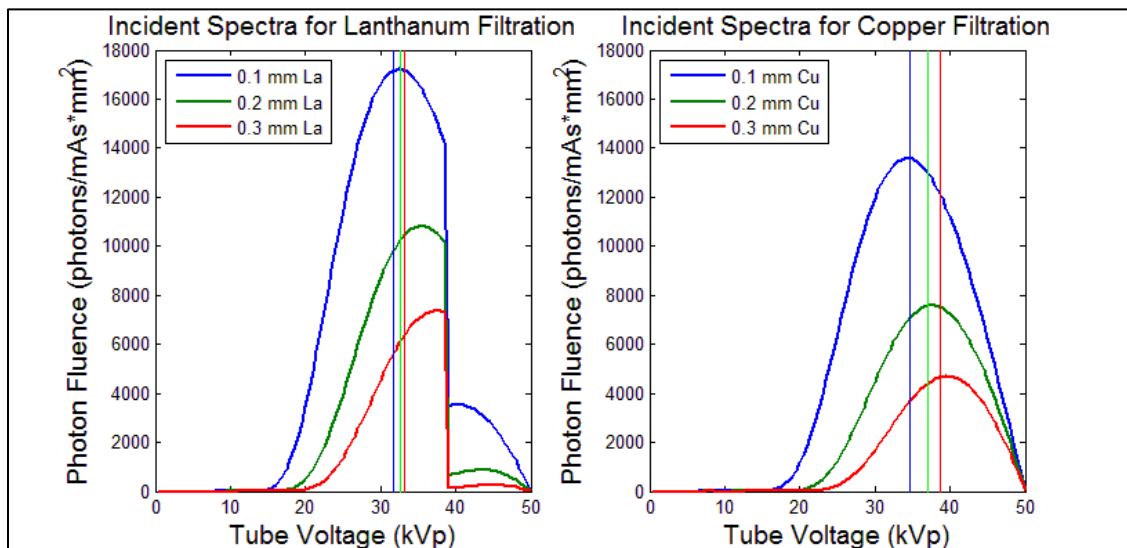
Figure 7.1: Simulated spectra using different thicknesses of lanthanum and copper filtration. With lanthanide filtration, we get a greater degree of monochromaticity with average energies in the ideal energy range. Initial spectrum is from IPEM Report 78.

While the studies described above show encouraging results for the use of

lanthanide filtration in achieving maximal DE values, the issue of tube loading was

not taken into account. As the filter thickness is increased, the intensity of the beam

is reduced and would require an increase in the mAs to obtain the same incident

fluence. To our knowledge, the necessary increase in tube-specific tube loading as a

function of filter type and thickness has not been investigated. Such information

would be useful in determining the filter type and thickness that can realistically be

implemented into an existing dedicated breast CT scanner. Part of the computational work in this chapter aims to address this issue.

One other commonality between the spectrum optimization studies previously discussed is the absence of bowtie filtration in the imaging scheme. Most of the studies investigated the DE metric as a function of a single region located at various positions of a uniform, cylindrical phantom. The image contrast and dose have been shown to change as a function of radial position due to the variation in the x-ray fluence as a function of fan-angle, so the DE metric may not be consistent for different radial positions in a cylindrical phantom. One goal of this study was to determine how the DE metric varies as a function of radial position in a cylindrical phantom, and how the inclusion of a bowtie filter affects the radial variability and magnitude of the DE. It is expected that a bowtie filter that provides an accurate spectral match of the breast tissue will improve the consistency of the DE distribution and increase its magnitude compared to the no-bowtie filter case. Based on the results from previous chapters, bowtie design #2 (BeO/B_4C) presented in this dissertation was selected and included in the simulation geometry to determine the benefits of adding bowtie filtration to the optimal spectrum.

7.2 Methods

7.2.1 Computational model

Using IPEM Report 78 data and spectra, mono-energetic and poly-energetic computations were done using a simple set-up as shown in Figure 7.2. The mono-energetic calculations investigated the required fluence through the breast to obtain a constant SNR for different energy photons and different breast diameters (Eq.7.1).

$$N = \frac{1}{(\mu_1 - \mu_2)^2 * e^{-\mu_2 * T}} \tag{7.1}$$

In this equation, N is the required photon fluence to obtain a constant SNR, μ_1 is the attenuation coefficient for the target material, μ_2 is the attenuation coefficient of the background material, and T is the thickness/diameter of the breast (Figure 7.2). For this computation, the target material was chosen to be 100% fibroglandular breast tissue, and the background material was chosen to be 50% fibroglandular/50% adipose breast tissue. The breast diameter distribution from a small group of women was found to range from 10 cm to 18 cm, so the mono-energetic calculations will cover these dimensions.[44]
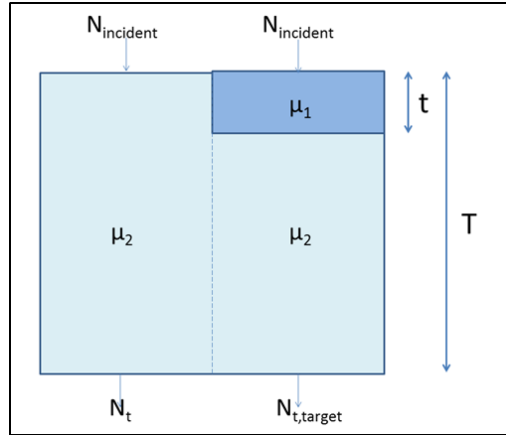
Figure 7.2: Schematic of computational set-up.

The poly-energetic spectra computations required the use of a FORTRAN program to manipulate IPEM Report 78 spectra. The input to the program included the chemical composition and thickness of the background object and target material inside of the object, chemical composition and thickness of the added filtration, and an energy range of interest. The chemical composition of the target and background was used to generate the energy-dependent attenuation coefficients (μ_1 and μ_2, respectively in Figure 7.2), which was calculated using the sum rule. A 100% fibroglandular target of thickness t in a 50% fibroglandular/50% adipose background of thickness T was used for a range of added filter thicknesses. Input spectra were manipulated to generate the incident and transmitted fluences ($N_{incident}$, N_t, and $N_{t.target}$ respectively) according to Eqs.7. 2-7.4.

$$N_{incident}(E) = N_0(E) * e^{-\mu_{filter}(E)*t_{filter}} \tag{7.2}$$

$$N_t(E) = N_{incident}(E) * e^{-\mu_2(E)*T} \tag{7.3}$$

$$N_{t,target}(E) = N_{incident}(E) * e^{-\mu_2(E)*(T-t)} * e^{-\mu_1(E)*t} \tag{7.4}$$

The attenuation coefficient of the added filtration is μ_{filter} and the thickness of this filter is t_{filter}. These fluence values were then used to compute the DE metric and an additional metric that illustrates the power required to maintain the CNR of a 50 kVp beam for various filters and filter thicknesses, called PCNR.

7.2.1.1 DE Calculation

The DE metric required the calculation of the CNR of a specified target region and the dose to that target region. The signal difference (SD) in the CNR was calculated by taking the difference between the energy fluence through the object without the target and the energy fluence through the object with the target (Eq.7.5).

$$SD = \int N_{incident}(E) * E * e^{-\mu_2(E)*T} dE - \int N_{incident}(E) * E * e^{-\mu_2(E)*(T-t)} * e^{-\mu_1(E)*t} dE \quad (7.5)$$

The noise in the CNR metric was calculated under the assumption that the energy bins were independent. The following equation describes the calculation of noise.

$$Noise = \sqrt{\Sigma_0^E E^2 \left(N_t(E) + N_{t,target}(E) \right)} \quad (7.6)$$

The ratio of these two quantities constituted the CNR to be used in the DE calculation.

The dose was simply taken to be the difference between the incident energy fluence ($N_i * E$) and the transmitted energy fluence with the target ($N_{t,target} * E$). The

DE metric was calculated for a range of tube voltages ($i = 30 - 80$ kVp) and filter

thicknesses ($j = 0 - 0.61$ mm) for breast diameters between 10 and 18 cm, in 2 cm

increments.

7.2.1.2 PCNR Calculation

In order to determine how the power requirements change as a function of

different flat filters of varying thicknesses, the PCNR metric was calculated using

adjustable parameters to a specific x-ray tube with a maximum power output, k, at a

given tube voltage. Using a 50 kVp reference spectrum with no additional filtration

and the target previously described, the power required to maintain the CNR obtained

from the reference spectrum was calculated according to Eq. 7.7 for a range of tube

voltages, i, and different filter thicknesses, j.

$$PCNR(i,j) = \frac{kVp_i}{kVp_{ref}} * \frac{CNR_{ref}}{CNR_{i,j}} * k \hspace{3cm} (7.7)$$

For the Varian G-1582BI rotating tungsten anode x-ray tube available for use in our

lab, the maximum tube current achievable for a 50 kVp spectrum was 125 mA.

Therefore, the constant, k, was 6250 W.

The PCNR was calculated for breast diameters between 10 and 18 cm, in 2 cm

increments. For each breast diameter and filter thickness, the maximum DE metric

was plotted with the corresponding PCNR.

7.2.2 Simulation set-up

In order to obtain more accurate computations of dose and to determine the effect bowtie filtration has on the consistency and magnitude of the DE metric as a function of radial position, Monte Carlo simulations were done using the PENELOPE code[50] with the penEasy_Imaging main program.[51] A 14-cm diameter cylindrical breast phantom filled with a 40% fibroglandular/60% adipose breast composition from Hammerstein *et al.* data was used.[39] According to the bowtie design specifications, the bowtie filter was placed 16.25 cm away from the source. The phantom contained three, 0.7 cm 100% fibroglandular cylindrical inserts, each spanning ± 1 cm in the z-direction from the center of the phantom for a total length of 2.0 cm. The inserts were placed 1.26, 3.15, and 5.04 cm away from the center of the phantom in the radial direction. For each projection image, the energy deposited in each insert was recorded. The sum of the energy deposition in each insert over the entire 360° acquisition was used as a surrogate for the dose to the region of interest.

The phantom was placed 73.5 cm away from the source. A similar simulation set-up was previously described in Section 3.2.5.1. The fan-angle and cone-angle collimations were set at 16.58° and 18.58°, respectively. The ideal detector with a matrix of 1536 x 2048 pixels and pixel pitch of 194 µm was placed 98.5 cm away from the x-ray source, which gives a magnification of about 1.3, similar to previous simulation and experimental studies.[5, 54]

Five different tube voltages between 30 kVp and 50 kVp in 5 kVp increments and copper filtration with a thickness of 0.1 mm were investigated. Each case was simulated with and without bowtie design #2 (BeO/B_4C). The initial spectra from

IPEM Report 78 were filtered with 0.8 mm of beryllium and 2.0 mm aluminum to account for the inherent filtration from the x-ray tube used in the lab. The cylindrical phantom was rotated in 1.2° increments over 360° to obtain 300 projection images. 10^{10} photons were simulated per projection view for each case.

The projection images were used in an FDK filtered back projection reconstruction algorithm[52, 53] to generate a 1000 x 1000 x 30 reconstructed volume with a pixel size of 0.1448 mm and 1 mm slice thickness. For each cylindrical insert, a 30 x 30 pixel ROI was selected within the insert. The same size uniform background region used as noise in the calculation of the CNR was selected to be the same radial distance from the center as a given insert. The CNR was only calculated on slices that fully contained the inserts in the reconstructed volume. The CNR values from all relevant slices were averaged. This value was squared, and normalized by the total energy deposited in the given insert to obtain the DE for that specific location and case.

7.3 Results

7.3.1 Computational analysis

7.3.1.1 Monoenergetic calculations

The results from the mono-energetic calculations are shown in Figure 7.3. Each of the curves represents the photon fluence required to maintain an arbitrary SNR at different photon energies for different breast thicknesses.
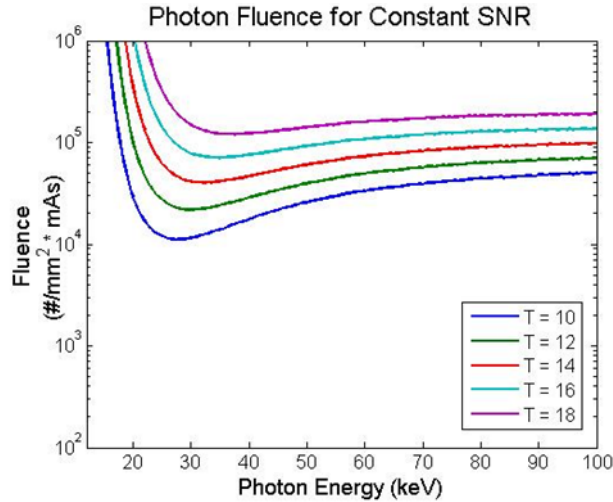
Figure 7.3: Monoenergetic calculation illustrating the photon fluence required to maintain a constant SNR given a 100% fibroglandular target embedded in a 50% fibroglandular/50% adipose breast tissue background of various thicknesses.

For photon energies less than 30 keV, there is a sharp decrease in the required fluence, down to a minimum value that occurs at increasing energy as breast thickness increases. Beyond this value, however, the required fluence increases more slowly, indicating that there is a large range of energies that can produce a reasonable SNR without increasing the dose to the patient by large factors.

7.3.1.2 Polyenergetic calculations

The computations from the poly-energetic spectra are shown in Figures 7.4 and 7.5. Figure 7.4 shows a plot of DE vs. tube voltage for neodymium filters of

various thicknesses, ranging from 0 - 0.61 mm. The DE metric peaks between 33 and

40 kVp for all thicknesses of the neodymium filter. Since the k-edge of the lanthanide

filters ranges between 38 and 43 keV[116], these filters will act as regular beam-

hardening filters with tube voltages lower than 40 kVp. This trend is also seen with

other lanthanide filters of various thicknesses as well as copper filtration.
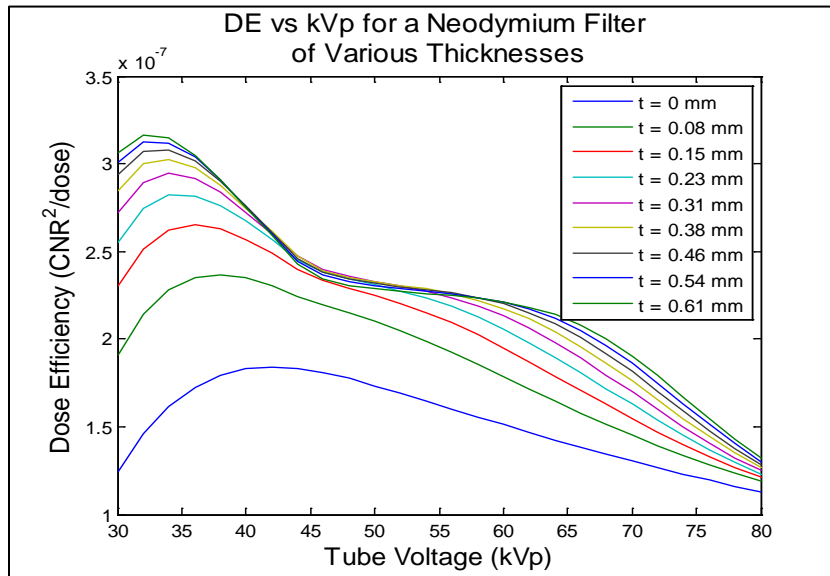
Figure 7.4: Dose efficiency vs. tube voltage for a neodymium filter of various
thicknesses.

The differences between the lanthanide filtration and the copper filtration can

be seen between the tube voltages of 40 – 60 kVp. In this range, the DE is fairly flat

for neodymium filter thicknesses greater than 0.23 mm. As the tube voltage is

increased beyond 60 kVp, the DE metric decreases. Again, this trend was seen with

other lanthanide filters. In comparison, the DE metric with copper filtration decreases

with increasing tube voltage for all filter thicknesses.

A plot of the power required to obtain a CNR equivalent to that of a 50 kVp beam versus the DE for the neodymium filter is shown in Figure 7.5. Each curve represents a different breast thickness, ranging from 10 cm to 18 cm. The DE value at the optimal kVp was used for each filter thickness in this plot. Each point on the curve denotes a specific filter thickness, starting from 0 to 0.61 mm. From this plot, the dependence of DE on power limitations can clearly be seen. With lower filter thicknesses, the power requirements remain low. As the filter thickness increases, the power requirement increases. The fourth data point in the power vs. DE plots for each lanthanide filter, corresponding to a thickness of 0.23 mm for the neodymium filter, appears to be the transition point from slow increase to rapid increase. Similar trends are seen for various other lanthanide filters and also copper filtration.
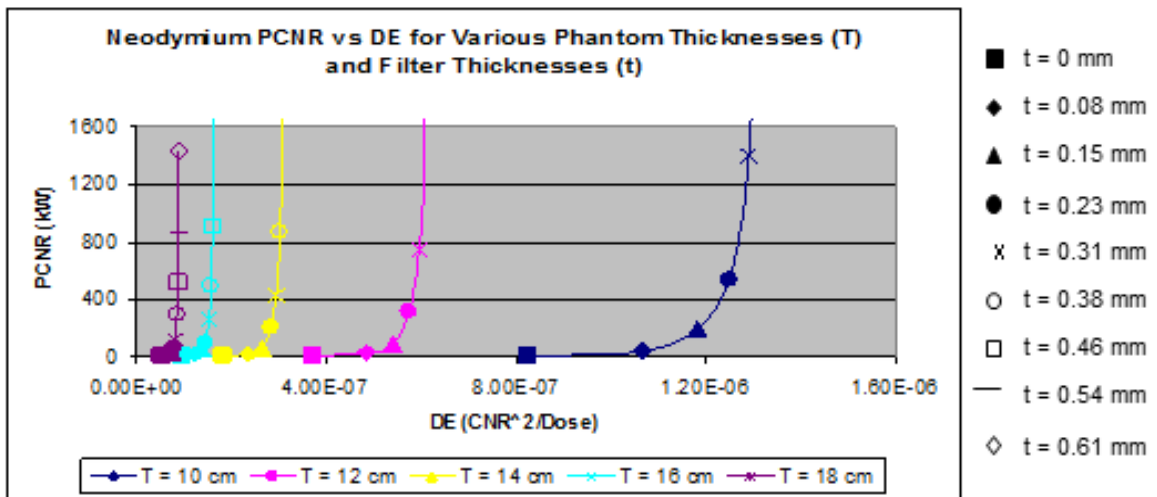
Figure 7.5: Power required to obtain the CNR of a 50 kVp beam as a function of dose efficiency. Each point of each curve represents a different filter thickness.

7.3.2 Simulation analysis

The projection images acquired with or without a bowtie filter, and with various tube voltages, and 0.1 mm copper filtration were reconstructed and analyzed to determine the DE metric as a function of radial position.

Figures 7.6 and 7.7 show the DE metric as a function of position and tube voltage with and without bowtie design #2 using 0.1 mm Cu. Both the primary and primary + scatter projection images were used to reconstruct a 3D volume, and used to compute the DE metric as a function of position.

As the tube voltage increases, the DE metric also increases. For both the primary and primary + scatter data sets, the inclusion of the bowtie filter increases the DE value for most positions at different tube voltages. The DE value also appears to be more consistent as a function of position when bowtie design #2 is used.
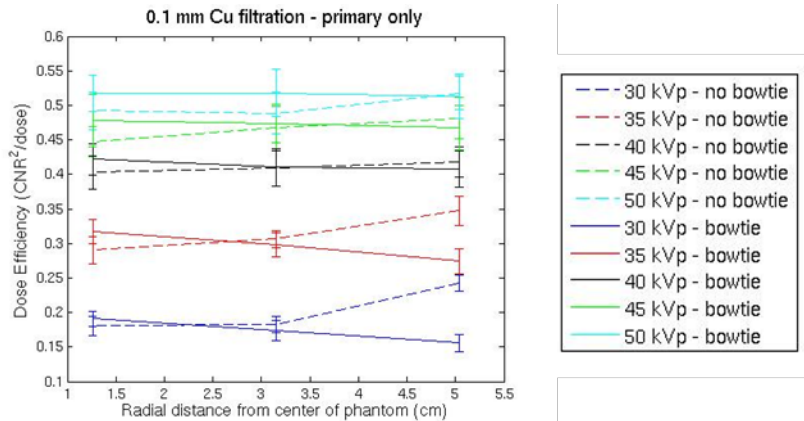
Figure 7.6: DE metric calculated from simulation data both with and without bowtie design #2 for various tube voltages. The DE was calculated using the reconstructed volume from the primary only projection images. The flat filter used in these data was 0.1 mm Cu.
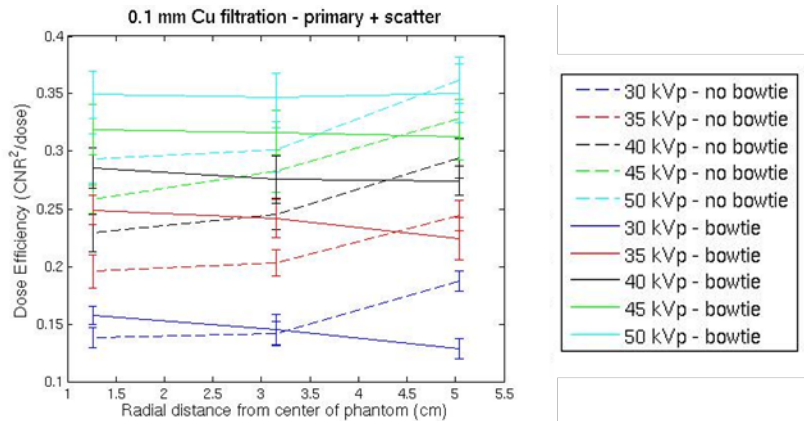
Figure 7.7: DE metric calculated from simulation data both with and without bowtie design #2 for various tube voltages. The DE was calculated using the reconstructed volume from the primary + scatter projection images. The flat filter used in these data was 0.1 mm Cu.

To further investigate the distribution of the DE metric from the center insert to the peripheral insert, the percent difference between the center DE value and peripheral DE value was calculated for each tube voltage, with and without the bowtie filter for the 0.1 mm Cu case. The results are shown in Figure 7.8.
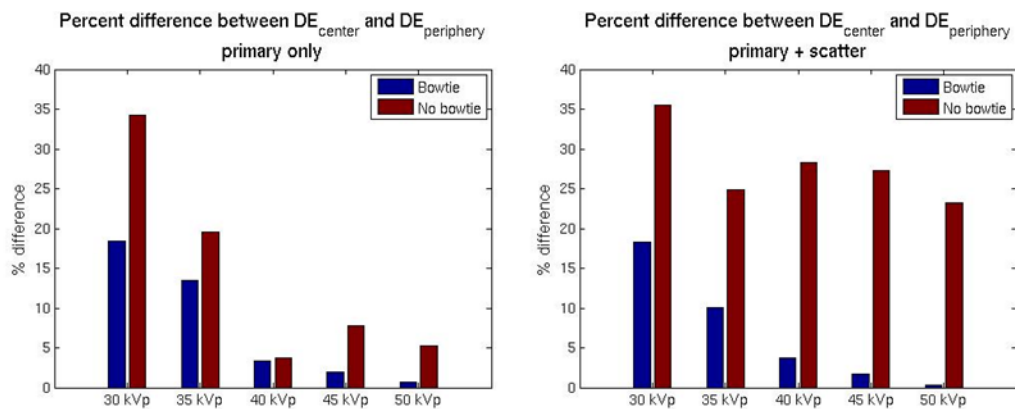
Figure 7.8: Percent difference between the center DE value and peripheral DE value with and without bowtie design #2 for various tube voltages using 0.1 mm Cu filtration. (Left) The primary only reconstructed volume was used to compute the DE. (Right) The primary + scatter reconstructed volume was used to compute the DE.

163

Without the bowtie filter, the percent difference from the center DE value to the

peripheral DE value is substantially larger than the percent difference seen with the

bowtie filter. This is true for all tube voltages in both the primary only and primary +

scatter calculations, excluding the 40 kVp primary only calculation.

7.4 Discussion

A review of the literature for optimal spectra for dedicated breast CT shows

inconsistent results. Several groups determined the optimal spectrum to vary between

40 and 70 kVp using various filtration. For these studies, the position of the ROI for

the DE calculation varied, and these groups failed to investigate how the DE metric

would change as a function of position. They also neglected to take into account tube

loading limitations of the currently available x-ray sources and generators for

dedicated breast CT. In addition, none of the studies implemented bowtie filtration in

the hunt for the optimal spectrum.

The results from this study presented computational work that examined the

common FOM for spectral optimization studies, the DE, but also examined a new

metric that describes the tube loading limitations. Figure 7.4 shows that for our

model, the DE peaks between 33 and 40 kVp for the case with a neodymium filter.

This trend is seen with most of the lanthanide filters as well as copper filtration.

These tube voltages, although realistic in mammography, are not realistic with the

currently available x-ray sources and generators in CT. If we look at the curves

between tube voltages of 40 kVp to 60 kVp, an interesting pattern is seen with all the lanthanide filters. As the filter thickness increases from 0 mm to approximately 0.3 mm, a distinct increase in the DE can be seen in this range. Beyond a certain thickness, however, the DE does not significantly change. As shown previously, increasing the filter thickness will increase the monochromaticity of the incident beam, but Figure 7.4 shows that there is very little benefit to using more filtration in terms of the DE. These results and the results from the mono-energetic calculations led to the conclusion that the optimal spectrum is limited by tube loading (power) constraints. That conclusion was further strengthened when looking at Figure 7.5 showing the PCNR as a function of the maximum DE for each filter thickness.

One limitation of the computational study is the calculation of the dose as the difference between the incident energy fluence and the transmitted energy fluence through the breast model. In order to make these computations more accurate, a database providing the dose deposition through the phantom model could be created as a function of photon energy.[22, 44]

The simulation results investigated the DE distribution both with and without bowtie design #2 (BeO/B_4C). For nearly all cases, which consisted of different tube voltage, filter type and filter thickness, the use of the bowtie filter improved the magnitude and uniformity of the DE metric for different radial positions in the uniform cylindrical phantom. These results show that with the use of a bowtie filter, the DE can be optimized independent of position in the phantom.

The percent difference between the center and peripheral DE values with the bowtie filter is much less than the percent difference seen without using a bowtie

filter. In Monte Carlo simulations, it is possible to collect projection images with no

scatter contamination and use those images in a reconstruction algorithm. The left

plot of Figure 7.8 examines the percent difference in the DE for glandular inserts

from center to periphery for the scatter-free case. The bowtie filter case is more

efficient in providing a uniform DE distribution for this scatter-free case, but this is

an unrealistic scenario in clinical and experimental applications. Although there are

several correction and reduction techniques to alleviate the issue of scatter

contamination, a perfectly scatter-free case as the one achieved in Monte Carlo

simulations is not possible. Therefore, it is more informative to look at the right plot

of Figure 7.8: the primary + scatter simulation. When scatter is included in the

simulation, there is a greater difference between the uniformity achieved with and

without a bowtie filter since the inclusion of scatter increases the variation in DE

without a bowtie filter as a function of radial position to be between 25% and 35%.

Chapter 8: Future work

8.1 Experimental validation of bowtie design #2 and optimal spectrum determination

Experimentation was done with bowtie design #1 (Al) and bowtie design #3 (PMMA) to validate the design outcomes and evaluate the results given parameters that differ from that of the standard breast. It was stated that bowtie design #2 (BeO/B$_4$C) could not be realized in a physical form due to limitations in cost and fabrication difficulties. Future work could include fabrication of this bowtie filter design and further experimental validation and evaluation.

In Chapter 7, a simulation framework was laid out for the determination of the optimal spectrum in dedicated breast CT with the use of bowtie filters. It was determined computationally that the optimal spectrum may be in the mammography range, but this was not able to be tested experimentally. The Varian G1582BI x-ray tube utilized in experiments could not operate below 40 kVp. Furthermore, at 40kVp the emission is space-charge limited, meaning that increases in the filament current will not produce increases in the tube current. Recently, Varian Medical Systems introduced a new x-ray tube technology specifically designed for dedicated breast CT and other mammography-related imaging.[118] This new tube technology is capable of achieving larger fluence outputs at lower tube voltages, so experiments determining

the optimal spectrum over the range of tube voltages tested computationally and in simulations can be realized.

8.2 Design and implementation of an anthropomorphic bowtie filter

A few groups have designed bowtie filters for dedicated breast CT with varying design goals. All designs, however, have used the simplifying assumption representing the breast as a cylindrical object. This alleviates the need to vary the bowtie filter thickness in the z-direction since the xy-plane cross-section of a cylinder is the same for all z values. This assumption is not clinically accurate as the pendant breast more closely resembles a half ellipsoid[5] with a varying xy-plane cross section as a function of z. Using the bowtie filters designed for a cylindrical object on a half-ellipsoidal object will not provide the dose reduction and image quality improvements shown in this dissertation for all xy-planes. By using a half-ellipsoid shape as the standard breast and determining the variation in the cross-sectional diameter as a function of z, an anthropomorphic bowtie filter could be designed.

Chen and Ning represented the breast as a half-ellipsoid with three half-axes equal to r, r, and 2r, where r is the radius of the breast.[5] The half-ellipsoidal shape can be defined by the following equation:

$$\left(\frac{x-x_c}{r}\right)^2 + \left(\frac{y-y_c}{r}\right)^2 + \left(\frac{z-z_c}{2r}\right)^2 = 1 \tag{8.1}$$

In this equation, x_c, y_c, and z_c denote the center of the ellipse. Since the shape of the breast is rotationally symmetric using this model, one plane can be investigated to determine the relevant cross-sectional diameters. If we look at only the xz-plane and assume that y = 0, then the equation describing the half-ellipsoid simplifies to the equation of a circle.

There are two conditions to consider when designing the anthropomorphic bowtie filter using the previously presented methodology in this dissertation: the fan-beam case (a simplified case) and the cone-beam case. Both cases will result in different values of the cross-sectional diameter as a function of z. The two cases are illustrated in Figure 8.1.
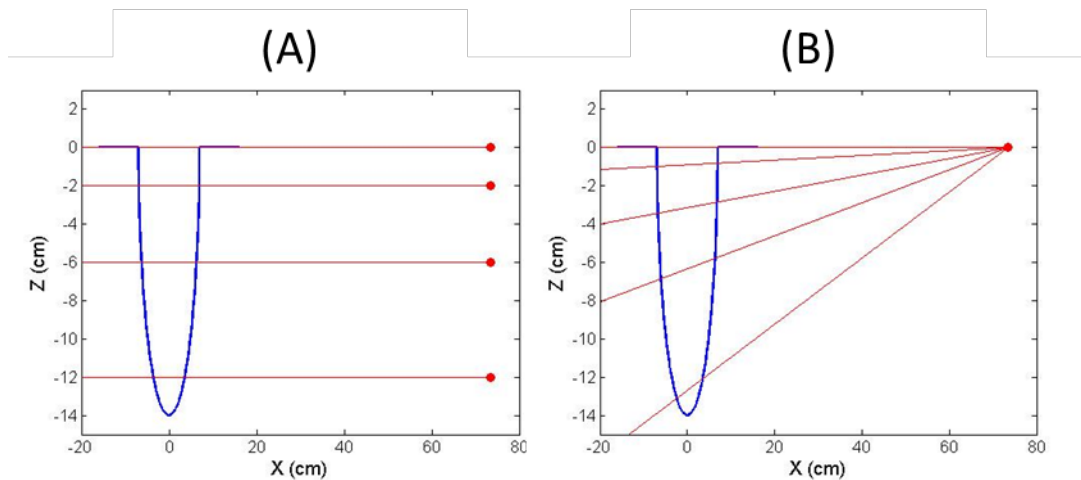
Figure 8.1: Ray traces through the half-ellipsoidal shape representing the pendant breast for the (A) fan-beam case and the (B) cone-beam case from a point source 73.5 cm away from the center of the breast. Each plot shows the half-ellipsoidal shape in the xz-plane.

To develop the initial framework needed for such a design, an anthropomorphic bowtie filter was designed assuming the fan-beam case for bowtie design #3. The three axes of the half-ellipsoidal breast shape were assumed to be 7, 7, and 14 and the source was assumed to be 73.5 cm away from the center of the

169

breast. For the purposes of the bowtie filer design, the SFD was assumed to be 16.25 cm. For each z position, the path length through the cross-section was determined for all fan-angles from -5.4° to 5.4°. These path lengths were then used to determine the necessary filter thickness needed to achieve the same effective attenuation coefficient through the center of the breast phantom at z = 0 for every z position. The 3D plot in Figure 8.2 shows the resulting thickness of the bowtie filter as a function of z position.
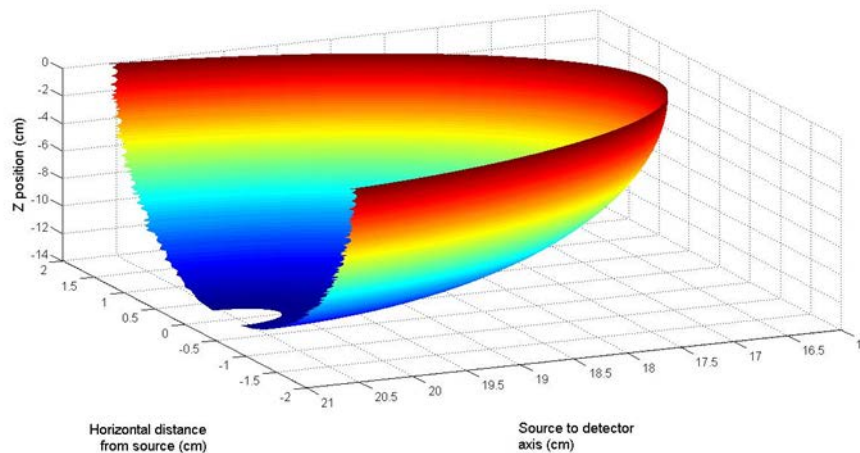
Figure 8.2: 3D plot of an anthropomorphic bowtie filter of design #3 assuming a fan-beam geometry. The different colors represent the filter shape for a given z position.

Although an initial design of an anthropomorphic bowtie filter has been presented, there are several analyses that would need to be done to investigate the benefits of such a design. The geometry shown in Figure 8.2 could be converted to geometry in the Monte Carlo PENELOPE environment to conduct simulations of x-ray transport in a dedicated breast CT set-up, with and without the anthropomorphic bowtie filter. The dose and dose distribution could be evaluated and compared

between the anthropomorphic bowtie filter case, regular bowtie filter case, and no-bowtie filter case. Also, the scatter and various image quality metrics could be investigated.

8.3 Noise characterization and lesion detectability

The ability of each bowtie filter to improve the noise uniformity from the center of a cylindrical phantom to the periphery was established in this dissertation. Due to the clinical importance of noise uniformity in low contrast detectability, the inclusion of bowtie filters in the imaging scheme of dedicated breast CT may substantially improve specificity and sensitivity of the device. The noise UI used to in this dissertation, however, is a limited metric of noise characterization since it is based on the standard deviation or variance of the pixels in the image.[119, 120] While the variance is easy to calculate, it may not fully reflect the impact that noise will have on certain diagnostic tasks.[119] The noise power spectrum (NPS) under the assumption of noise stationarity is a more powerful metric for characterizing the noise in the acquired CT images since it is able to account for correlations[119, 121] and also predict detection performance.[122, 123] Future work would focus on the inclusion of a more complete analysis of the noise with and without the different bowtie filters using the more informative metric, the NPS.

As a starting point, the NPS was calculated from simulated projection images of a uniform cylindrical phantom, reconstructed using an FDK filtered backprojection

algorithm both with and without bowtie design #1 (Al), bowtie design #2 (BeO/B$_4$C), and bowtie design #3 (PMMA). The reconstructed volume contained isotropic 0.1448 mm^3 pixel voxels with 500 slices. Three different regions in the reconstructed volume were extracted and used to compute the location-dependent NPS. Figure 8.3 shows the 40 x 40 pixel ROIs extracted from each of the 500 slices in the reconstructed volume.
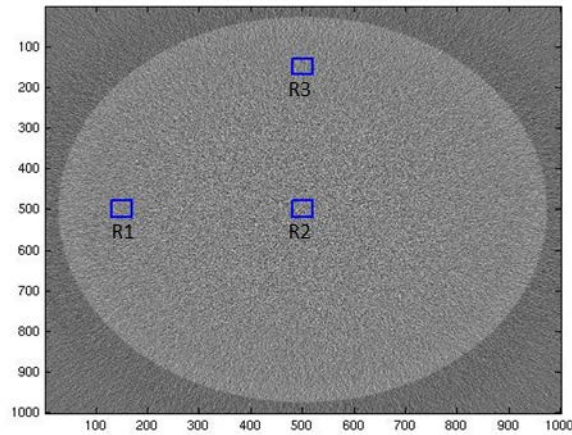
Figure 8.3: A single slice from the reconstructed volume used to compute the location-dependent NPS. The blue squares labeled R1, R2, and R3 show the regions extracted from each slice for the NPS analysis.

The NPS was calculated for each slice, and the results were averaged to decrease the uncertainty. For a given slice and region, the mean pixel value was subtracted from all pixels in the region. A Hann window was applied to reduce the spectral leakage.[124] The averaged 2D NPS from each region for the bowtie/no-bowtie filter case was plotted for each bowtie filter type in Figures 8.4-8.6.

Figure 8.4 shows the 2D NPS with and without bowtie design #1 (Al). Both with and without the bowtie filter, there is evidence of different directionality in the noise images depending on the location. R1, R2, and R3 show vertical, isotropic, and horizontal noise structure, respectively. Similar results were seen in a previously reported study.[112, 119, 125] The difference in directionality is due to a difference in the number of photons traveling through the designated regions at different acquisition (gantry) angles. If the reconstructed image in Figure 8.3 represents the top-view of an object being imaged with the x-ray source some distance away along the line $y = 500$, the number of photons traveling through R1 would be less than the number of photons traveling through R3. This would cause the 2D NPS to have higher amplitude in the y-direction, as seen in the first plots in Figure 2. When the source is rotated 90° such that it lies some distance away along the line $x = 500$, the situation reverses and more photons travel through R3, causing an increase in the 2D NPS amplitude in the x-direction. The same number of photons travels through R2 independent of the gantry angle, so the 2D NPS is isotropic in this region. Between the bowtie and no-bowtie filter cases, the magnitude of the NPS does not vary greatly, but we do see trending toward a more isotropic noise structure with the inclusion of bowtie design #1 (Al). These differences are very subtle, however.
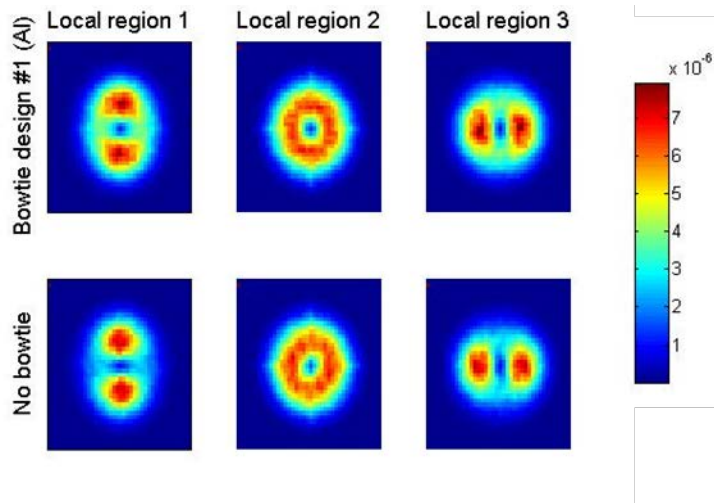
Figure 8.4: Location-dependent 2D NPS with and without bowtie design #1 (Al). The bowtie/no-bowtie filter cases are each plotted on the same scale.

Figure 8.5 shows the 2D NPS with and without bowtie design #2 (BeO/B$_4$C). The no-bowtie filter case shows evidence of directionality differences in the different regions for reasons previously stated. With the inclusion of bowtie design #2, however, the 2D NPS in all regions become isotropic, with slightly larger magnitude in the peripheral regions. Similar results were shown by Wunderlich and Noo[126] in their work on image covariance and lesion detectability. With the inclusion of a bowtie filter, it was shown that the correlation coefficient remains fairly symmetric, independent of location in the image. The removal of directionality differences for different locations in an image would be important in the detection of anisotropic lesions.[119, 125]
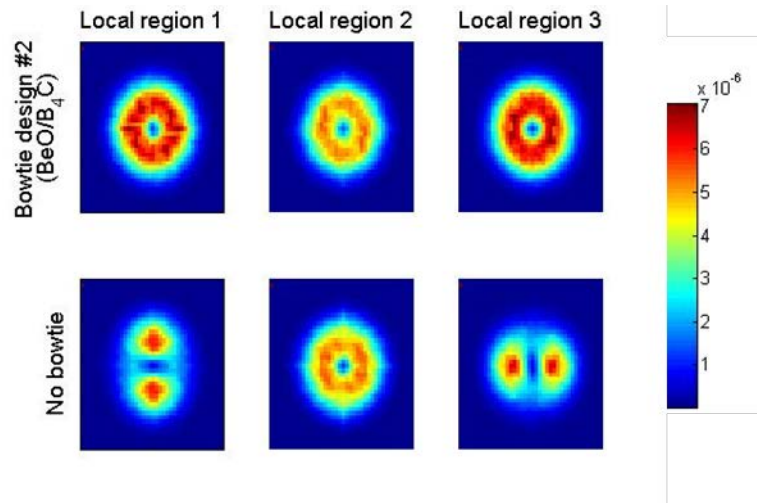
Figure 8.5: Location-dependent 2D NPS with and without bowtie design #2 (BeO/B$_4$C). The bowtie/no-bowtie filter cases are each plotted on the same scale.

Figure 8.6 shows the 2D NPS with and without bowtie design #3 (PMMA). Very similar results seen with bowtie design #1 (Al) are seen here.
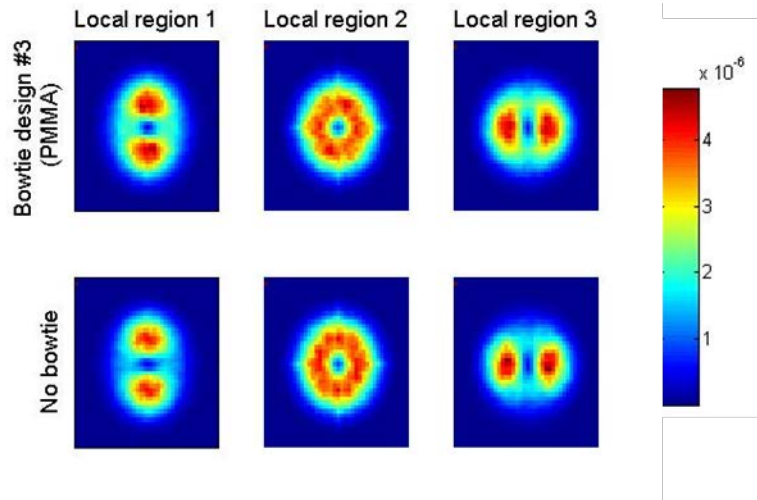

Figure 8.6: Location-dependent 2D NPS with and without bowtie design #3 (PMMA). The bowtie/no-bowtie filter cases are each plotted on the same scale.

These results are encouraging and informative, but many more analyses on noise characterization could be done. The initial results presented here only look at

the 2D NPS in the x-y plane of a cylindrical, uniform phantom. With the design of an anthropomorphic bowtie filter, simulations and experiments could be done evaluating the NPS as a function of position in the z-direction as well. Several groups have developed methodology to investigate the 3D NPS,[121, 125, 127] but none have investigated the effects of bowtie filtration with the specific design traits of the bowtie filters presented in this work.

In addition to noise characterization, the effect of our bowtie filter designs on lesion detectability of various types of lesions (isotropic vs. anisotropic, etc.) could be investigated as a function of radial distance and z-direction for an anthropomorphic phantom. Wunderlich and Noo performed area under the curve (AUC) analyses for a binary detection task of a lesion in various radial locations with and without a bowtie that was designed to perfectly equalize the attenuation of the object.[126] Their results indicated that the inclusion of a bowtie filter provides uniform AUC values as a function of radial distance compared to substantial increases in the AUC as a function of radial distance from the center. The bowtie filter used in the Wunderlich and Noo study is similar to bowtie design #2 (BeO/B_4C), but a thorough investigation of all three bowtie filter types should be completed. Additional work on the comparison of two methods to calculate the SNR showed that signal transfer could be affected by the change in the point spread function (PSF) for larger distances from the center of a cylindrical phantom.[112] An investigation of how this PSF changes as a function of radial position with and without the bowtie filter may also be of interest since this metric will also affect the detectability.

Chapter 9: Conclusions

Dedicated breast CT is an emerging technology that can alleviate the issue of tissue superpositioning that arises from acquiring a two-dimensional image of a three-dimensional object. Given the relatively symmetric shape of the breast and homogeneous tissue composition compared to other regions of the body, dedicated breast CT is a prime candidate for bowtie filter implementation. In this dissertation, three bowtie filters that all provided different outcomes were designed and extensively validated and evaluated. Integration of these bowtie filters into the hunt for the optimal spectrum was also done through means of Monte Carlo simulation.

The theoretical basis of each bowtie filter design was described. For each bowtie filter, a computational model was created and used in Matlab programming to validate and evaluate the design against variations in the design input parameters, such as breast diameter, breast composition, and tube voltage. The plots of the HVL, transmitted energy fluence, and effective attenuation coefficient (all as a function of fan-angle) provided validation for each design. In looking at varying design input parameters using the bowtie filter designed for a specific standard breast, results showed the designs to be robust, with the largest variation occurring with different breast diameters.

To obtain a more realistic understanding of the behavior and benefits of implementing these bowtie filter designs into dedicated breast CT imaging scheme, Monte Carlo simulations using PENELOPE with the penEasy_Imaging package were

done. Cylindrical phantoms of various diameters were created in the PENELOPE geometry environment, as well as each bowtie filter evaluated computationally. These simulations allowed us to look at the beam hardening artifacts, dose distribution, noise homogeneity and CNR homogeneity for each bowtie filter. A more in-depth analysis of the scatter characterization using each bowtie filter and an analysis of the trade-offs between using different materials for each bowtie filter type was also done using simulations.

Physical prototypes of two of the three bowtie filters were fabricated. This allowed us to validate the designs experimentally. Using radiation field mapping techniques and reconstructed volumes of projection images, the design goals of the bowtie filters were validated and evaluated. The experimental results show that the designs are robust against variation in design input parameters. Scatter measurements were also done using a beam-block method to show the reduction in scatter with the use of our bowtie filters.

Based on these computational, simulation, and experimental results, we were able to show that the inclusion of these bowtie filters in the dedicated breast CT geometry can reduce scatter contamination, provide uniform dose and noise distribution, generate CNR homogeneity, and address the issue of beam hardening. One design in particular, bowtie design #2, was more consistent in all calculated/measured parameters, independent of the material chosen. For this reason, bowtie design #2 was selected to demonstrate the benefit of including bowtie filtration in the hunt for the optimal spectrum.

The computational results investigating the optimal spectrum demonstrated the limiting factor of tube loading in determining the optimal spectrum. Taking these findings into account, an initial simulation study was conducted to develop a framework for determining the optimal spectrum in dedicated breast CT and to elucidate the benefit of adding bowtie filters to the imaging scheme. Using various thicknesses of lanthanide filtration and copper filtration, and cases both with and without bowtie design #2, the DE metric was calculated as a function of radial position in a uniform cylindrical phantom. The initial results showed that the inclusion of the bowtie filter created a substantially more uniform distribution of the DE metric, and, for some cases, and increase in the magnitude of the DE metric. Given the inconsistencies in the reported optimal spectrum from various groups, these results indicate that the use of a bowtie filter could provide better, more consistent FOMs.

Bibliography

1   S.A. Feig, "Decreased breast cancer mortality through mammographic screening: results of clinical trials," Radiology **167**, 659-665 (1988).

2   L.G. Larsson, L. Nystrom, S. Wall, L. Rutqvist, I. Andersson, N. Bjurstam, G. Fagerberg, J. Frisell, L. Tabar, "The Swedish randomised mammography screening trials: analysis of their effect on the breast cancer related excess mortality," J Med Screen. **3**, 129-132 (1996).

3   C.J. Lai, C.C. Shaw, L. Chen, M.C. Altunbas, X. Liu, T. Han, T. Wang, W.T. Yang, G.J. Whitman, S.J. Tu, "Visibility of microcalcification in cone beam breast CT: effects of X-ray tube voltage and radiation dose," Med Phys **34**, 2995-3004 (2007).

4   D.S. Buist, P.L. Porter, C. Lehman, S.H. Taplin, E. White, "Factors contributing to mammography failure in women aged 40-49 years," Journal of the National Cancer Institute **96**, 1432-1440 (2004).

5   B. Chen, R. Ning, "Cone-beam volume CT breast imaging: feasibility study," Med Phys **29**, 755-770 (2002).

6   S.J. Glick, "Breast CT," Annu.Rev.Biomed.Eng. **9**, 501-526 (2007).

7   E.A. Morris, L.H. Schwartz, D.D. Dershaw, K.J. van Zee, A.F. Abramson, L. Liberman, "MR imaging of the breast in patients with occult primary breast carcinoma," Radiology **205**, 437-440 (1997).

8   J.M. Boone, T.R. Nelson, K.K. Lindfors, J.A. Seibert, "Dedicated breast CT: radiation dose and image quality evaluation," Radiology **221**, 657-667 (2001).

9   S.J. Glick, S. Thacker, X. Gong, B. Liu, "Evaluating the impact of X-ray spectral shape on image quality in flat-panel CT breast imaging," Med Phys **34**, 5-24 (2007).

10   A. O'Connell, D.L. Conover, Y. Zhang, P. Seifert, W. Logan-Young, C.F. Lin, L. Sahler, R. Ning, "Cone-beam CT for breast imaging: Radiation dose, breast coverage, and image quality," AJR.Am J Roentgenol. **195**, 496-509 (2010).

11   N.D. Prionas, K.K. Lindfors, S. Ray, S.Y. Huang, L.A. Beckett, W.L. Monsky, J.M. Boone, "Contrast-enhanced dedicated breast CT: initial clinical experience," Radiology **256**, 714-723 (2010).

12   J.D. Silkwood, K.L. Matthews, P.M. Shikhaliev, "Photon counting spectral breast CT: effect of adaptive filtration on CT numbers, noise, and contrast to noise ratio," Med Phys **40**, 051905 (2013).

13   M. Weigel, S.V. Vollmar, W.A. Kalender, "Spectral optimization for dedicated breast CT," Med.Phys. **38**, 114-124 (2011).

14   N.D. Prionas, S.Y. Huang, J.M. Boone, "Experimentally determined spectral optimization for dedicated breast computed tomography," Med.Phys. **38**, 646-655 (2011).

15   R.L. McKinley, M.P. Tornai, E. Samei, M.L. Bradshaw, "Simulation study of a quasi-monochromatic beam for x-ray computed mammotomography," Med Phys **31**, 800-813 (2004).

16   J. Hsieh, *Computed Tomography: Principles, Design, Artifacts,and Recent Advances*, Second ed. (SPIE, Bellingham, Washington, 2009).

17   G.J. Bootsma, F. Verhaegen, D.A. Jaffray, "The effects of compensator and imaging geometry on the distribution of x-ray scatter in CBCT," Med Phys. **38**, 897-914 (2011).

18   S.A. Graham, D.J. Moseley, J.H. Siewerdsen, D.A. Jaffray, "Compensators for dose and scatter management in cone-beam computed tomography," Med.Phys. **34**, 2691-2703 (2007).

19   N. Mail, D.J. Moseley, J.H. Siewerdsen, D.A. Jaffray, "The influence of bowtie filtration on cone-beam CT image quality," Med Phys **36**, 22-32 (2009).

20   R.J. Jennings, "A method for comparing beam-hardening filter materials for diagnostic radiology," Med.Phys. **15**, 588-599 (1988).

21   R.J. Jennings, "Computational Methods for the Design of Test Objects and Tissue Substitutes for Radiologic Applications," Radiation Protection Dosimetry **49**, 327-332 (1993).

22   F. Rupcich, A. Badal, I. Kyprianou, T.G. Schmidt, "A database for estimating organ dose for coronary angiography and brain perfusion CT scans for arbitrary spectra and angular tube current modulation," Med Phys **39**, 5336-5346 (2012).

23   S.S. Hsieh, D. Fleischmann, N.J. Pelc, "Dose reduction using a dynamic, piecewise-linear attenuator," Med Phys **41**, 021910 (2014).

24   S.S. Hsieh, N.J. Pelc, "The feasibility of a piecewise-linear dynamic bowtie filter," Med Phys **40**, 031910 (2013).

25   T.P. Szczykutowicz, C.A. Mistretta, "Design of a digital beam attenuation system for computed tomography. Part II. Performance study and initial results," Med.Phys. **40**, 021906 (2013).

26   T.P. Szczykutowicz, C.A. Mistretta, "Design of a digital beam attenuation system for computed tomography: part I. System design and simulation framework," Med.Phys. **40**, 021905 (2013).

27   R.L. Egan, *Breast Imaging: Diagnosis and Morphology of Breast Diseases*. (W.B. Saunders Company, Philadelphia, PA, 1988).

28   *ICRU Report 44: Tissue Substitutes in Radiation Dosimetry and Measurements*. (International Commission on Radiological Units and Measurements, 1989).

29   A.L. Kwan, J.M. Boone, N. Shah, "Evaluation of x-ray scatter properties in a dedicated cone-beam breast CT scanner," Med Phys **32**, 2967-2975 (2005).

30   F. Luck, D. Kolditz, M. Hupfer, W.A. Kalender, "Effect of shaped filter design on dose and image quality in breast CT," Phys.Med Biol. **58**, 4205-4223 (2013).

31   W. Mayneord, J. Roberts, "The 'quality' of high voltage radiations. I," Br.J Radiol. **8**, 341 (1935).

32   R. Thoraeus, "A study of the ionization method for measuring the intensity and absorption of Roentgen rays and of the efficiency of different filters used in therapy," Acta Radiol **Suppl 15**1932).

33	R.E. Alvarez, A. Macovski, "Energy-selective reconstructions in X-ray computerized tomography," Phys Med Biol **21**, 733-744 (1976).
34	F.E. Carroll, J.W. Waters, W.W. Andrews, R.R. Price, D.R. Pickens, R. Willcott, P. Tompkins, C. Roos, D. Page, G. Reed, et al., "Attenuation of monochromatic X-rays by normal and abnormal breast tissues," Investigative radiology **29**, 266-272 (1994).
35	P.C. Johns, M.J. Yaffe, "X-ray characterisation of normal and neoplastic breast tissues," Phys.Med.Biol. **32**, 675-695 (1987).
36	A. Tomal, I. Mazarro, E.M. Kakuno, M.E. Poletti, "Experimental determination of linear attenuation coefficients of normal, benign, and malignant breast tissues," Radiation Measurements **45**, 1055-1059 (2010).
37	P. Madhav, C.M. Li, M.P. Tornai, "Development of in vivo characterization of breast tissues through absolte attenuation coefficients using dedicated cone-beam CT," Proc. SPIE, 7622091-76220911 (2010).
38	E. Trout, J. Kelley, A. Lucas, "Evaluation of Thoraeus filters," Am. J. Roentgenol. **85**, 933 (1961).
39	G.R. Hammerstein, D.W. Miller, D.R. White, M.E. Masterson, H.Q. Woodard, J.S. Laughlin, "Absorbed radiation dose in mammography," Radiology **130**, 485-491 (1979).
40	W. McMaster, N. Del Grande, J. Mallett, J. Hubbell, "Compilation of X-ray Cross Sections," (University of California, Lawrence Radiation Laboratory, 1969).
41	W.A. Kalender, W.H. Perman, J.R. Vetter, E. Klotz, "Evaluation of a prototype dual-energy computed tomographic apparatus. I. Phantom studies," Med Phys **13**, 334-339 (1986).
42	A. Sonzogni, "National Nuclear Data Center Chart of Nuclides," (www.nndc.bnl.gov/chart, 2014).
43	W.P. Argo, K. Hintenlang, D.E. Hintenlang, "A tissue-equivalent phantom series for mammography dosimetry," Journal of applied clinical medical physics / American College of Medical Physics **5**, 112-119 (2004).
44	J.M. Boone, N. Shah, T.R. Nelson, "A comprehensive analysis of DgN(CT) coefficients for pendant-geometry cone-beam breast computed tomography," Med.Phys. **31**, 226-235 (2004).
45	P.M. Shikhaliev, "Energy-resolved computed tomography: first experimental results," Phys Med Biol **53**, 5595-5613 (2008).
46	P.M. Shikhaliev, "Projection x-ray imaging with photon energy weighting: experimental evaluation with a prototype detector," Phys Med Biol **54**, 4971-4992 (2009).
47	M.J. Yaffe, J.M. Boone, N. Packard, O. Alonzo-Proulx, S.Y. Huang, C.L. Peressotti, A. Al-Mayah, K. Brock, "The myth of the 50-50 breast," Med Phys. **36**, 5437-5443 (2009).
48	D.J. Crotty, R.L. McKinley, M.P. Tornai, "Experimental spectral measurements of heavy K-edge filtered beams for x-ray computed mammotomography," Phys.Med.Biol. **52**, 603-616 (2007).
49	M.J. Berger, Hubbell, J.H., Seltzer, S.M., Chang, J., Coursey, J.S., Sukumar, R., Zucker, D.S., and Olsen, K, "XCOM: Photon Cross Section Database

(version 1.5)," (National Institute of Standards and Technology, Gaithersburg, MD, 2010).

50   F. Salvat, J. Fernandez-Vare, J. Sempau, "PENELOPE-2006: A code system for Monte Carlo simulation of electron and photon transport," (OECD/NEA Data Bank 2006, 2006).

51   J. Sempau, A. Badal, L. Brualla, "A PENELOPE-based system for the automated Monte Carlo simulation of clinacs and voxelized geometries-application to far-from-axis fields," Med Phys **38**, 5887-5895 (2011).

52   L. Feldkamp, L. Davis, J. Kress, "Practical cone-beam algorithm," J.Opt.Soc.Am **1**, 612-619 (1984).

53   J. Fessler, "Image Reconstruction Toolbox," (University of Michigan).

54   I. Sechopoulos, "X-ray scatter correction method for dedicated breast computed tomography," Med Phys. **39**, 2896-2903 (2012).

55   J.P. Bissonnette, D.J. Moseley, D.A. Jaffray, "A quality assurance program for image quality of cone-beam CT guidance in radiation therapy," Med Phys. **35**, 1807-1815 (2008).

56   P.J. La Riviere, X. Pan, "Favorable noise uniformity properties of Fourier-based interpolation and reconstruction approaches in single-slice helical computed tomography," Med Phys **29**, 943-951 (2002).

57   X. Pan, L. Yu, "Image reconstruction with shift-variant filtration and its implication for noise and resolution properties in fan-beam computed tomography," Med Phys **30**, 590-600 (2003).

58   J. Hsieh, "Nonstationary noise characteristics of the helical scan and its impact on image quality and artifacts," Med Phys **24**, 1375-1384 (1997).

59   A. Wunderlich, F. Noo, "Achieving Uniform Noise in Direct Fan-beam CT Reconstruction Through Bowtie Filter Design," IEEE Nuclear Science Symposium Conference Record **6**, 4379 - 4382 (2007).

60   W.T. Yang, S. Carkaci, L. Chen, C.J. Lai, A. Sahin, G.J. Whitman, C.C. Shaw, "Dedicated cone-beam breast CT: feasibility study with surgical mastectomy specimens," AJR.Am.J.Roentgenol. **189**, 1312-1315 (2007).

61   M.A. Habibzadeh, M.R. Ay, A.R. Asl, H. Ghadiri, H. Zaidi, "Impact of miscentering on patient dose and image noise in x-ray CT imaging: Phantom and clinical studies," Phys.Med **28**, 191-199 (2012).

62   T. Toth, Z. Ge, M.P. Daly, "The influence of patient centering on CT dose and image noise," Med Phys. **34**, 3093-3101 (2007).

63   J.M. Boone, A.L. Kwan, K. Yang, G.W. Burkett, K.K. Lindfors, T.R. Nelson, "Computed tomography for imaging the breast," J.Mammary.Gland.Biol.Neoplasia. **11**, 103-111 (2006).

64   K.K. Lindfors, J.M. Boone, T.R. Nelson, K. Yang, A.L. Kwan, D.F. Miller, "Dedicated breast CT: initial clinical experience," Radiology **246**, 725-733 (2008).

65   K. Kontson, R.J. Jennings, "Bowtie Filter Designs for Dedicated Breast CT," Medical physics **40**, 527 (2013).

66   K. Kontson, R.J. Jennings, "Bowtie filter designs for dedicated breas CT Part 1: theory and computational implementation," Med Phys **Submitted**2014).

67 H. Bornefalk, M. Danielsson, "Photon-counting spectral computed tomography using silicon strip detectors: a feasibility study," Phys Med Biol **55**, 1999-2022 (2010).

68 V.C. Cajipe, R;Clajus, M;Gratten, B;Hayakawa, S;Jayaraman, R;Tumer, T;Yossifor, O, "Multi-energy x-ray imaging with linear CZT pixel arrays and integrated electronics," IEEE Nuclear Science Symposium Conference Record **7**, 4548-4551 (2004).

69 J.S.M. Iwanczyk, N.O.;Arenson, J;Hartsough, N.E.;Malakhov, N;Wessel,J.C., "Photon Counting Energy Dispersive Detector Arracys for X-Ray Imaging," IEEE Nuclear Science Symposium Conference Record **56**, 2741-2748 (2007).

70 C.S. Szeles, S; Vydrin, S; Graves, J; Bale, D, "Ultra High Flux 2-D CdZnTe Monolithic Detector Arrays for X-Ray Imaging Applications," IEEE transactions on medical imaging **54**, 1350-1358 (2007).

71 S.J. Glick, C. Didier, "Investigating the effect of characteristic x-rays in cadmium zinc telluride detectors under breast computerized tomography operating conditions," Journal of applied physics **114**, 144506 (2013).

72 P.M. Shikhaliev, S.G. Fritz, "Photon counting spectral CT versus conventional CT: comparative evaluation for breast imaging application," Phys.Med.Biol. **56**, 1905-1930 (2011).

73 I. Sechopoulos, S.S. Feng, C.J. D'Orsi, "Dosimetric characterization of a dedicated breast computed tomography clinical prototype," Med Phys **37**, 4110-4120 (2010).

74 G.J. Bootsma, F. Verhaegen, D.A. Jaffray, "The effects of compensator and imaging geometry on the distribution of x-ray scatter in CBCT," Med.Phys. **38**, 897-914 (2011).

75 S.A. Graham, D.J. Moseley, J.H. Siewerdsen, D.A. Jaffray, "Compensators for dose and scatter management in cone-beam computed tomography," Med Phys. **34**, 2691-2703 (2007).

76 A.L. Kwan, J.M. Boone, N. Shah, "Evaluation of x-ray scatter properties in a dedicated cone-beam breast CT scanner," Med Phys. **32**, 2967-2975 (2005).

77 B. Liu, S.J. Glick, C. Groiselle, "Characterization of Scatter Radiation in Cone Beam CT Mammography," Proc. SPIE **5745**, 818-827 (2005).

78 G. Jarry, S.A. Graham, D.J. Moseley, D.J. Jaffray, J.H. Siewerdsen, F. Verhaegen, "Characterization of scattered radiation in kV CBCT images using Monte Carlo simulations," Med Phys. **33**, 4320-4329 (2006).

79 R. Ning, X. Tang, D. Conover, "X-ray scatter correction algorithm for cone beam CT imaging," Med Phys. **31**, 1195-1202 (2004).

80 Y. Chen, B. Liu, J.M. O'Connor, C.S. Didier, S.J. Glick, "Characterization of scatter in cone-beam CT breast imaging: comparison of experimental measurements and Monte Carlo simulation," Med.Phys. **36**, 857-869 (2009).

81 G.H. Glover, "Compton scatter effects in CT reconstructions," Med Phys **9**, 860-867 (1982).

82 A. Keely, I.S. Kyprianou, R.J. Jennings, K.J. Myers, T. Gilat-Schmidt, "Phantom Development for Artifact Reduction in Cone-Beam CT," Med Phys **34**, 2340 (2007).

83   R.J. Jennings, C. Mariani Bettolo, K. Kontson, S. Beg, E. Akinnagbe, presented at the 54th Annual Meeting of AAPM.

84   I.S. Kyprianou, S. Paquerault, B.D. Gallas, A. Badano, S. Park, K.J. Myers, "Framework for the determination of geometric parameters of a cone beam CT scanner for measuring the system response function and improved object reconstruction," IEEE Trans on Information Technology in Biomedicine, 1248-1251 (2006).

85   K. Kontson, R.J. Jennings, I.S. Kyprianou, "X-Ray Spectra for Breast CT," Med Phys **39**, 3913-3914 (2012).

86   J.M. Boone, V.N. Cooper, 3rd, "Scatter/primary in mammography: Monte Carlo validation," Med Phys **27**, 1818-1831 (2000).

87   J.M. Boone, K.K. Lindfors, V.N. Cooper, 3rd, J.A. Seibert, "Scatter/primary in mammography: comprehensive results," Med Phys **27**, 2408-2416 (2000).

88   R. Fahrig, J.G. Mainprize, N. Robert, A. Rogers, M.J. Yaffe, "Performance of glass fiber antiscatter devices at mammographic energies," Med Phys **21**, 1277-1282 (1994).

89   M.J. Yaffe, A. Fenster, J. H.E., "Xenon ionization detectors for fan beam computed tomography scanners," J. Comput. Assist. Tomogr **1**, 419-428 (1977).

90   H. Gao, R. Fahrig, N.R. Bennett, M. Sun, J. Star-Lack, L. Zhu, "Scatter correction method for x-ray CT using primary modulation: phantom studies," Med Phys **37**, 934-946 (2010).

91   L. Zhu, N.R. Bennett, R. Fahrig, "Scatter correction method for X-ray CT using primary modulation: theory and preliminary results," IEEE transactions on medical imaging **25**, 1573-1587 (2006).

92   A.P. Colijn, F.J. Beekman, "Accelerated simulation of cone beam X-ray scatter projections," IEEE transactions on medical imaging **23**, 584-590 (2004).

93   G.J. Bootsma, F. Verhaegen, D.A. Jaffray, "The effects of compensator design on scatter distribution and magnitude: A Monte Carlo study," SPIE Medical Imaging **SPIE Proc. 7961**, 91-912 (

94   J.M. Boone, "Method for evaluating bow tie filter angle-dependent attenuation in CT: theory and simulation results," Med Phys **37**, 40-48 (2010).

95   G. Zhang, N. Marshall, R. Jacobs, Q. Liu, H. Bosmans, "Bowtie filtration for dedicated cone beam CT of the head and neck: a simulation study," The British journal of radiology **86**, 20130002 (2013).

96   J.T. Bushberg, J.A. Seibert, E.M. Leidholdt, J.M. Boone, *The Essential Physics of Medical Imaging*, 3 ed. (Lippincott Williams & Wilkins, 2012).

97   G.X. Ding, D.M. Duggan, C.W. Coffey, "Characteristics of kilovoltage x-ray beams used for cone-beam computed tomography in radiation therapy," Phys Med Biol **52**, 1595-1615 (2007).

98   S. Itoh, S. Koyama, M. Ikeda, M. Ozaki, A. Sawaki, S. Iwano, T. Ishigaki, "Further reduction of radiation dose in helical CT for lung cancer screening using small tube current and a newly designed filter," Journal of thoracic imaging **16**, 81-88 (2001).

99   W.A. Kalender, M. Beister, J.M. Boone, D. Kolditz, S.V. Vollmar, M.C. Weigel, "High-resolution spiral CT of the breast at very low dose: concept and feasibility considerations," European radiology **22**, 1-8 (2012).

100   E.P. Ruhrnschopf, K. Klingenbeck, "A general framework and review of scatter correction methods in x-ray cone-beam computerized tomography. Part 1: Scatter compensation approaches," Med Phys. **38**, 4296-4311 (2011).

101   W. Cai, R. Ning, D. Conover, "Scatter correction for clinical cone beam CT breast imaging based on breast phantom studies," J Xray.Sci Technol. **19**, 91-109 (2011).

102   H. Lee, L. Xing, R. Lee, B.P. Fahimian, "Scatter correction in cone-beam CT via a half beam blocker technique allowing simultaneous acquisition of scatter and image information," Med Phys. **39**, 2386-2395 (2012).

103   T. Niu, L. Zhu, "Scatter correction for full-fan volumetric CT using a stationary beam blocker in a single full scan," Med Phys. **38**, 6027-6038 (2011).

104   J. Wang, W. Mao, T. Solberg, "Scatter correction for cone-beam computed tomography using moving blocker strips: a preliminary study," Med Phys. **37**, 5792-5800 (2010).

105   A. Sisniega, W. Zbijewski, A. Badal, I.S. Kyprianou, J.W. Stayman, J.J. Vaquero, J.H. Siewerdsen, "Monte Carlo study of the effects of system geometry and antiscatter grids on cone-beam CT scatter distributions," Med Phys **40**, 051915 (2013).

106   D. Shepard, "A two-dimensional interpolation function for irregularly spaced data," Proc. of the 1968 23rd ACM National Conference, 517-524 (1968).

107   Y. Cho, D.J. Moseley, J.H. Siewerdsen, D.A. Jaffray, "Accurate technique for complete geometric calibration of cone-beam computed tomography systems," Med Phys **32**, 968-983 (2005).

108   P.M. Shikhaliev, "Energy-resolved computed tomography: first experimental results," Phys.Med.Biol. **53**, 5595-5613 (2008).

109   P.M. Shikhaliev, "Computed tomography with energy-resolved detection: a feasibility study," Phys.Med.Biol. **53**, 1475-1495 (2008).

110   P.M. Shikhaliev, "Projection x-ray imaging with photon energy weighting: experimental evaluation with a prototype detector," Phys.Med.Biol. **54**, 4971-4992 (2009).

111   C.C. Brunner, I.S. Kyprianou, "Material-specific transfer function model and SNR in CT," Phys Med Biol **58**, 7447-7461 (2013).

112   C.C. Brunner, S.F. Abboud, C. Hoeschen, I.S. Kyprianou, "Signal detection and location-dependent noise in cone-beam computed tomography using the spatial definition of the Hotelling SNR," Med Phys **39**, 3214-3228 (2012).

113   Y. Meng, H. Gong, X. Yang, "Online geometric calibration of cone-beam computed tomography for arbitrary imaging objects," IEEE transactions on medical imaging **32**, 278-288 (2013).

114   D. Panetta, N. Belcari, A. Del Guerra, S. Moehrs, "An optimization-based method for geometrical calibration in cone-beam CT without dedicated phantoms," Phys Med Biol **53**, 3841-3861 (2008).

115   K. Yang, A.L. Kwan, D.F. Miller, J.M. Boone, "A geometric calibration method for cone beam CT systems," Med Phys **33**, 1695-1706 (2006).

116   S. Fine, C. Hendee, "X-Ray Critical Absorption and Emissionf Energies in keV," Philips Laboratories, Irvington on Hudons, New York.

117   R.L. McKinley, "Development and characterization of a dedicated computed mammotomography system," (Duke University, Department of Biomedical Engineering, 2006).

118   "Varian Medical Systems Introduces New X-Ray Tubes and Flat Panel Products at RSNA," http://investors.varian.com/index.php?s=43&item=7922010).

119   J. Baek, N.J. Pelc, "The noise power spectrum in CT with direct fan beam reconstruction," Med Phys **37**, 2074-2081 (2010).

120   C.C. Brunner, S.F. Hurowitz, S.F. Abboud, C. Hoeschen, I. Kyprianou, "Noise characterization of computed tomography using the covariance matrix," Proc. SPIE, 7622:76224Z (2010).

121   A.R. Pineda, D.J. Tward, A. Gonzalez, J.H. Siewerdsen, "Beyond noise power in 3D computed tomography: the local NPS and off-diagonal elements of the Fourier domain covariance matrix," Med Phys **39**, 3240-3252 (2012).

122   E. Samei, M.J. Flynn, "An experimental comparison of detector performance for computed radiography systems," Med Phys **29**, 447-459 (2002).

123   E. Samei, M.J. Flynn, "An experimental comparison of detector performance for direct and indirect digital radiography systems," Med Phys **30**, 608-622 (2003).

124   E. Fredenberg, "Matlab File ID #36462: Noise Power Spectrum," Royal Institute of Technology2012).

125   J. Baek, N.J. Pelc, "Local and global 3D noise power spectrum in cone-beam CT system with FDK reconstruction," Med Phys **38**, 2122-2131 (2011).

126   A. Wunderlich, F. Noo, "Image covariance and lesion detectability in direct fan-beam x-ray computed tomography," Phys Med Biol **53**, 2471-2493 (2008).

127   J.H. Siewerdsen, I.A. Cunningham, D.A. Jaffray, "A framework for noise-power spectrum analysis of multidimensional images," Med Phys **29**, 2655-2671 (2002).